Charles University in Prague
Faculty of Mathematics and Physics

PhD THESIS

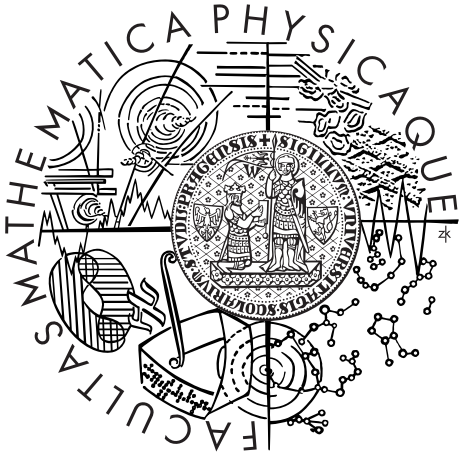

Vahid Abbasvand Azar

Chromospheric waves and their contribution to heating of the atmosphere

Astronomical Institute of the Charles University
Astronomical Institute of the Czech Academy of Sciences, v.v.i.

Supervisor of the PhD thesis: RNDr. Michal Sobotka, DSc.
Advisor of the PhD thesis: Prof. RNDr. Petr Heinzel, DrSc.

Prague 2021

I dedicate my dissertation work to my family, especially to my parents who have always stressed the importance of education. They gave me moral and emotional support and instilled in me a tireless work ethic and persistent determination to be whatever I wanted to be in life without limitations. They are two pillars of strength in my life.

First of all, I would like to offer my sincere gratitude to my supervisor Dr. M. Sobotka and my advisor Prof. P. Heinzel from the Astronomical Institute of the Czech Academy of Sciences for their guidance and support throughout this thesis. I would also like to thank the solar physics team at the Leibniz-Institut für Astrophysik Potsdam (AIP), especially Dr. C. Denker, whose insight and knowledge into the subject matter steered me through this research.

During my doctoral studies I was supported by the Czech Science Foundation grant 18-08097J. Some observations were supported by the project SOLARNET that has received funding from the European Union Horizon 2020 research and innovation programme under grant agreement No. 824135.

I hereby declare that I am the sole author of this thesis and that neither any part of this thesis nor the whole of the thesis has been submitted for a degree to any other University or Institute.

I certify that, to the best of my knowledge, my thesis does not infringe upon anyone's copyright nor violate any proprietary rights and that any ideas, techniques, quotations, or any other material from the work of other people included in my thesis, published or otherwise, are fully acknowledged in accordance with the standard referencing practices.

I declare that this is a true copy of my thesis, including any final revisions, as approved by my thesis review committee.

I understand that my work relates to the rights and obligations under the Act No. 121/2000 Coll., the Copyright Act, as amended, in particular the fact that the Charles University in Prague has the right to conclude a license agreement on the use of this work as a school work pursuant to Section 60 paragraph 1 of the Copyright Act.

In ..... on ..... Author signature

Název práce: Chromosférické vlny a jejich příspěvek k ohřevu atmosféry

Autor: Vahid Abbasvand Azar

Katedra: Astronomický ústav UK, Matematicko-fyzikální fakulta, Univerzita Karlova

Školicí pracoviště: Astronomický ústav Akademie věd České republiky, v.v.i.

Vedoucí doktorandské práce: RNDr. Michal Sobotka, DSc., Astronomický ústav Akademie věd České republiky, v.v.i.

Abstrakt:

Akustické a magnetoakustické vlny hrají důležitou roli při ohřevu chromosféry, protože podstatná část jejich energie může být v chromosféře pohlcena. Ohřev sluneční chromosféry v oblastech s magnetickým polem a bez něho studujeme pomocí porovnání uložené energie akustických vln a celkových zářivých ztrát. Uloženou akustickou energii odvozujeme z pozorování silných chromosférických čar Hα, Hβ, Ca II 854.2 nm a Mg II k a h. Oblasti klidného Slunce a aktivní oblasti byly pozorovány pomocí přístrojů Interface Region Imaging Spectrograph (IRIS), Vacuum Tower Telescope (VTT), Dunn Solar Telescope (DST) a Goode Solar Telescope (GST). Deponovaná akustická energie je určena z dopplerovských rychlostí pozorovaných ve dvou rozdílných referenčních výškách, odpovídajících střední a horní chromosféře. Zářivé ztráty jsou vypočteny ze souboru škálovaných jednorozměrných non-LTE hydrostatických semiempirických modelů, které reprodukují pozorované profily spektrálních čar. Energie akustických vln deponovaná v klidné chromosféře stačí k vyrovnání zářivých ztrát a k udržení teplot popsaných semiempirickými modely ve vrstvě mezi oběma referenčními výškami. V chromosféře aktivních oblastí s magnetickým polem se ukazuje, že příspěvek energie magnetoakustických vln k zářivým ztrátám je jenom 10–30 %, takže je příliš malý na jejich vyrovnání a chromosféra je ohřívána jinými mechanismy.

Klíčová slova: sluneční chromosféra – oscilace – přenos záření

Title: Chromospheric waves and their contribution to heating of the atmosphere

Author: Vahid Abbasvand Azar

Department: Astronomical Institute of the Charles University, Faculty of Mathematics and Physics, Charles University

Training institution: Astronomical Institute of the Czech Academy of Sciences, v.v.i.

Supervisor of the Ph.D. thesis: RNDr. Michal Sobotka, DSc., Astronomical Institute of the Czech Academy of Sciences, v.v.i.

Abstract:

Acoustic and magnetoacoustic waves play an important role in the chromospheric heating, exhibiting the capability of depositing a main part of their energy in the chromosphere. To study the heating of solar chromospheric magnetic and non-magnetic regions by acoustic and magnetoacoustic waves, the deposited acoustic-energy flux, derived from observations of strong chromospheric lines (Hα, Hβ, Ca II 854.2 nm, and Mg II k&h), is compared with the total integrated radiative losses. A set of quiet-Sun and weak-plage regions was observed with the Interface Region Imaging Spectrograph (IRIS), Vacuum Tower Telescope (VTT), Dunn Solar Telescope (DST) and Goode Solar Telescope (GST). The deposited acoustic-energy flux is derived from Doppler velocities observed at two different reference heights corresponding to the middle and upper chromosphere. A set of scaled non-LTE 1D hydrostatic semi-empirical models, obtained by fitting synthetic to observed line profiles, is applied to compute the radiative losses. In the quiet chromosphere, the deposited acoustic flux is sufficient to balance the radiative losses and maintain the semi-empirical temperatures in layers between the two reference heights. In the magnetic active-region chromosphere, the comparison shows that the contribution of magnetoacoustic energy flux to the radiative losses is only 10–30 %, so that the contribution is too small to balance the radiative losses in the chromosphere, which has to be heated by other mechanisms.

Keywords: Sun: chromosphere – oscillations – radiative transfer

Contents

Chapter 1

Introduction

1.1 The Sun

The Sun as one of the stars in the Milky Way orbits the center of the galaxy with a speed of 217 km s^{-1} and the period of 230 million years. The Sun is located on the main sequence of the Hertzsprung-Russell (H-R) diagram with spectral type G2 and luminosity class V. The Sun has been on the main sequence for 5 Gyr and it will leave it toward the giant branch after another 5 Gyr. Now the Sun is in its main-sequence phase, where the main source of energy is the nuclear fusion of hydrogen to helium. After the initial phase of accretion of mass, a self gravitating lasts for most of its life. The period for the Sun will continue for approximately another five billion years when the evolutionary stages include a complex variation of the radius, with burning of helium as the source of energy in a later red giant phase. After ending helium burning, the mass of the Sun is believed to be not large enough to continue further fusion stages, and finally the Sun will slowly faint as a white dwarf star.

At the core of the Sun, the density ($\sim$ 160 g cm^{-3}) and temperature ($\sim$ 13 million Kelvin) are high enough to fuse hydrogen and burn it into helium to produce energy in the form of high-energy photons. The output energy from the nuclear reactions keeps the core of the Sun at high temperature to sustain the gravitational load from the outer gas shells. In the high density, the photons are continuously absorbed and re-emitted by ions, therefore the energy output is slowly radiated toward the surface of the Sun. In this way, the density along with the temperature decreases exponentially.

In the convection zone at the distance from approximately $0.7R_{\odot}$ to the surface, the radiation process is not efficient enough to transport the huge amount of energy produced in the core. In this region, the gas is heated up, and the density of convection cells dwindle and rise by the buoyancy force while cool gas sinks to the bottom of the cells, where it is heated again. The flows transport the energy to the outer layer, and at the surface of the Sun they create granules where the effective temperature is $\sim$ 5700 K. The density drops enough that the photons can escape without much further absorption. The layer where we receive most of the photons in the optical part of the spectrum can is called "photosphere" (sphere of light). Figure 1.1 shows the photosphere of the Sun and granules generated by convection currents.

In the second layer of solar atmosphere, called "chromosphere", the gas density

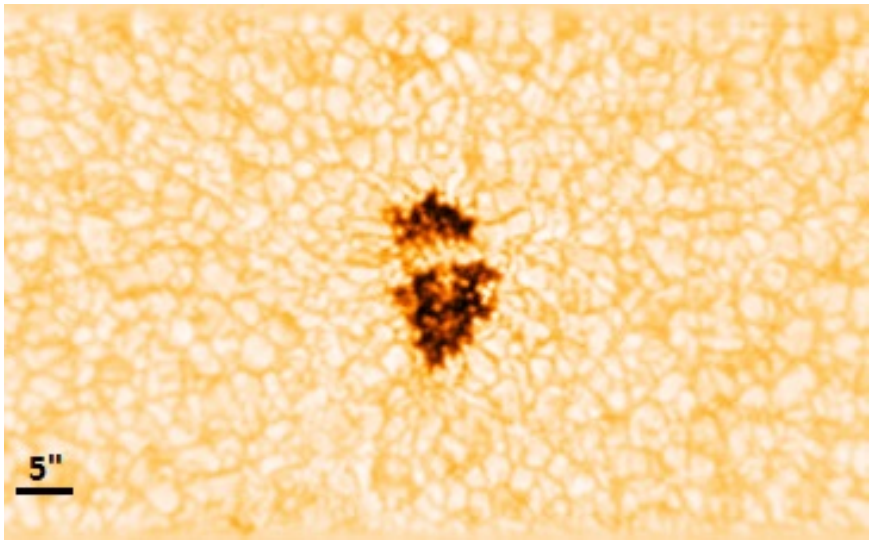

Figure 1.1: IBIS image of the photosphere of the Sun. Granules are seen all around the photosphere outside the dark area (pore). They form the uppermost layers of the convection zone, in which the energy is transported from deep down outwards via gas motions. At the top, the gas cools down by radiating photons into space. Localized strong magnetic fields can also emerge and are seen as dark areas, the sunspots, which are a consequence of the less efficient energy transport.

decreases upwards and the magnetic fields originated inside the Sun cease to be pushed around by gas flows. At the height about 500 km, according to standard semi-empirical models, the temperature is of about 4000 K, which is low enough to allow the formation of molecules like CO or water vapor. Above this temperature minimum T_{min}, the temperature increases again. This increase (chromospheric heating) can be caused by various mechanisms, for example, the dissipation of (magneto)acoustic waves coming from the photosphere and/or the heat release during reconnection processes in magnetic field. The ionization of hydrogen starts and it absorbs a lot of energy released within the chromosphere. The temperature reaches to 8000–10000 K and the chromospheric layer extends to the height of about 2000 km. This work deals with physical properties of this layer and studies the factors involved in heating the chromosphere.

The next layer is the transition region (TR) that separates the corona from the chromosphere. In this layer the temperature goes up abruptly. The number of neutral hydrogen atoms is no longer sufficient to absorb all of the acoustic flux energy, so that it becomes one of the candidates for the source of coronal heating. A significant amount of the energy is transported toward the upper layers by thermal conduction. As a result, temperature suddenly jumps by more than 10000 K.

The outer atmosphere of the Sun is the corona, extending to several solar radii. It gradually transforms into the solar wind that flows outward through our solar system. The temperature in the corona rises abruptly to a million degrees, while the pressure and density in the corona are much lower than in the chromosphere. The density of plasma falls rapidly through the transition region moving upward from the chromosphere to the corona. During a total solar eclipse, the corona briefly comes into view as the Moon blocks out the solar surface. Artificially,

a special instrument (coronagraph), allows astronomers to look at the corona anytime.

During the first phases of the life of the Sun, most of its angular momentum was removed by a strong wind and braking via magnetic fields anchored in the surrounding interstellar medium. The remaining angular momentum leads to slowly rotation. As the Sun is not completely rigid body, the rotation varies with latitude from the equator to the poles so that the plasma at the equator rotates with a period of 27 days and at the poles this period is roughly 32 days. In the inner part of the Sun the rotation is like a rigid body. The differential rotation is present in the convective zone, between its lower boundary called tachocline and the solar surface. The differential rotation creates meridional flows of plasma directed towards the poles near the surface and towards the equator near the bottom of the convection zone.

The Sun is a magnetic star. The Solar magnetic field is generated through a dynamo process driven by the differential rotation and plasma turbulence in the convection zone. Toroidal magnetic flux generated by the dynamo action rises from the base of the convection zone to the surface of the Sun through buoyancy. The magnetic field comes into sight in a wide range of spatial scales with different magnitudes in the photosphere. Active regions (AR) are the regions of enhanced surface magnetic fields, which generally display a bipolar configuration. The largest features in terms of size and the magnetic field strength are sunspots. Magnetic field structures also appear on smaller scales. Magnetic elements are known as the smallest magnetic-field structures on the solar surface. They appear in the quiet-Sun regions mostly at the boundaries of large-scale convective cells, known as supergranules, forming the magnetic network. The magnetic field, which emerges near the centers of supergranules outside the magnetic network is known as the inter-network magnetic field.

The magnetic field of the Sun varies periodically in time and this phenomenon is called the "solar cycle" and it is also known as the "sunspot cycle" with the period of approximately 11 years, because the number of sunspots changes during the solar cycle. Sunspots do not appear randomly over the surface of the Sun. They are concentrated in two latitude bands ($\pm$ 30°) on either side of the equator. In general, the first spots for each cycle appear at higher latitudes in both hemisphere, and then move toward the equator as the cycle progresses. The full magnetic-field cycle of the Sun has a mean period of 22 years, when the magnetic polarity reverses after 11 years. Active regions, in particular sunspots, are located in areas of strong magnetic field which are relevant for all energetic phenomena on the Sun, such as flares or coronal mass ejections (CMEs).

The solar flares are important phenomena in the solar atmosphere. They occur in active regions around sunspots, where intense magnetic fields emerges in the photosphere. The flare is a result of releasing the magnetic energy (up to 6×10^{25} J) that has built up in the solar atmosphere by instability in the magnetic configuration. Such energy creates an acceleration of non-thermal particles and a heating of coronal and chromospheric plasma. These processes emit radiation in almost all wavelengths: radio, visible light, EUV, soft X-rays, and hard X-rays during large flares. Solar flares affect all layers of the solar atmosphere. The solar structure is shown in Figure 1.2.

The coronal mass ejection is an ejection of material from the solar corona.

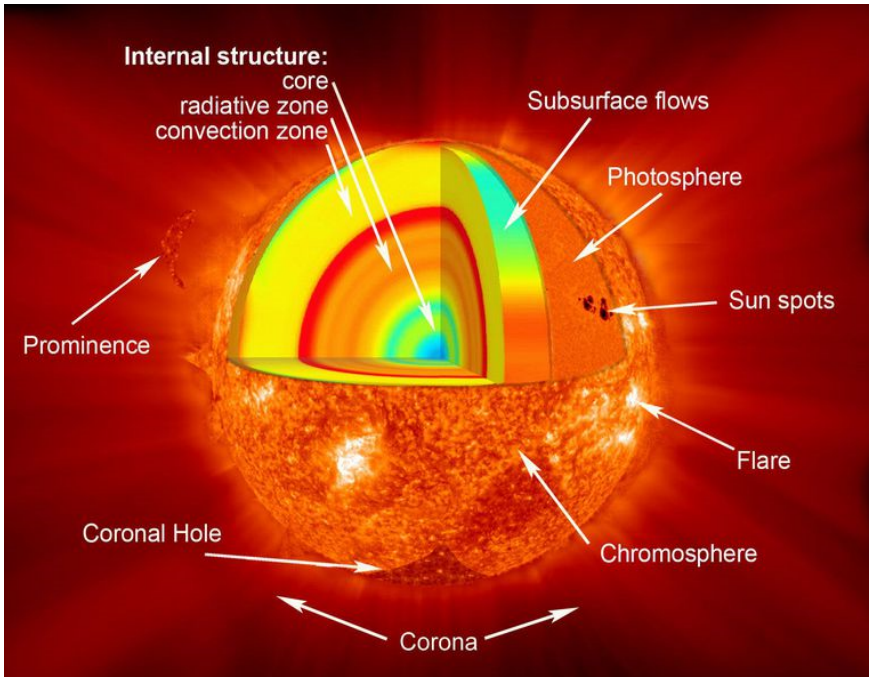

Figure 1.2: The internal structure of the Sun, its atmosphere, and solar-activity phenomena in a NASA drawing.

CME is highly magnetized hydrogen plasma consisting of electrons, protons and small quantities of heavier elements such as helium, oxygen, and iron. CMEs affect the space weather and are often responsible for disturbances of the geomagnetic field. Solar flares and CMEs are caused by magnetic reconnection. Magnetic reconnection of two groups of magnetic field lines with opposite directions leads to the formation of rising hot cusp-shaped coronal arcades and the eruption of a filament in the corona above the flaring region. This eruption may result in the formation of a CME.

The Sun is the closest star to the Earth, hence it is the only star that allows us to resolve directly structures on its surface and get enough energy to investigate in detail its spectrum. With current telescopes and techniques it is possible to resolve structures with sizes below 100 km. The solar atmosphere and the effects of magnetism can also be studied by methods of numerical simulations. This thesis is focused to the chromosphere and a its possible heating by (magneto)acoustic waves.

1.2 The chromosphere

The solar chromosphere is traditionally defined as a thin layer of the Sun, lying between the photosphere and the transition region, approximately, 2000 km just above the photosphere. The lower boundary in this definition is formed by the temperature minimum (T_{min}) layer. The upper boundary of this definition is less clear, however, generally prescribed by a temperature around 1–2$\times 10^4$ K. Due to low density in the chromosphere, this layer is more visually transparent than the photosphere. It is red in color because the spectrum of the chromosphere is dominated by the deep red Hα spectral line of hydrogen. Only during the

total solar eclipse, this layer may be seen directly with the naked eye. There are some reasons, which are not fully understood, why the temperature of the chromosphere, indicated by static semi-empirical models, is hotter than that of the photosphere. The chromospheric temperature varies from 4500 K to as high as 20000 K, while in the photosphere the temperature is of about 5800 K.

Regarding the explanation of chromospheric heating, there are two main competitive candidates: (1) heat release connected to two groups of magnetic field lines with opposite directions and their reconnection, which creates local electric current sheets to release the magnetic energy (Rabin and Moore, 1984); (2) dissipation of the energy of upward-propagating magneto-acoustic waves generated above the convection zone due to turbulent motions (e.g., Aschwanden, 2001; Zaqarashvili and Erdélyi, 2009; Kayshap et al., 2018, and references therein). This thesis is focused to the study of the second mechanism.

It is a matter of discussion if this increase of temperature reported by the static semi-empirical models is real. The dissipation of acoustic waves is generally time-dependent. Carlsson and Stein (1995) applied time-dependent 1D radiation-hydrodynamic models to compute the propagation of acoustic waves in the non-LTE regime. They found that acoustic shocks cause short time intervals of high temperature, however, the average temperature of the chromosphere continuously decreases with height. This result disagrees with the fact that emission in chromospheric lines exists everywhere and all the time (Carlsson et al., 1997; Kalkofen et al., 1999). The discrepancy might be solved by a multi-dimensional approach, but the difficulties connected with multi-dimensional time-dependent non-LTE modeling, namely extremely high computational requirements, do not allow us to represent the observed chromospheric structures directly this way (Carlsson and Leenaarts, 2012a). The alternative of a stationary approach with time-averaged atmospheric parameters provided by 1D semi-empirical hydrostatic models (Sobotka et al., 2016) may, at present, help to avoid these difficulties.

The quiet and active chromosphere is full of structures observed at different spatial scales. There are numerous magnetic structures and phenomena such as sunspots, plages, flare ribbons, eruption, network, internetwork, Hα-grains, quiescent prominences, filaments, spicules, cool CO-clouds, 3-min oscillations, shock waves and so forth. In the chromosphere, waves, magnetic field, and non local thermodynamics equilibrium (NLTE) effects on line formation become energetically important. The broad range of the different wavelengths, from the EUV to the radio, provides conditions to reveal various structures and inhomogeneities. For instance, plages are seen in strong lines such as Mg II k&h, Ca II H&K, and in EUV emission lines like O I 110 nm and He I 50.4 nm. Dark structures in Ca II H&K filtergrams are barely visible. Spicules, prominent fibrils and grains are best seen in the Hα line. Sunspots are only seen in radiation coming from the lower chromosphere and they appear bright in the EUV He II lines. The cool CO-clouds are visible practically only in the fundamental rotational-vibrational bands of CO at around 4.7 μm.

Polarimetry in the strong chromospheric spectral lines such as Hβ, Na I D, Ca II infrared triplet, and in the nearly optically thin He I 1083 nm makes possible to construct magnetic-field maps. Figure 1.3 shows a comparison between the photospheric and chromospheric images of an active region located relatively close to the disk center. The chromospheric images in Hα were taken with the

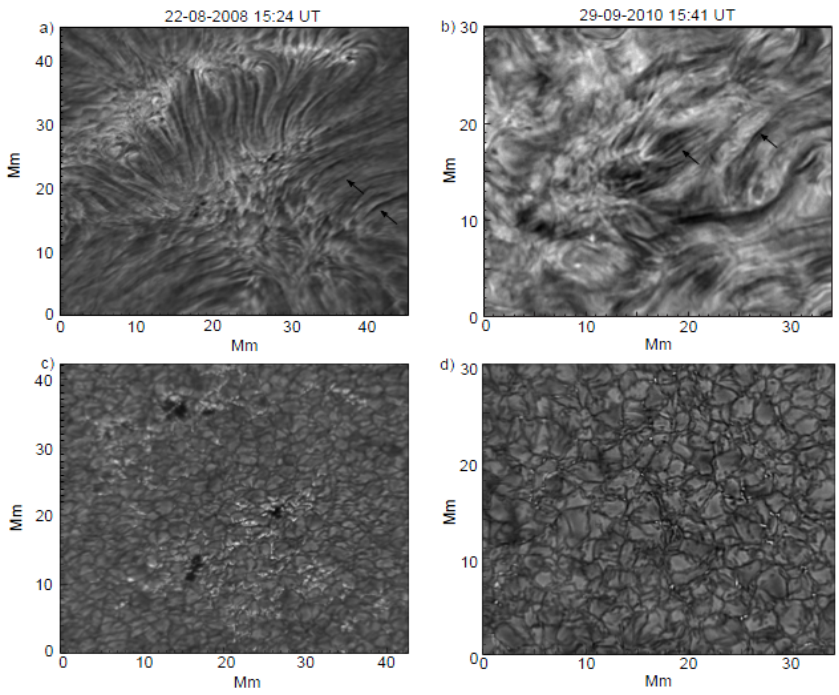

Figure 1.3: The solar atmosphere observed by ROSA. (*a*) and (*b*) – The solar chromosphere in a magnetically active region as seen with an Hα 6562.8 Å filter. The existence of fine-scale structuring in the bandpass is evident in both datasets, with both spicules/mottles and cell-spanning fibrils identifiable. Examples of fibrils are highlighted by the black arrows. (*c*) and (*d*) – Corresponding G-band images centered at 4305.0 Å, which reveals magnetic bright points, larger magnetic pores and the solar granulation. The G-band images depict the solar photosphere that lies directly under the Hα chromosphere. The figure is provided through the courtesy of Morton et al. (2014)

Rapid Oscillations in the Solar Atmosphere (ROSA) instrument at the Dunn Solar Telescope (top frames) and the corresponding photospheric G-band images were observed with the Hinode Solar Optical Telescope (SOT) (bottom frames).

The chromosphere is also strongly dynamic and shows both periodic and aperiodic variations. From the point of the oscillatory motions, the amplitude of oscillations, which are seen in the cores of strong absorption spectral lines and EUV emission lines, is a far larger than their photospheric counterparts. The chromospheric oscillations are significantly different between the network and internetwork. The dominant period of oscillation in the interiors of cells (internetwork) is 3 min and the waves propagate upward. Lites et al. (1993) computed the velocity power spectrum over the averaged network and internetwork in the quiet Sun with the Ca II H line. The results for the network show that high power is basically at periods longer than approximately 4–5 min, while for the internetwork it is found between 1.5 and 4 min.

The magnetic field links the photosphere and the corona by transition of the photospheric flux tubes to the coronal loops and open field lines. Symbolically, chromospheric structures such as prominences, spicules, Hα fibrils, etc. are related to chromospheric magnetic fields (Sterling and Hollweg, 1989). Berger et al.

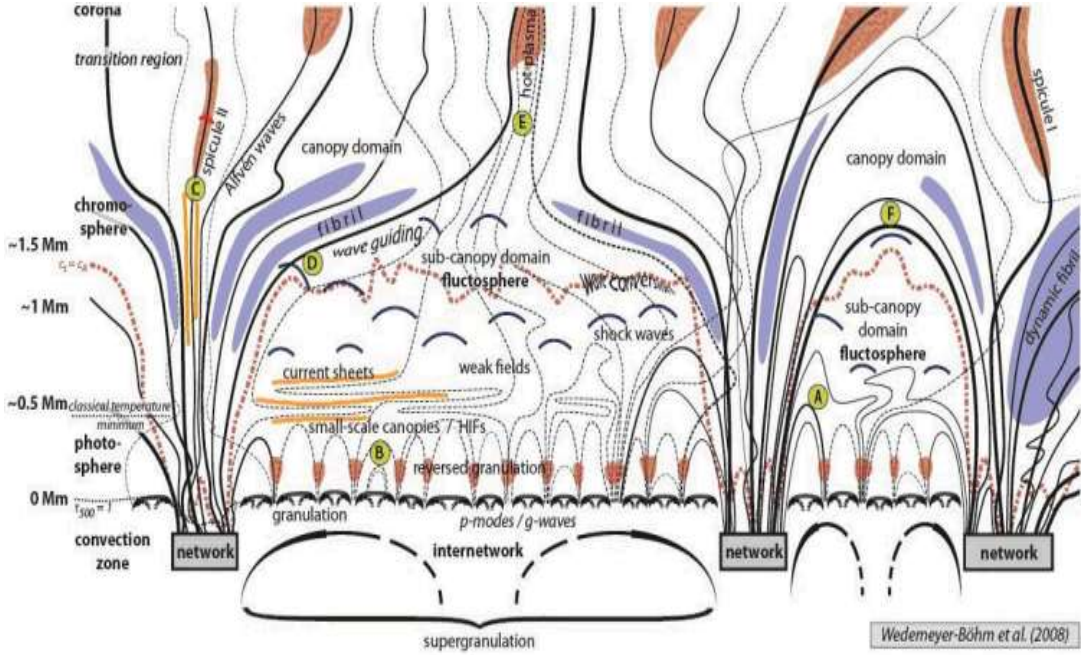

Figure 1.4: A sketch of the structures of the solar chromosphere and their coupling to the photosphere and the corona. The figure shows out of the sun emerging magnetic field lines (network), where it comes through reconnection to nano-flares. Finally, they initiate Alfvén waves, extending into the corona. Acoustic waves generated above the convection zone due to turbulent motions are propagated upward and heat the chromosphere. The current sheets are formed between the magnetic fields of different polarity layers and build up flares. Figure courtesy of Wedemeyer-Böhm et al. (2009, Fig. 16)

(1999) have presented that combinations of field lines from many photospheric sources can form magnetic loops. The moss is the term used for cell-like patterns of bright material with the typical temperature of up to million K, which is one of the evidences for the complexity of the chromospheric magnetic structure. In the moss domain, the magnetic field lines are strongly bent on their way from the photosphere to the corona. Further analysis reveals that it does not look like a chromospheric plage and is not correlated with the magnetic flux locations in the photosphere of the Sun.

Gabriel (1976) introduced magnetic canopies in the chromosphere to explain the emission measures of the chromosphere and transition region in UV lines. According to measurements, they lie certainly in active- and quiet-Sun regions in the lower chromosphere (Giovanelli and Jones, 1982; Jones and Giovanelli, 1982). Few years later, based on scattering polarization measurements in the Na I D lines, Landi degl'Innocenti (1998) pointed out that in quiet chromosphere the strength of horizontal magnetic fields is not far larger than a fraction of a Gauss. In the lower chromosphere, the presence of a canopy can theoretically be explained if the flux tube is hotter than its surrounding atmosphere, like CO-clouds (Solanki and Steiner, 1990). In 2003, an opposite idea to the presence of canopies in the lower chromosphere was discussed by Schrijver and Title (2003). They found that many of the field lines associated with the traditional canopy return to the photosphere near their original flux tube.

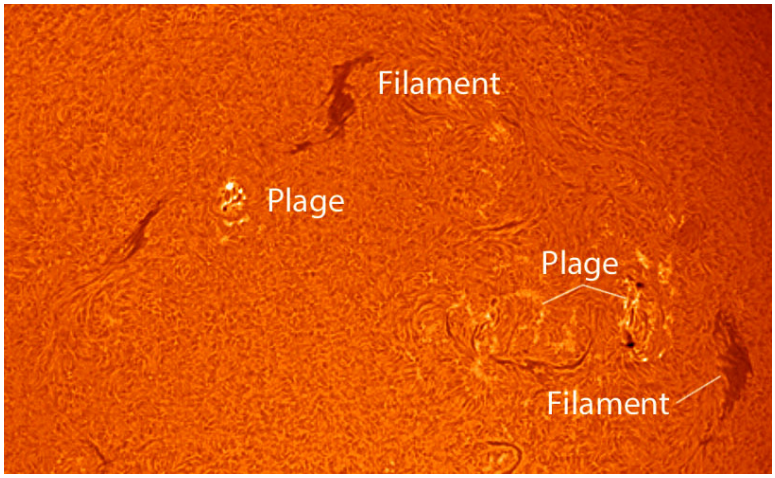

Figure 1.5: Plages and filaments are shown at solar disc center in the Hα 6563 Å. Courtesy of Alvaro Ibañez Perez.

Generally, it is difficult to use the Zeeman effect to measure the magnetic field in the chromosphere because most Zeeman-sensitive chromospheric lines are naturally broad and optically thick. They usually suffer from a complex line formation. Nevertheless, Hβ and radio observations provide interesting magnetic field strength maps to study the magnetic structures (Lee et al., 1999). To extract the full magnetic vector, nowadays, we can use "Hanle effect" measurements in resonance spectral lines, such as He I 1083 Å triplet, which forms in the upper chromosphere. The He triplet has the advantage that its components are optically thin, narrow and magnetically sensitive. As a method for the inversion, the SIR-code (Stokes Inversion based on Response functions) helps to obtain the full magnetic vector with high accuracy in the upper chromosphere (Ruiz Cobo and del Toro Iniesta, 1992).

Plages are the chromospheric signature of dense collections of small flux tubes, which in the photosphere correspond to faculae. In the photosphere, the contrast of faculae increases strongly moving from disc center to the solar limb. Diameter of the flux tubes is below roughly 500 km, usually even the smallest ones are bright at most wavelengths. Plages formed from the large flux tubes appear as bright structures in line cores at chromospheric filtergrams. In statistical terms, 90 % of plages are created by concentrations of small magnetic flux tubes with the total field strength of $\sim$ 1500 G. The magnetic pressure inside these tubes is greater than the gas pressure (β=8πP/B^2, β <1; the plasma β is related to the gas pressure P and magnetic-field strength B). The thermal stratification of magnetic elements is mostly responsible for the plages' brightness, where their atmosphere is hotter than quiet Sun. In the chromosphere at higher heights, the brightness contrast can be detected in shorter wavelengths, like UV, due to additional effects by non-radiative heating. Figure 1.5 shows plages at the solar disc center in the Hα line. Oscillations and waves in plages have been studied using theoretical and observational methods by Solanki (1997). Magneto(acoustic) and kink waves are the main candidates of heating the chromospheric layers of plages. For more detail on solar plages and other magnetic elements refer to Solanki (1993) and Steiner (1994).

Mottles, spicules, fibrils and dynamic fibrils, straws, rapid blue excursions

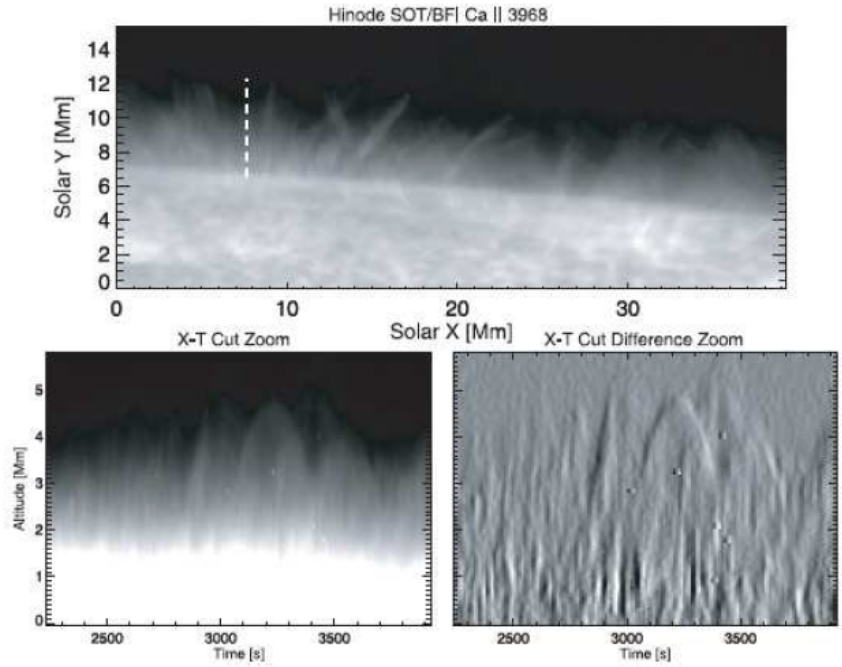

Figure 1.6: The top panel shows spicules at the quiet Sun limb obtained with the SOT/Hinode in the Ca II H passband. The bottom panels show space-time (X-T) plots along the location indicated by a dashed line in the top panels, for both the original and time difference data. The space-time plot is dominated by short-lived vertical stripes (Type II spicules) and longer-lived parabolic paths (Type I spicules) (Figure courtesy of de Pontieu et al. (2007))

(RBEs) are jet-like structures in the chromosphere. Obtaining parameters such as lifetime, size, spatial distribution, velocity, inclination, etc. of these structures is possible with narrow- and broad-band filtergrams. Spectroscopic observations provide other useful physical parameters such as temperature, density and flows. Spicules are the most common solar features within the chromosphere, which are seen at the limb of the Sun as thin and luminous jet-like features against the dark background. Roberts (1945) used the term "spicule" to describe jets shooting up to 10000 km heights. High resolution observations in the Ca II H line obtained with the Broadband Filter Imager (BFI) of SOT on the Hinode spacecraft can reveal some physical properties of spicules reported by de Pontieu et al. (2007). Based on this research, there are two types of spicules: Type I and II. The first one appears at the limb and falls back after rising up, it is long-lived (3–7 min) and exhibits longitudinal motions of the order of 20 km s^{-1}. The second one has a much shorter lifetime 50–100 s, higher velocity ($\sim$100 km s^{-1}), it is notably taller and exhibits only an upward motion and then it rapidly disappears. Figure 1.6 shows spicules at the quiet Sun limb.

Spicules, unlike the activity phenomena, are spread everywhere on the solar surface. The number of spicules counted along the solar limb depends on the height, solar latitude and quality of the observations. The total number of spicules on the Sun is estimated to reach up to 10^6, or even more (Beckers, 1972). The inclination of spicules is related to the local magnetic field topology. Recent computations by Pasachoff et al. (2009) report a mean variation of $\sim 23^\circ$ from

the local vertical. In their work, they also give estimates of heights in the range 4200–12200 km with a mean of 7200±2000 km and in width, most spicules have diameters between 400±1500 km with an average diameter 615±250 km. To extend his knowledge on the physical parameters of spicules, the reader can see the paper of Tsiropoula et al. (2012).

Mottles are rapidly changing hair-like jets observed in Hα or the Ca II lines in quiet-Sun regions on the solar disc. Considering these features as spicules by some authors can be right due to the fact that spicules are not observed only at the limb, but also can be seen as a kind of quiet-Sun structures on the disc (looking at the spicules from above, not in perpendicular direction). They appear in a complex geometric pattern over the solar disc contouring the boundaries of the chromospheric network seen in the Ca II lines. The mottles observed in the wings of Hα ± 0.5 Å are dark compared to the solar-disk background. Near the Hα line center, it is difficult to see them. Bratsolis et al. (1993) reported that mottles have no special shape, their horizontal dimension is between 720–10000 km and the mean lifetime is between 13–14 min. There is a debate in the solar physics community about the exact relationship between spicules and mottles.

In 1994, to find the physical conditions in dark and bright mottles, Heinzel and Schmieder (1994) applied a grid of prominence-like non-LTE models using Hα line profile observations over mottles. The models were 1D plane-parallel vertical slabs irradiated from both sides by an isotropic incident radiation. The result showed that the models have a higher-pressure ($P_g \sim 0.5$ dyn cm^{-2}) than the surrounding atmosphere and their temperature was around 10^4 K. For more details, the reader can see the review paper of Tsiropoula et al. (2012).

Pietarila et al. (2009) used Ca II K line observations to investigate the relationship between photospheric magnetic features and fibrils. The fibrils basically are structured by magnetic field and the bright endpoints are obviously co-spatial with the magnetic field concentrations in the photosphere. Due to high density of fibrils and vertical magnetic fluxes in strong plage region, it is difficult to identify the endpoints. The Ca II K fibrils appear bright which indicates a temperature enhancement in the chromospheric layers and support the presence of a hot magnetic canopy. In principle the fibrils play two distinct roles depending on their location: they can act as a canopy suppressing oscillations or they can channel low-frequency oscillations into the chromosphere.

As a complementary part of the observational analysis, NLTE and cloud-model codes (e.g., Dineva et al., 2020) used for the inversion of spectral line profiles provide a tool to determine quantitatively various physical parameters of the chromosphere and its structures. The accurate model atmospheres are needed to study, besides other problems, the chromospheric and coronal heating processes. On the other hand, numerical simulations that match well the observational data can provide an accurate synthetic picture of the solar atmosphere and its features. In the recent decades, multi-wavelength observations, improved NLTE codes, MHD simulations, and forward modelling are combined together to study the fine chromospheric structures as well as the sources of the chromospheric heating.

The aim of this thesis is to study the role of acoustic and magnetoacoustic waves in the heating of the solar chromosphere. Observations of strong chromospheric lines of H, Ca II, and Mg II are used to derive semi-empirical models of

the chromosphere and acoustic energy fluxes deposited due to the dissipation of (magneto)acoustic waves. The deposited acoustic energy is then compared to radiative losses integrated over height in the chromosphere. Chapter 2 is focused to the models of solar atmosphere, semi-empirical models, and their scaling. In Chapter 3 are summarized the properties of spectral lines used in this work. Chapter 4 describes in detail the observations and data processing. Radiative cooling and calculation of the deposited acoustic flux are treated in Chapters 5 and 6, respectively. The results of comparison of these two quantities are presented in Chapter 7 and these results are discussed and summarized in Chapter 8.

Chapter 2

Atmospheric models

2.1 Radiative transfer

The atmosphere of the Sun is not at all a vacuum, therefore we expect that the intensity of radiation will not remain spatially constant through the atmosphere. The spatial changes come from the material absorption and emission of radiative field. Transport of radiation is generally described by the "equation of radiative transfer". To derive a general equation for unpolarized radiative transfer, let us first consider $I(\mathbf{r},\mathbf{n},\nu,t)$ as the *specific intensity* at a given position $\mathbf{r}$. The energy is transported by radiation in the frequency range (ν, ν+dν) across an elementary area dS into a solid angle dω in a time interval dt:

$$\mathrm{d}E = I(\mathbf{r},\mathbf{n},\nu,t)\,\mathrm{d}S\cos\theta\,\mathrm{d}\omega\,\mathrm{d}\nu\,\mathrm{d}t, \tag{2.1}$$

where θ is the angle between the direction of propagation $\mathbf{n}$ and the normal to the elementary area dS. The unit of specific intensity is erg cm^{-2} s^{-1} Hz^{-1} sr^{-1} in cgs units and the frequency to wavelength conversion is $I_\lambda = I_\nu\ \mathrm{c}/\lambda^2$, with d$\nu$ and dλ both positively increasing.

The radiative transport depends on absorption and emissivity properties of the medium. The absorption coefficient describes the removal of energy from the radiation field by matter:

$$\mathrm{d}E = \chi(\mathbf{r},\mathbf{n},\nu,t)\ I(\mathbf{r},\mathbf{n},\nu,t)\,\mathrm{d}S\,\mathrm{d}s\,\mathrm{d}\omega\,\mathrm{d}\nu\,\mathrm{d}t \tag{2.2}$$

where ds is an elementary distance along the ray and the unit of χ is cm^{-1}. A photon travels a distance $1/\chi$ before it is absorbed, called the "photon mean free path". The material energy released in the form of radiation into the radiation field can be described by the emission coefficient:

$$\mathrm{d}E = \eta(\mathbf{r},\mathbf{n},\nu,t)\,\mathrm{d}S\,\mathrm{d}s\,\mathrm{d}\omega\,\mathrm{d}\nu\,\mathrm{d}t \tag{2.3}$$

The unit of emission coefficient is erg cm^{-3} s^{-1} Hz^{-1} sr^{-1} in cgs units. In one-dimensional (1D) planar atmosphere, the relation between the vertical distance or geometrical height z and the distance along the ray s is dz=cosθ ds. Hence the general form of the radiative transfer equation (RTE) is given by

$$\mu\frac{\mathrm{d}I}{\mathrm{d}z} = \eta - \chi I \tag{2.4}$$

The intensity I is only a function of z, ν, and the directional cosine μ=cosθ. It can alternatively be written with the optical depth τ as the independent variable

$$\mu \frac{\mathrm{d}I}{\mathrm{d}\tau} = I - S, \tag{2.5}$$

where the ratio of the emission to absorption, S $\equiv \eta/\chi$, is called the "source function". τ and z increase downward and upward in the planar atmosphere, respectively. In the pure-absorption case $\eta = S = 0$, the second term is zero, and we find the simple result that the lower-boundary intensity is just exponentially attenuated.

The integral form of the intensity is called the "formal solution", because the source function is not as a clear function of optical depth. The formal solution of the radiative transfer equation can be obtained as

$$I(\mu, \tau) = I(\mu, \tau_0)\, e^{(\tau-\tau_0)/\mu} + \int_{\tau}^{\tau_0} S(t)\, e^{(\tau-t)/\mu} \mathrm{d}t/\mu \quad ; \quad \mu > 0, \quad \tau < \tau_0 \tag{2.6}$$

where τ_0 is the total optical thickness of the planar slab under consideration, and t is just an integration variable in optical depth. Classical stellar atmospheres are sometimes called "semi-infinite atmospheres", because at the surface τ_0=0, no radiation is illuminating the atmosphere from above, and at the bottom $\tau \to \infty$. The emergent radiation from such an atmosphere has the intensity

$$I(\mu, 0) = \int_{0}^{\infty} S(t) e^{(-t)/\mu} \mathrm{d}t/\mu \tag{2.7}$$

The radiative transfer is explained in more detail by e.g., Mihalas (1978) and Rutten et al. (1995).

2.1.1 TE, LTE, and NLTE

The thermodynamical equilibrium (TE) supports $I_\nu = J_\nu$ (mean intensity) = $S_\nu = B_\nu$(T) (Planck function) for each subprocess and the total source function, therefore the specification of the subprocesses is not essential. The populations of atomic levels are obtained by the Saha-Boltzmann distribution. The kinetic energy follows the Maxwell velocity distribution, with the same temperature in all distribution laws. At each frequency, between each process and the next one, there is a balance, thus no net transport energy and no spectral lines exist.

The local thermodynamical equilibrium (LTE) is an environment where the matter is in equilibrium with the surrounding kinetic temperature, which may vary very slowly through the medium. The radiation could be deviated from this temperature. The distribution is determined by the thermal particle motions, and local collisions more than radiation determine the energy distribution of matter. LTE maintains $S_\nu = B_\nu$(T), $I_\nu \neq B_\nu$(T), $J_\nu \neq B_\nu$(T), and $F_\nu \neq 0$ (non zero energy distribution).

The non local thermodynamical equilibrium (non-LTE or NLTE) works when LTE is not valid, no matter what is valid instead. The level population is computed by means of the statistical equilibrium (SE), a static situation of radiative fields and level populations, and the source function shows deviations from the local Planck function. In other words, it implies that $I_\nu \neq J_\nu \neq S_\nu \neq B_\nu$(T). To

get more details about TE, LTE, and NLTE, the reader can refer to e.g., Rutten et al. (1995).

2.2 Basic equations

Here we present a brief list of basic equations used to construct 1D plane-parallel models of stellar atmospheres in radiative and hydrostatic equilibrium. The following refers to the work of Heinzel (2019), who presented those main equations in a brief and comprehensive manner.

- **Radiative Transfer Equation (RTE)**
  If LTE holds, the source function is simply determined by the surrounding temperature and the absorption coefficient by means of the Saha-Boltzmann laws. The factual form of radiative transfer equation will depend on the method used to solve it. The Feautrier method, one of the popular methods, has been discussed for a single frequency, which uses RTE as a second-order differential equation:

$$\mu^2 \frac{d^2 j_{\mu\nu}}{d\tau_\nu^2} = j_\nu - S_\nu, \tag{2.8}$$

  where $j_{\mu\nu} \equiv (I_\mu$ - $I_{-\mu})/2$ is the so-called Feautrier variable.
  For spectral lines, it is necessary to add another dimension, which covers a grid of frequencies. For most lines, it is known that the assumption of complete frequency redistribution (CRD) over the line profile is usually better than the coherent scattering. In this case, J_ν can be replaced by $\bar{J}$, the frequency-averaged mean intensity, in the source function. By using this it should no longer be necessary to iterate Feautrier solutions for each frequency in the line separately whereas the total radiation redistributed across the line maintains the source function. Rybicki (1971) introduced a refined version of the Feautrier method for all quantities per frequency, e.g., angle and depth vectors, by changing the orders and only the $\bar{J}$ is used within the forward elimination - back substitution scheme. For more detail, see Mihalas (1978) on page 158.

- **Hydrostatic Equilibrium (HE)**
  The stationary atmosphere requires

$$\mu \frac{dp}{dz} = -\rho g, \tag{2.9}$$

  where p is the total pressure, ρ the plasma density, and g the gravity acceleration at the solar surface. It is sometimes common to use the column mass $dm = \rho dz$ and rewrite HE as

$$\mu \frac{dp}{dm} = g \tag{2.10}$$

  The direct solution of this differential equation is $p(m) = gm + p(0)$ in the case of a constant g, where $p(0)$ is the boundary pressure. The total pressure contains the gas, turbulent, and radiation pressures.

$$P_{total} = P_{gas} + P_{turb} + P_{rad} = NkT + \frac{1}{2}\rho v^2 + \frac{4\pi}{c}\int_0^\infty K_\nu d\nu \tag{2.11}$$

Here, N is the total particle number density, K_ν is the second moment of the radiation intensity, and v is the mean microturbulent velocity.

- **Radiative Equilibrium (RE)**
  RE is the simplest constraint on the atmospheric temperature structure. By setting the total energy flux equal to the radiative flux through the atmosphere, the stability requirement becomes a radiative equilibrium condition. Its integral form states that all emissions and absorptions, integrated over the whole spectrum, must be in balance at each atmospheric depth:

$$\int_0^\infty (\eta_\nu - \chi_\nu J_\nu) d\nu = \int_0^\infty \chi_\nu (\eta_\nu - J_\nu) d\nu = L = 0, \tag{2.12}$$

  where L is the net radiative loss function, taken as positive for radiative cooling and negative for radiative heating when RE is not valid. Individual line or continuum transitions contribute to radiative heating or cooling, but total $L = 0$ in RE. Equivalently, we can say that the total radiation flux (first moment of the intensity) is conserved:

$$\int_0^\infty H_\nu d\nu = \frac{\sigma}{4\pi} T_{eff}^4, \tag{2.13}$$

  where $T_{\rm eff}$ is the effective temperature of the star calculated from its luminosity. Solving the radiative transfer equation under RE constraint provides the mean radiation intensity and the source function is equal to Planck function. Opacities are computed in LTE using the Saha-Boltzmann distributions. Net radiative losses in standard photosphere are simply equal to zero at all depths. However, application of this condition to temperature determination is a complex numerical task, especially when the non-LTE conditions and the line blanketing are considered.

- **Statistical Equilibrium Equations (ESE)**
  Statistical equilibrium implies that the radiation fields and atomic level populations for all directions and frequencies do not change with time. Multilevel statistical equilibrium equations in their simplest form are straightforward generalizations of the two level-atom ESE,

$$n_i \sum_{j \neq i} (R_{ij} + C_{ij}) = \sum_{j \neq i} n_j (R_{ji} + C_{ji}), \tag{2.14}$$

  in which R_{ij} and C_{ij} are the radiative and collisional rates, respectively. Contrary to the two-level atom, which only includes bound-bound transitions, the multilevel form contains also the bound-free (ionization) and free-bound (recombination) transitions, i.e., transitions between the bound levels and the continuum states. These population equations for statistical equilibrium are coupled to the RTEs at all frequencies ν. ESEs always depend on $\bar{J}_\nu$ and thus on I_ν in all directions, while the optical thickness τ_ν and source function S_ν in the RTE both again depend on the populations via the absorption coefficient. I_ν and S_ν are usually connected to each other with non linear functions. ESE for all considered atomic and ionic states form a linearly dependent system, and thus one equation must be replaced

by some additional constraint, e.g., the total particle-number conservation for each species: $\sum_i n_i = N_{\rm atom}$.

- **Charge conservation equation**
  The electron density is constrained by the charge conservation, which expresses the electric neutrality of the medium

$$\sum_i n_i Z_i + n_e = 0, \tag{2.15}$$

  in which Z_i is the charge associated with the ionic state i.

- **Auxiliary definition equations**
  In the multilevel atom case, the line absorption and emission coefficients contain all bound-bound, bound-free, and free-free contributions at a given frequency. The general form of the absorption coefficient takes the form

$$\begin{aligned}\chi_\nu = \sum_i \sum_{j>i} [n_i - n_j(g_i/g_j)]\sigma_{ij}(\nu) + \sum_i (n_i - n_j^\star e^{-h\nu/kT}]\sigma_{ik}(\nu) \\ + \sum_k (n_e n_k \sigma_{kk}(\nu, T)(I - e^{-h\nu/kT}] + n_e\sigma_e\end{aligned} \tag{2.16}$$

  The first, second, third and fourth terms correspond to a generalization of the line absorption coefficient, photoionization, free-free continuum opacity, and the Thomson scattering on free electrons. g_i and g_j are the statistical weights and σ corresponds to cross-sections of the included processes. The stimulated emission is included as a negative absorption. The general form of the emission coefficient is given as

$$\begin{aligned}\eta_\nu = (2h\nu^3/c^2)\Bigg[\sum_i \sum_{j>i} n_j(g_i/g_j)]\sigma_{ij}(\nu) + \sum_i (n_i^\star e^{-h\nu/kT}]\sigma_{ik}(\nu) \\ + \sum_k (n_e n_k \sigma_{kk}(\nu, T)\Bigg]\end{aligned} \tag{2.17}$$

  where the emission caused by Thomson scattering is included as an extra term in RTE.

All the basic equations are explained in more detail by, e.g., Mihalas (1978) and Rutten et al. (1995).

2.3 Solar atmospheric models

The solar atmospheric models can be typically classified into four general groups: radiative equilibrium, general equilibrium, semi-empirical, and hydrodynamical models. In the first group, radiative equilibrium models, the outward radiative flux is constant with depth and the temperature distribution is determined by this constraint. These models do not depend on time and there are no sources of non-radiative heating. The temperature decreases with height. The

photosphere of the Sun (the deepest layer of the solar atmosphere), which doesn't show non-radiative heating effects, is a good example of this group (Kurucz, 1991, 1998). For a radiative equilibrium model, one must specify the effective temperature (which determines the total radiative flux), the surface gravity, and the chemical composition of the atmosphere, and then calculate the model atmosphere and the corresponding spectrum to be compared with an observed solar spectrum.

General equilibrium models include the effects of a non-radiative energy flow due to thermal conduction, particle diffusion, and mass flows, and can include a mechanical heating specified in some parametric way. These models are also time-independent and can be used in layers with a very steep temperature gradient. Transition region of the solar atmosphere or transitions from neutral to ionized regions are some of examples for such a model (Fontenla et al., 2002).

In semi-empirical models, the temperature distribution of the atmosphere is determined empirically without considering the energy equation, only by obtaining a good agreement between the spectrum calculated from the model and the observed spectrum. Therefore, the non-thermal heating distribution is derived using the departures from the constant radiative flux. In solar and stellar chromospheres, semi-empirical models show outwardly increasing temperature (Vernazza et al., 1976, 1981), followed by emission features in strong spectral lines. The reader can find more details in the following section (Section 2.4).

Hydrodynamical models simulate dynamical processes and take advantage of their physical properties to include the mechanical heating, which is necessary to explain the observed spectrum. Such models need some initial conditions to get the gas motions started, but then the model relies on internal wave motions to produce the mechanical heating. The aim in such calculations is to include all important physical processes and to match the given observations well enough to have confidence that the simulation is realistic. In case that the hydrodynamical models agree well with observations, these tell us more about the physical mechanisms at work than can be learned from the semi-empirical models, since the latter can indicate only the general properties of the temperature and mechanical heating distributions yielding a given spectrum. In extreme cases, the variations with time in hydrodynamical models can be very large, suggesting that the time-averaged quantities in a corresponding time-independent semi-empirical model may not properly represent the physical conditions in the atmosphere. Examples are the dynamical solar atmospheric models by Carlsson and Stein (1997, 1999). The hydrodynamical calculations are complex, and the results reported by Carlsson & Stein show that the match in some observations is good but it fails in others. (Kalkofen, 2001).

2.4 Semi-empirical models

Semi-empirical models, as earlier mentioned, characterize the temperature and density variations as a function of atmospheric heights. In this way, constructing models can be easy even if non-trivial solutions of other basic equations exist. The plasma temperature is derived by comparing the observed spectrum at each depth with the synthetic spectrum obtained by radiative-transfer calculations for an estimated temperature structure. Therefore, different spectral data in a wide

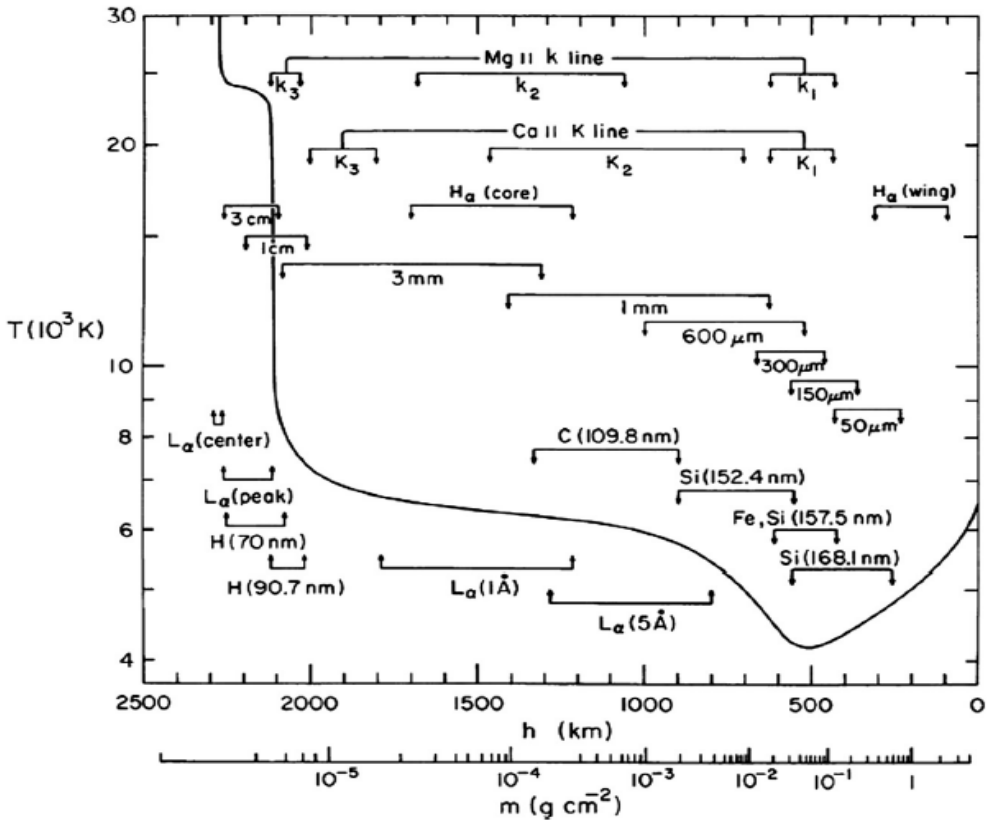

Figure 2.1: The averaged quiet-Sun temperature stratification derived from the EUV continuum, the Lα, and other spectral lines. The approximate formation heights are indicated. h and m stand for the geometrical height and column-mass scales, respectively (Figure from Vernazza et al., 1981).

range of wavelengths are recommended to include in the modeling. It is obvious that different lines and continua form at different atmospheric heights, therefore models are sensitive to different temperatures. Considering critical points of these models, semi-empirical models are still greatly applicable for the solar atmosphere.

For the quiet Sun, the early models introduced by Gingerich and de Jager (1968), were widely developed to the level of standardly used models by Vernazza et al. (1981); these are known as VAL models. They have been constructed, using the PANDORA non-LTE code of Avrett and Loeser (2008), to characterize various solar features. The VAL models contain versions for dark points in the internetwork (VAL A), internetwork area (VAL B), quiet Sun (VAL C), average network (VAL D), bright network (VAL E), and very bright network (VAL F). The "VAL paper" is one of the most cited ones in solar physics. A modification of the models around the temperature minimum between photosphere and chromosphere was discussed by Avrett (1985) and specified in Maltby et al. (1986). At a later period, this set of six models was extended thanks to improvements of the temperature structure in the transition region toward the corona by accounting for ambipolar diffusion (Fontenla et al., 1993, 1999, 2006, FAL models). In addition to quiet-Sun models (FAL A–F), they introduced plage (FAL H), facula (FAL P), bright facula (FAL Q), and sunspot (FAL R, S) models. The most

recent time-averaged statistical semi-empirical model of the average quiet-Sun atmosphere is known as the C7 model (Avrett and Loeser, 2008).

Figure 2.1 shows the averaged classical VAL C model together with formation heights of several chromospheric spectral lines. In low photospheric layers the temperature outwardly decreases until $T_{\rm min} = 4170$ K. This part of the atmosphere roughly corresponds to models in RE. Above h=500 km, the temperature begins to increase with height for the sake of non-thermal heating (waves, magnetic reconnections) and starting ionization of H, which absorbs this energy. Finally, there is a steep temperature gradient toward the transition region and corona and the temperature reaches more than 10000 K in a few hundreds of kilometers. In the chromosphere, the line and continuum source functions may significantly depart from the Planck function (NLTE regime), and thus the spectrum is not a straightforward indicator of the kinetic plasma temperature as it is in the photosphere (LTE regime). Only in the microwave range does the free-free continuum have the Planck source function, which largely simplifies empirical modeling.

2.5 Grid of chromospheric models

The grid of models has to be constructed to match precisely the observed spectral lines originating under different physical conditions in the atmosphere, keeping the number of free parameters as low as possible. We scale the existing set of six semi-empirical 1D hydrostatic models VAL A–F, which describe the solar atmosphere from internetwork to bright network features, by changing independently the temperature (T) and column mass (m) stratifications. Adopting the column mass as an independent variable makes it possible to conserve the condition of hydrostatic equilibrium in the scaled models. To construct the grid of models, we developed an original scaling method (Section 2.5.1) and compared it with an already existing method (Section 2.5.2) proposed by Berlicki et al. (2005). For the model calculations we used the non-LTE radiative-transfer code based on the Multi-level Accelerated Lambda Iterations technique (MALI, Rybicki and Hummer, 1991, 1992) with standard partial frequency redistribution (see Section 3.4 for details). This code was written and kindly provided by Petr Heinzel (Heinzel, 1995).

2.5.1 The scaling method

The original VAL models specify the column mass m, optical depth τ_{500} at 500 nm, temperature T, microturbulent velocity $v_{\rm t}$, hydrogen density $n_{\rm H}$, electron density $n_{\rm e}$, total pressure $P_{\rm tot}$, gas pressure to total pressure ratio $P_{\rm g}/P_{\rm tot}$, and density ρ in 52 geometrical heights z ranging from -75 km to 2400–2700 km ($z = 0$ is at $\tau_{500} = 1$). The microturbulence stratification is practically equal in all models A–F at the heights from -75 km to 2000 km, that is, in the whole photosphere and chromosphere, and it is not changed in scaled models. In Figure 2.2, we show the table of VAL C model as a sample. To improve numerical accuracy of the following computations, we resampled the models to 103 heights by means of the linear interpolation. The scaling of these initial models is done

	h (km)	m (g cm^{-2})	τ_{500}	T (K)	V (km s^{-1})	n_H (cm^{-3})	n_e (cm^{-3})	P_{total} (dyn cm^{-2})	$\frac{P_{gas}}{P_{total}}$	σ (g cm^{-3})
1	2543	5.257-06	0.	447000	11.28	1.005+09	1.205+09	1.440-01	.9896	2.349-15
2	2298	5.365-06	3.712-08	141000	9.87	3.205+09	3.839+09	1.470-01	.9752	7.494-15
3	2290	5.373-06	3.969-08	89100	9.82	5.041+09	5.961+09	1.472-01	.9614	1.179-14
4	2280	5.389-06	4.491-08	50000	9.76	9.038+09	9.993+09	1.477-01	.9318	2.113-14
5	2274	5.404-06	4.952-08	37000	9.73	1.201+10	1.318+10	1.481-01	.9102	2.808-14
6	2271	5.413-06	5.234-08	32000	9.71	1.378+10	1.498+10	1.483-01	.8976	3.222-14
7	2267	5.427-06	5.657-08	28000	9.70	1.567+10	1.677+10	1.487-01	.8840	3.665-14
8	2263	5.443-06	6.124-08	25500	9.68	1.718+10	1.812+10	1.491-01	.8738	4.017-14
9	2255	5.476-06	7.110-08	24500	9.64	1.797+10	1.881+10	1.500-01	.8698	4.203-14
10	2230	5.583-06	1.030-07	24200	9.49	1.862+10	1.943+10	1.530-01	.8718	4.355-14
11	2200	5.716-06	1.426-07	24000	9.33	1.932+10	2.009+10	1.566-01	.8645	4.517-14
12	2160	5.902-06	1.977-07	23500	9.08	2.051+10	2.120+10	1.617-01	.8778	4.795-14
13	2129	6.055-06	2.427-07	23000	8.87	2.163+10	2.219+10	1.659-01	.8801	5.058-14
14	2120	6.101-06	2.562-07	22500	8.81	2.231+10	2.276+10	1.672-01	.8789	5.216-14
15	2115	6.128-06	2.640-07	21000	8.78	2.403+10	2.402+10	1.679-01	.8710	5.619-14
16	2113	6.140-06	2.674-07	18500	8.77	2.732+10	2.620+10	1.682-01	.8539	6.390-14
17	2109	6.172-06	2.754-07	12300	8.74	4.092+10	3.306+10	1.691-01	.7839	9.569-14
18	2107	6.193-06	2.801-07	10700	8.72	4.673+10	3.535+10	1.697-01	.7552	1.093-13
19	2104	6.228-06	2.877-07	9500	8.71	5.239+10	3.705+10	1.706-01	.7277	1.225-13
20	2090	6.416-06	3.243-07	8440	8.60	6.127+10	3.799+10	1.758-01	.6986	1.433-13
21	2080	6.564-06	3.507-07	8180	8.55	6.541+10	3.780+10	1.798-01	.6891	1.530-13
22	2070	6.722-06	3.770-07	7940	8.50	6.960+10	3.783+10	1.842-01	.6808	1.628-13
23	2050	7.066-06	4.299-07	7660	8.42	7.705+10	3.792+10	1.936-01	.6701	1.802-13
24	2016	7.732-06	5.203-07	7360	8.22	9.075+10	3.811+10	2.118-01	.6616	2.122-13
25	1990	8.322-06	5.903-07	7160	8.01	1.033+11	3.858+10	2.280-01	.6600	2.417-13
26	1925	1.015-05	7.717-07	6940	7.63	1.380+11	4.028+10	2.780-01	.6620	3.227-13
27	1785	1.647-05	1.212-06	6630	6.92	2.601+11	4.771+10	4.511-01	.6772	6.082-13
28	1605	3.407-05	1.958-06	6440	5.85	6.386+11	6.005+10	9.334-01	.7262	1.493-12
29	1515	5.144-05	2.420-06	6370	5.26	1.048+12	6.456+10	1.409+00	.7595	2.450-12
30	1380	1.012-04	3.286-06	6280	4.51	2.273+12	7.600+10	2.774+00	.8051	5.315-12
31	1280	1.747-04	4.084-06	6220	3.92	4.200+12	7.486+10	4.786+00	.8423	9.822-12
32	1180	3.112-04	5.075-06	6150	3.48	7.865+12	8.108+10	8.527+00	.8694	1.839-11
33	1065	6.299-04	6.861-06	6040	2.73	1.711+13	9.349+10	1.726+01	.9136	4.000-11
34	980	1.098-03	9.148-06	5925	2.14	3.147+13	1.041+11	3.008+01	.9440	7.359-11
35	905	1.840-03	1.239-05	5755	1.70	5.546+13	1.049+11	5.043+01	.9628	1.297-10
36	855	2.632-03	1.553-05	5650	1.53	8.135+13	1.064+11	7.210+01	.9691	1.902-10
37	755	5.577-03	2.537-05	5280	1.23	1.864+14	8.838+10	1.528+02	.9784	4.358-10
38	705	8.333-03	3.288-05	5030	1.09	2.935+14	7.664+10	2.283+02	.9821	6.864-10
39	655	1.276-02	4.452-05	4730	.96	4.794+14	8.085+10	3.495+02	.9852	1.121-09
40	605	2.013-02	7.022-05	4420	.83	8.119+14	1.112+11	5.516+02	.9881	1.899-09
41	555	3.270-02	1.456-04	4230	.70	1.382+15	1.733+11	8.958+02	.9912	3.232-09
42	515	4.878-02	3.014-04	4170	.60	2.096+15	2.495+11	1.336+03	.9934	4.902-09
43	450	9.378-02	1.017-03	4220	.53	3.989+15	4.516+11	2.569+03	.9949	9.327-09
44	350	2.481-01	5.626-03	4465	.52	9.979+15	1.110+12	6.798+03	.9954	2.334-08
45	250	6.172-01	2.670-02	4780	.63	2.315+16	2.674+12	1.691+04	.9936	5.413-08
46	150	1.433+00	1.117-01	5180	1.00	4.917+16	6.476+12	3.926+04	.9854	1.150-07
47	100	2.118+00	2.201-01	5455	1.20	6.866+16	1.066+13	5.804+04	.9801	1.606-07
48	50	3.056+00	4.395-01	5840	1.40	9.203+16	2.122+13	8.274+04	.9748	2.152-07
49	0	4.279+00	9.953-01	6420	1.60	1.166+17	6.433+13	1.172+05	.9702	2.727-07
50	-25	4.991+00	1.683+00	6910	1.70	1.261+17	1.547+14	1.368+05	.9688	2.949-07
51	-50	5.747+00	3.338+00	7610	1.76	1.317+17	4.645+14	1.575+05	.9697	3.080-07
52	-75	6.534+00	7.445+00	8320	1.80	1.365+17	1.204+15	1.790+05	.9711	3.192-07

Figure 2.2: Table of atmospheric parameters of the VAL C model (Table 12 of Vernazza et al., 1981).

in two steps: (1) m and T stratifications are changed and (2) the other model quantities are recalculated.

We can find an adequate way to change m and T by adopting, for example, the VAL C model as the initial one and reproducing the stratifications of all the other

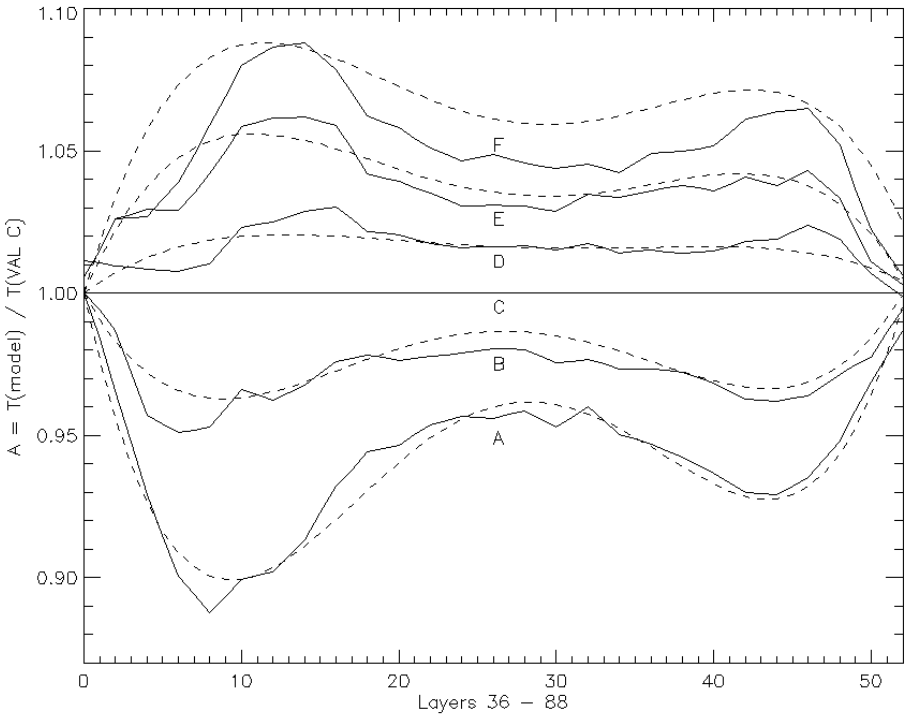

Figure 2.3: Temperature stratifications of models VAL A–F normalized to VAL C (solid lines) in the range z from 2100 km to 250 km. Dashed lines show the approximation by fourth-order polynomials.

VAL models. In general, the scaling algorithm must be able to reproduce all the stratifications using any VAL model as the initial one. The following solution was adopted: The initial column mass stratification $m_0(z)$ is changed for $z \geq 450$ km ($m < 0.1$ g cm^{-2}) whereas it is kept unchanged in deeper layers. The changes are controlled by scaling parameter p_m, so that the scaled column mass is

$$
\begin{aligned}
m_\mathrm{x} &= b_\mathrm{x} m_{0\mathrm{x}}, \quad \text{where} \\
b_\mathrm{x} &= p_\mathrm{m} \quad \text{for} \quad z \geq 2000 \text{ km} \\
b_\mathrm{x} &= p_\mathrm{m} + (1 - p_\mathrm{m})\, x \,/\, (x_{450} - x_{2000}) \quad \text{for} \quad 2000 \text{ km} > z \geq 450 \text{ km},
\end{aligned}
$$

and x is the sampling (row) index in the model table. In upper layers, from the maximum height down to $z \approx 2000$ km, b_x is simply a multiplicative factor equal to p_m. In deeper layers ($z < 2000$ km), this factor linearly decreases or increases to reach unity at $z \approx 450$ km.

The initial temperature stratification is changed in the range of heights from approximately 250 km to 2100 km; the upper and lower parts remain equal to the initial model. To derive the scaling parameter p_T, we normalize the temperature stratifications T_x of all VAL models to VAL C: $A_\mathrm{x} = T_\mathrm{x} / T_{\mathrm{xVALC}}$ (Figure 2.3). These normalized stratifications can be approximated by a fourth-order polynomial in the form $A'(x) = 1 + \sum_{i=1}^{4} a_i x^i$. The coefficients a_i (Figure 2.4) are mutually dependent and a_{2-4} can be expressed by multiples of a_1 (Figure 2.5), particularly, $a_{\mathrm{i}=2,3,4} = a_1 q_\mathrm{i}$, where $q_\mathrm{i} = [-7.90 \times 10^{-2}, 2.21 \times 10^{-3}, -2.03 \times 10^{-5}]$. The values of q_i are practically independent of the initial model. Thus, a_1 can be used as the temperature scaling parameter, $p_\mathrm{T} = a_1$. The scaled temperature

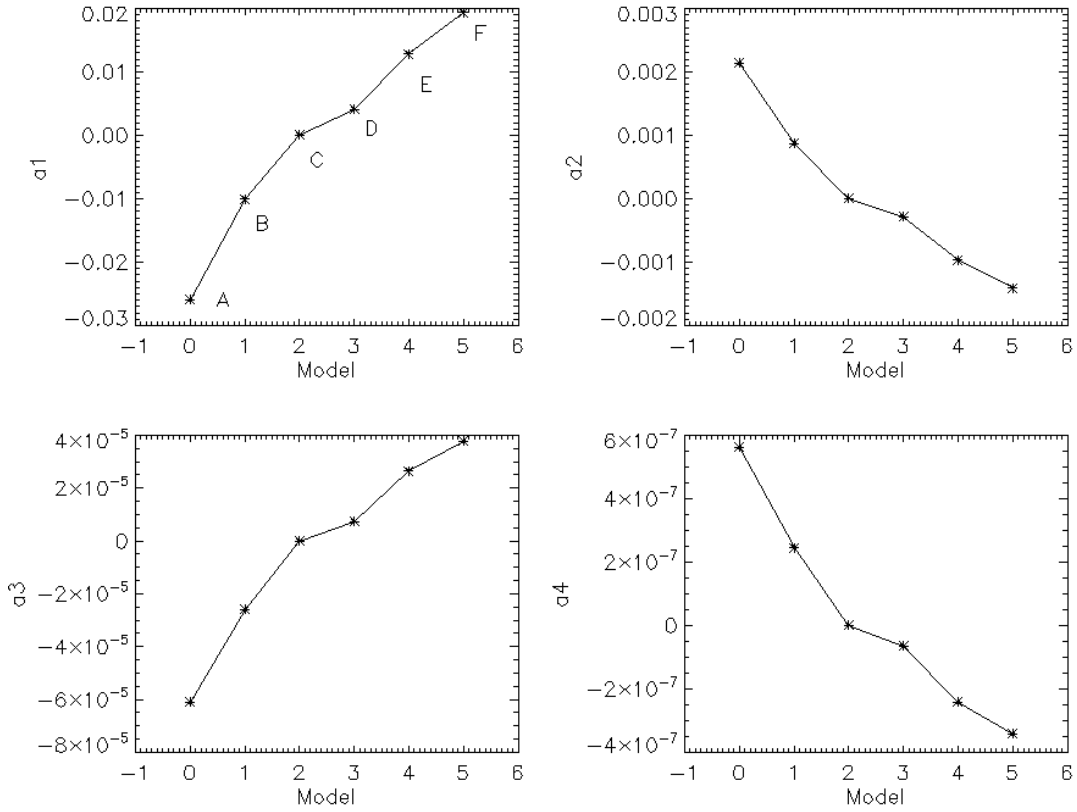

Figure 2.4: Coefficients a_{1-4} of the fourth-order polynomials versus models VAL A–F.

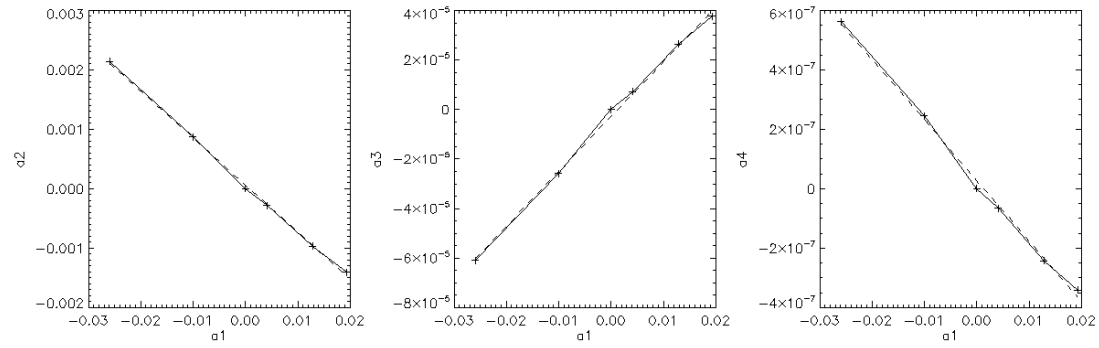

Figure 2.5: Dependence of the coefficients a_{2-4} on the coefficient a_1 (solid) and its linear approximation (dashed).

stratification (in the range 250–2100 km) is then calculated as

$$T_{\rm x} = T_{0\rm x}(1 + p_{\rm T}x + p_{\rm T}\sum_{i=2}^{4} q_{\rm i}x^i),$$

where T_{0x} are the initial temperatures.

For each of the initial VAL models we calculated a grid of 2806 scaled models using a combination of the parameters $p_{\rm m}$ = [0.5, 0.6, ..., 4.9, 5.0] and $p_{\rm T}$ = [-0.030, -0.029, ..., 0.029, 0.030]. In Figure 2.6, we show that the models

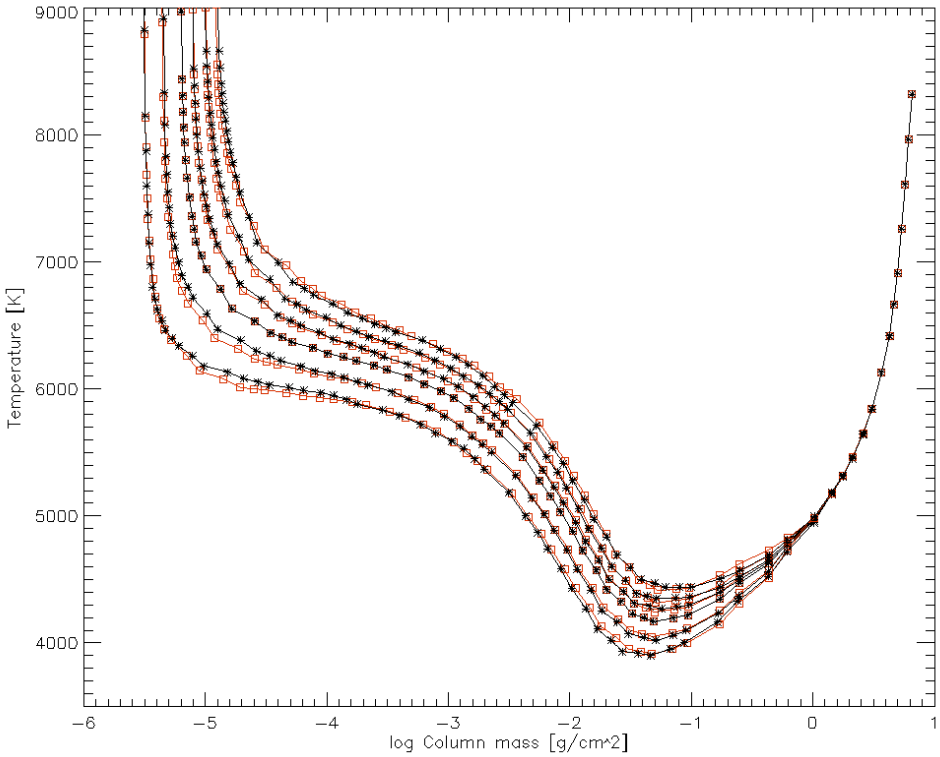

Figure 2.6: Temperature versus column mass of the VAL A–F models scaled from the model C. Red and black lines show the scaling results and the original VAL models, respectively. The symbols denote sampling of the models.

VAL A-F can be reproduced by scaling the model C, applying the sets of parameters $p_{\rm m}$ = [0.5, 0.7, 1.0, 1.3, 1.6, 2.0] and $p_{\rm T}$ = [−0.021, −0.010, 0.000, 0.006, 0.012, 0.020], respectively. In total, we have 16836 individual pre-computed models in the grid parametrized by $p_{\rm m}$, $p_{\rm T}$, and the initial model selection. This scaling method and obtained results were published in Abbasvand et al. (2020a).

2.5.2 Alternative scaling method

Another method to scale the VAL models using only two parameters m and T was introduced by Berlicki et al. (2005). The column mass is scaled by adding a constant m_0 to the stratification of the model VAL C:

$$m_{\rm x} = m_{\rm x,VALC} + m_0$$

The temperature is scaled by adding a constant temperature difference $\triangle T$ multiplied by a normalized column-mass difference:

$$T_{\rm x} = T_{\rm x,VALC} + \triangle T(m_1 - m_x)/m_1, \quad \text{for } m_{\rm x} < m_1$$

where m_1 is a column mass at the depth below which T is fixed to VAL C. Setting m_1 = 0.6172 g cm^{-2} (z=250 km, T=4780 K of VAL C), $\triangle T$ = [−370, −200, 0, 100, 230, 370] K and m_0 = [-3.1996×10^{-6}, -1.7990×10^{-6}, 0, 1.336×10^{-6}, 3.962×10^{-6}, 6.196×10^{-6}] g cm^{-2} for models A–F, we can approximate the $T_{\rm x}$ versus $m_{\rm x}$ stratification of all the VAL models. In Figure 2.7 we show how the

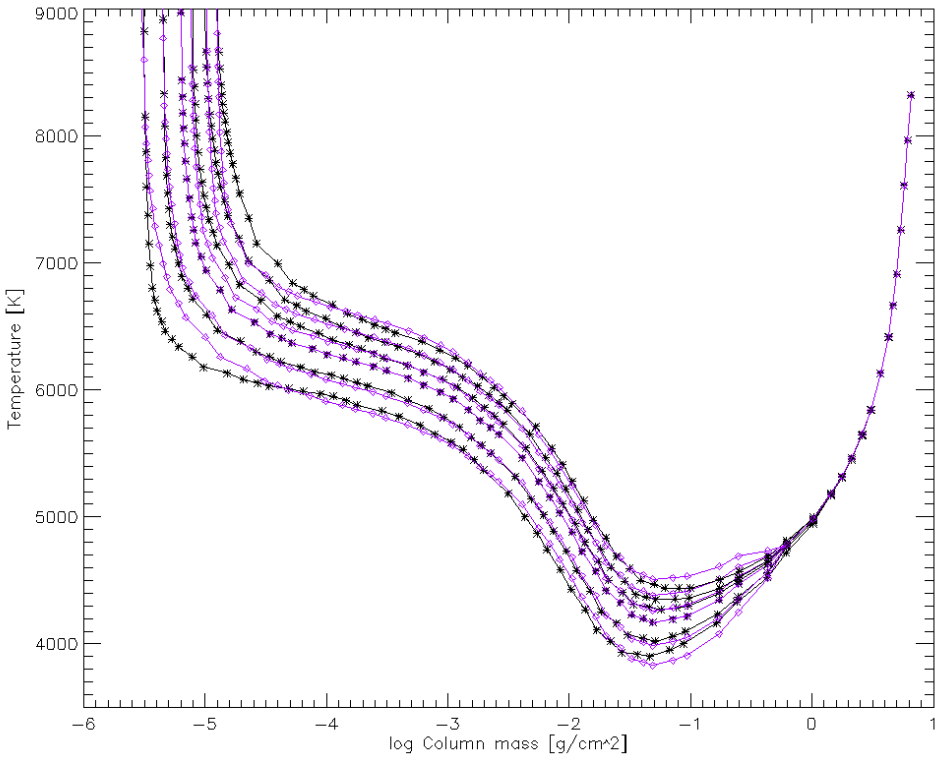

Figure 2.7: Temperature versus column mass of the VAL A–F models scaled from the model C using the alternative method. Violet and black lines show the scaling results and the original VAL models, respectively. The symbols denote sampling of the models.

models VAL A–F can be reproduced by scaling the model C, applying the sets of parameters listed above.

We have presented two methods to scale the temperature and column-mass parameters in a solar atmospheric model. Our method uses a VAL model as reference (for example the VAL C average quiet-Sun model) and two free parameters to solve the scaling in the range of other VAL models. In other words, the VAL models are reproducible via any other of VAL models. A comparison of results of both methods (see Figures 2.6 and 2.7) shows that the first method reproduces the VAL models well in the whole range from the low photosphere to the transition region. The second alternative method shows considerable deviations from the original VAL models around the temperature minimum (-1.5 $<$ log m $<$ -0.6) and in upper chromosphere (-5.4 $<$ log m $<$ -4.3). Hence the first method is more suitable to reproduce all the VAL models by scaling one of them. The success of this method in fitting different spectral lines in many different observations analyzed in this work is a demonstration of the validity of our approach. Our database of scaled models together with synthetic line profiles, radiative losses, and contribution functions is published in the web page `https://www.asu.cas.cz/~sdsa/VAL-database/`.

Chapter 3

Spectral lines

An atom is generally composed of a positively charged atomic nucleus and negatively charged electrons. From quantum mechanics, it is known that the electrons stay in discrete energy levels within the atom. As an electron transits from a higher energy level to a lower one, the extra energy is emitted in the form of electromagnetic radiations with a specific wavelength. Since the energy differences between the energy levels are discrete, the emission spectrum of the atom must also have discrete lines of different wavelengths.

In an atom with charge $+Ze$ and N electrons, the Hamiltonian energy operator can be written as follows:

$$H = \sum_{i=1}^{N} \left(\frac{-\hbar}{2m} \nabla_i^2 - \frac{Ze^2}{4\pi\varepsilon_0 r_i} \right) + \sum_{i<j=1}^{N} \frac{e^2}{4\pi\varepsilon_0 r_{ij}} + \sum_{i=1}^{N} \xi(r_i)(\bar{l}_i * \bar{s}_i) \tag{3.1}$$

where r_i is the distance between an electron and the nucleus and $r_\mathrm{ij} = \mid \bar{r}_\mathrm{i} - \bar{r}_\mathrm{j} \mid$ is the distance between two electrons i and j. The first sum demonstrates the radial part of the kinetic (first term) and potential (second term) energy of all electrons in the field around the nucleus. The second sum represents the potential energy from the repulsion between the electrons. The third sum adds the potential energy originating from the magnetic interaction between the spin of the electrons s (the magnetic moment) and the orbital motion of the electrons l (the magnetic field). $\hbar = h/2$ is the reduced Planck's constant, m the mass of the electron, ∇_i is the Laplace operator acting on the wave function for each electron in the Schrödinger equation, e the charge of the electron, l_i the angular momentum of the electron and its spin s_i. The function $\xi(r_\mathrm{i})$ is proportional to $1/r_\mathrm{i}$ and $\mathrm{d}V(r_\mathrm{i})/\mathrm{d}r_\mathrm{i}$, where $V(r_\mathrm{i})$ is the potential (for more detail see e.g., Cowan, 1981).

An electron under collision can be excited to any level, nevertheless, de-excitation of a photon to lower levels must be controlled by a set of LS-coupling rules. In LS-coupling, the contribution to the energy due to the non-central electron-electron repulsion and the contribution from the magnetic spin-orbit interaction are included. LS-coupling is valid when the non-central interaction is much bigger than the spin-orbit interaction (for the other way around the system is described by jj-coupling). It works best for the lightest elements, but it is quite good for medium heavy elements as well. With LS-coupling we get new quantum numbers L, S and J that are related as follows: $\bar{J} = \bar{L} + \bar{S}$. The quantum number L is the total orbital angular momentum, S represents the total spin

angular momentum and J is the total angular momentum. L and S are given by $| l_1 - l_2 | \leq L \leq l_1 + l_2$ and $| s_1 - s_2 | \leq S \leq s_1 + s_2$.

The level of a configuration is shown by ${}^{2S+1}L_J$, where ${}^{2S+1}L$ is the term and $2S+1$ is the multiplicity of the term. The multiplicity tells us the maximum number of levels a term can have, e.g. $2S+1=1$ depicts that the term is a singlet while $2S+1=3$ indicates that the term is a triplet. The rules that an electron has to follow for a transition are:

1. $\Delta L = 0, \pm 1$ where 0 to 0 is forbidden.
2. $\Delta S = 0$; (1) and (2) are only valid in LS-coupling
3. $\Delta J = 0, \pm 1$ where 0 to 0 is forbidden.
4. $\Delta \pi =$ yes, π stands for parity and *yes* means that the parity has to change. The parity operator can be either 1 (even) or -1 (odd).

During the transition between two levels, the photon takes the parity 1 and this rule is necessary. Since parity depends on l, the rule can also be written: $\Delta l = \pm 1$. Transitions that do not follow these rules are called forbidden lines, which does not have to mean that they are forbidden, but only less probable than the others. This holds for atoms that can be described by LS-coupling. However, this approximation does not work perfectly for all elements and sometimes the rules are broken. Transitions that do not follow ΔS are called intercombination lines (see e.g., Thorne et al., 1999).

3.1 Ca II 854.2 nm

Calcium is an atom with two electrons in a closed s shell. The spectrum of Ca is somewhat similar to that of He in that singlet and triplet excited systems. In addition, in calcium we have bound states where both of the s electrons are excited. Singlet states are levels where one electron is in the $4s$ state and the other electron is in some other state with the spins adding to zero angular momentum, $S = 0$. Core electrons at $1s$, $2s$, $2p$, $3s$ and $3p$ levels require a great deal of energy to remove and no important excited states of unionized Ca involves this kind of excitation. On the other hand, triplet states are analogous to the singlet states but with S = 1. There is a triplet state for every singlet state except for the ground state. In this case, because both electrons are in the same state, only the S = 0 state is permitted by the Pauli exclusion principle. Figure 3.1 shows Ca I and Ca II spectral lines.

Calcium is one of the best studied elements in the visible and near infrared spectrum of cool stars. Calcium lines cover a wide variety of excitation conditions and line strengths. The strongest Ca II H&K spectral lines (396.8 and 393.3 nm) are results of electron transitions between the $4s^2S_{1/2}$ level to the $4p^2P_{1/2}$ and $4p^2P_{3/2}$ levels, respectively.

The infrared triplet lines of ionized calcium at 849.8, 854.2 and 866.2 nm, which correspond to transitions from the $3d^2D_{3/2}$ and $3d^2D_{5/2}$ levels to the $4p^2P_{1/2}$ and $4p^2P_{3/2}$ levels, are important features in this spectrum range. Extended wings of these strong lines show a good signature of the temperature distribution in the

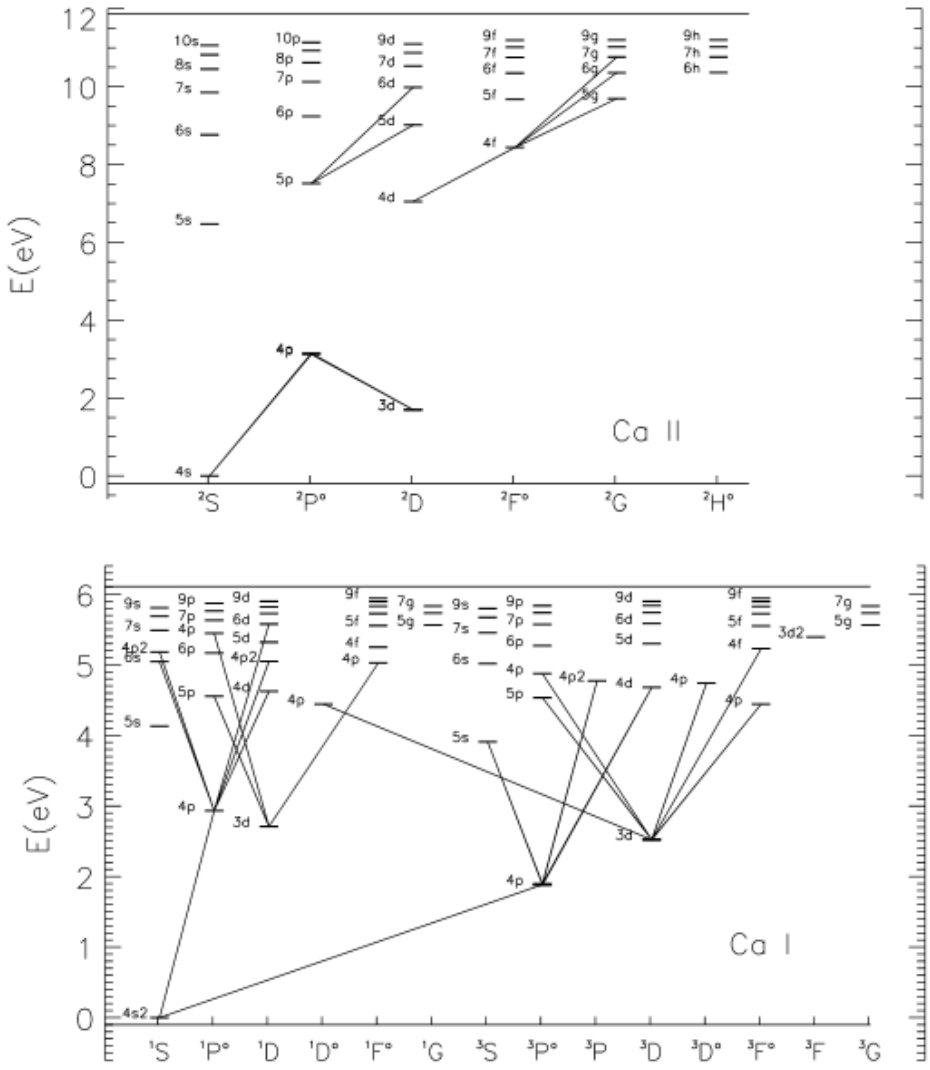

Figure 3.1: A diagram of the Ca I and Ca II spectral lines used in Ca abundance analysis arise in the transitions shown as continuous lines. The figure is provided through the courtesy of Mashonkina et al. (2011).

deeper atmosphere of the Sun. Their cores, formed in the chromosphere, are quite sensitive to the degree of chromospheric activity and Doppler velocities. The mostly used line Ca II 854.2 nm is a result of the transition between the levels $3d^2D_{5/2}$ and $4p^2P_{3/2}$.

The first fully detailed study of all useful calcium lines in the solar spectrum was presented by Holweger (1972). According to this study, the abundance of the solar calcium spectrum in both visible and near infrared spectral region is 46 lines with known f-values, including resonance, forbidden and auto-ionizing lines. All transitions involved in the solar calcium spectrum are in the range from 0 eV lines of Ca I to 7.5 eV lines of Ca II and include auto-ionizing lines. In photospheric spectrum, neutral and singly ionized calcium are most detectable lines.

In the solar atmosphere, the statistical equilibrium of the level populations in a Ca model atom consisting of 16 levels of Ca I, 3 levels of Ca II, and the ground state of Ca III was studied by Watanabe and Steenbock (1985). They claimed that there is no significant departure from LTE populations in the Ca II levels,

and the global NLTE effects on the determination of the calcium abundance are very small.

Jorgensen et al. (1992) investigated specifically the effects of departures from LTE on the Ca II triplet lines using the MARCS photospheric model. The model of calcium atom was used comprising 8 levels in Ca I, 5 levels in Ca II, plus the ground state of Ca III. They widely discussed the departure effects on the combined integrated equivalent widths and the effect of rising temperature on the central core intensities. They derived that if the Ca II IR triplet line wings are formed in conditions close to LTE, the line core should be in NLTE. The largest NLTE effects are found at high temperature $T_{\rm eff}$ and gravity g. The dependence of the equivalent width on gravity is higher at higher metallicities. At low metallicities, the dependence on log g is less than that on $T_{\rm eff}$.

Linsky (1970) argued that the Ca II H&K spectral lines show a similar effect. The Ca II H line has half the opacity as the K line, and hence its source function thermalizes at a slightly lower height than the source function of the K line. This means that the K source function follows the temperature rise more strongly in chromosphere than the H line, and hence the K emission peaks are more intense.

3.2 Hydrogen lines

3.2.1 Hα 656.28 nm

The first line in the Balmer series is Hα, which is located at 656.28 nm in the electromagnetic spectrum. The spectral line is the result of radiative transition between the levels n=2 and n=3. It is the strongest visible spectral line of neutral hydrogen originating in the chromosphere and one of the most important lines for studying chromospheric structures. Hydrogen is the lightest element in the universe and hence it is most sensitive to thermal broadening. Since Hα has a broad line profile, is not much sensitive to Doppler shifts. All electron transitions in Lyman, Balmer, Paschen and Brackett series are shown in Figure 3.2.

For two reasons Hα is a strong absorption line in the solar spectrum: First hydrogen is the most abundant element in the Sun and the Universe. Second due to the Sun's effective temperature $T \approx 5800$ K, the second level of hydrogen is populated and makes possible the absorption in Hα. The chromosphere observed in Hα exhibits many rich structures, caused by absorption by gas ejecta, Doppler shifts of the line profile in fast gas flows along magnetic fields, and channeling of photons around absorbing features.

3.2.2 Hβ 486.13 nm

The second line in the Balmer series is Hβ line which is located at 486.13 nm in the electromagnetic spectrum. The spectral line is the result of radiative transition between levels n=2 and n=4. The profile of Hβ is one of the most studied line-shapes in the optical emission plasma spectroscopy. As for all other hydrogen lines, the plasma broadening is governed by the linear Stark effect which makes the line shape very sensitive to the micro-field of the charged particles (electrons and ions). Hβ is a candidate for plasma diagnostic for the sake of its high sensitivity to the density of charged particles.

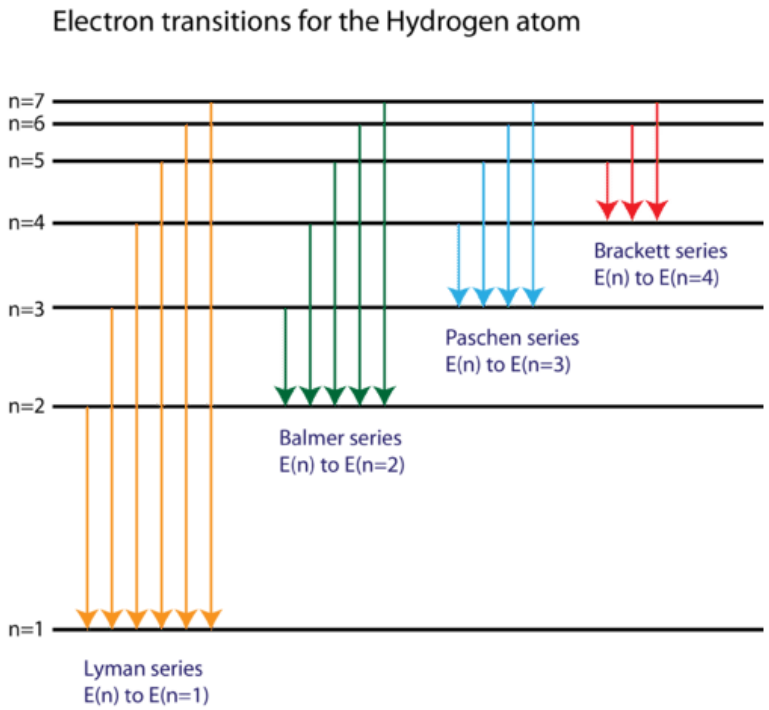

Figure 3.2: A diagram of the hydrogen spectral lines. n is the principle quantum number.

3.3 Mg II k&h

One of the most abundant elements in the solar atmosphere is neutral magnesium and its singly ionized state, which give rise to a number of spectral lines that diagnose the physical properties of the photosphere as well as in the chromosphere. For example, the Mg I 457.1 nm forbidden line allows us a photospheric temperature diagnostic. Another line, the Mg I b line around 517 nm is a helpful line for lower chromospheric magnetic field diagnostic. The Mg I 12 μm infrared lines are good exhibitors of a peculiar non-LTE radiative transfer behavior (Chang et al., 1991). The Mg I 285.2 nm resonance line shows effects of partial frequency redistribution (PRD, Uitenbroek and Briand, 1995). Eventually the Mg II k&h resonance doublet at 279.55 nm and 280.27 nm, respectively, are the strongest lines in the solar spectrum observed in the middle of the UV range. There are no ground-based observation for those.

The Mg k&h lines are transitioned from the $3s^2S$ ground state to the $3p^2P$ excited states. Close to these lines, there is a triplet of transitions between the $3p^2P$ and $3d^2D$ states. One of the triplet lines with a wavelength of 279.08 nm is located in the blue wing of the k core, the other two lines at 279.79 nm and 279.80 nm are located in between the k&h line cores. The triplet lines can potentially be used as an indicator of velocity in the lower chromosphere.

The recent study by Asplund et al. (2009) shows that magnesium is about 18 times more abundant than calcium in solar atmosphere, therefore the Mg II k&h lines form correspondingly higher heights of atmosphere than the analogous Ca II H&K lines, where the H&K lines regularly lack emission reversals altogether, or exhibit singly peaked profiles (Rezaei et al., 2008). On the other side, the k&h lines always have doubly peaked emission reversals, except in sunspots (Morrill

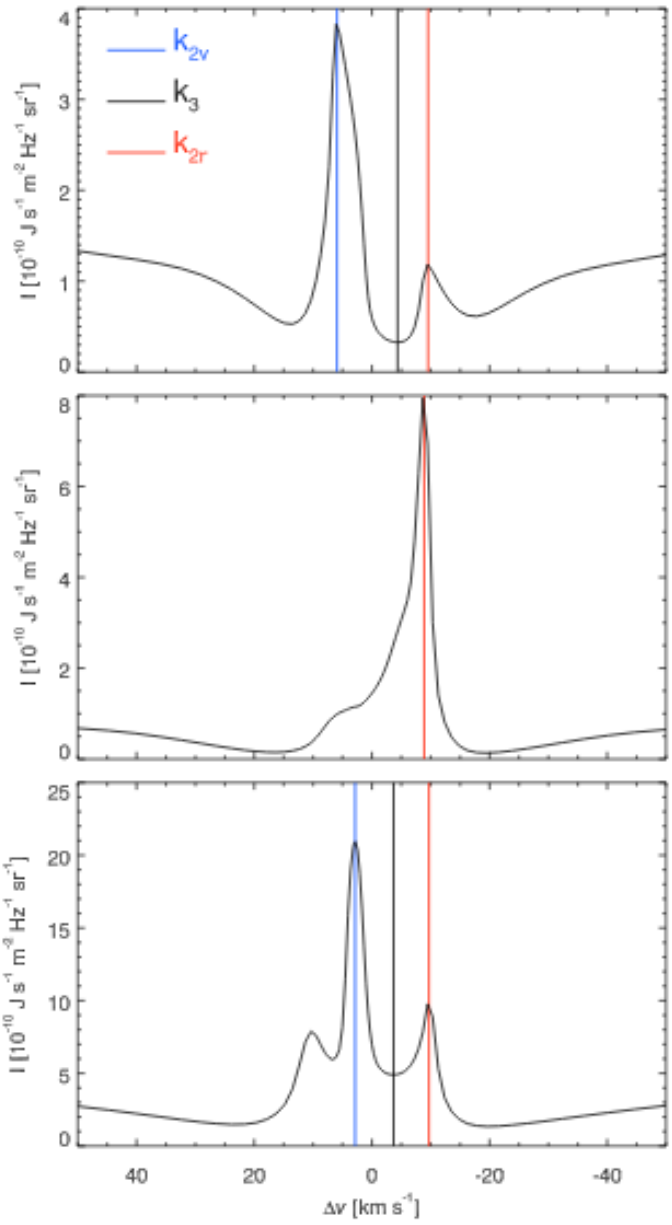

Figure 3.3: Example Mg II k line profiles with the identification of k_{2v}, k_3, and k_{2r} features. *Top*: standard profile with two emission peaks and a central depression. *Middle*: profile showing only one emission peak on the red side of the rest line-center wavelength. *Bottom*: profile showing three emission peaks. The vertical blue, black and red lines indicate the wavelength position of k_{2v}, k_3 and k_{2r}. The figure is provided through the courtesy of Leenaarts et al. (2013).

et al., 2001). On top of that, the high profile asymmetry of the Ca II H&K lines is related to the result of acoustic waves steepening into shocks (Carlsson and Stein, 1997), which is much less in the k&h lines (Gouttebroze, 1989).

The Mg II k&h resonance lines have shown to be a great-potential tool to study the solar chromosphere, sampling layers from the temperature minimum to the upper chromosphere. The solar spectra of each line are often characterized by a central emission reversal (central absorption, k_3, h_3), surrounded by two emission

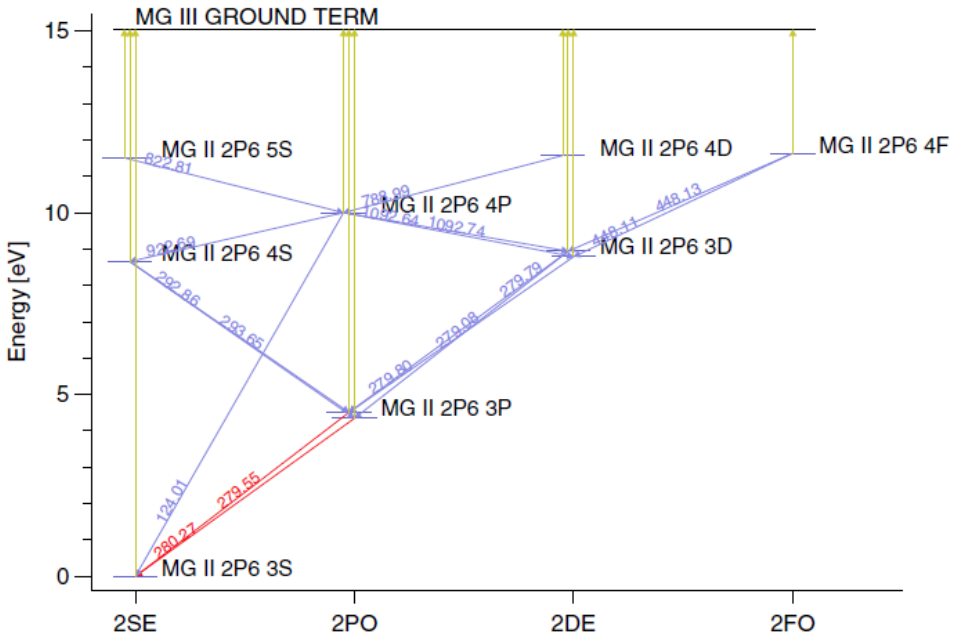

Figure 3.4: A diagram of the 10 level plus continuum Mg II atomic model. The red transitions indicate the Mg II h&k lines, all other bound–bound and bound-free transitions are blue and yellow, respectively. All bound-bound transitions are interpreted with the line-center wavelength in nanometers. The figure is provided through the courtesy of Leenaarts et al. (2013).

peaks (k_{2v}, k_{2r}, h_{2v}, h_{2r}). The emission peaks form in the middle chromosphere, where decoupling between their source function and the Planck function occurs. The central reversal forms at the height 200 km below the transition region, where the decoupling is even stronger than in the emission peaks. The k line is formed by few tens of kilometers slightly higher in the atmosphere than the h line, because its opacity is higher by a factor of two than that of the h line (Leenaarts et al., 2013).

The spectra of Mg II k&h lines show a wide range of profiles in different regions. Profiles with more than two peaks indicate a combination of different structures with different velocities along the line of sight (LOS). Based on the main characteristics of the profiles, we divide them into three groups: A) central-reversed (standard) profiles, B) single-peaked profiles, and C) complex profiles that may have more than two peaks. In the top panel of Figure 3.3, we show a standard profile with well-defined features. The middle panel shows a profile with only one emission peak, because it has a wavelength larger than the rest line-center wavelength. The bottom panel shows a triple-peaked profile. For profiles with three or more peaks it is not a priori clear which features to select.

The atomic structure between singly ionized calcium and magnesium differs slightly, hence NASA's Interface Region Imaging Spectrograph (IRIS, De Pontieu et al., 2014) provides an interesting opportunity for simultaneous temperature and velocity diagnostics. While the Ca II $3d^2D$ levels have a lower energy by about 1.3 eV than the $4p^2P$ upper levels of the H&K lines, and thus allow for the $4d^2D$–$4p^2P$ Ca II triplet to form in the infrared, the Mg II $3d^2D$ levels lie at about the same energy difference above the $3p^2P$ levels as these levels lie above

the Mg II $3s^2S$ ground state. As a result, the $3d^2D$–$3p^2P$ triplet forms in the UV, very close to the k&h resonance lines, overlapping with them in wavelength. Figure 3.4 exhibits a 10 level plus continuum model atom for Mg II.

The Mg II k&h lines are resonance lines, consequently the radiative damping is the largest contribution to their total line broadening. The most important contribution to the radiative damping is the Van der Waals interaction during the collisions with neutral atoms of hydrogen in the photosphere. Therefore, the Mg II k&h lines have very broad wings because of their large opacity in the photosphere. The combined k&h line opacity at the height $z = 200$ km in the quiet-Sun model (FAL C) becomes equal to the continuum opacity at 277.25 nm and 282.34 nm, more than 2 nm away from the nearest k&h line-center wavelength. For comparison, the Doppler half-width ($\sqrt{2kT/m}$) of the k&h lines at typical chromospheric temperatures is between 2–3 km s^{-1}, that is, ~ 0.003 nm. Linsky and Avrett (1970) discussed that the Mg II k&h and Ca II H&K spectral lines behave qualitatively in the same way. Later, in other analysis, this was confirmed by Leenaarts et al. (2013).

3.4 Fit of synthetic to observed line profiles

The initial models VAL A–F, including the column mass m, optical depth τ_{500} at 500 nm, temperature T, microturbulent velocity $v_{\rm t}$, hydrogen density $n_{\rm H}$, electron density $n_{\rm e}$, total pressure $P_{\rm tot}$, gas pressure $P_{\rm g}$, and density ρ, are scaled by changing two free parameters that define the T and m stratifications (see Section 2.5.1). These stratifications are used as inputs in the non-LTE radiative-transfer code kindly provided by Petr Heinzel. This code is based on the Multi-level Accelerated Lambda Iterations technique (MALI) with preconditioning of the statistical-equlibrium equations according to Rybicki and Hummer (1991, 1992). The density structure is obtained from the hydrostatic equilibrium for a given temperature structure and the radiative transfer equation is solved in a semi-infinite atmosphere subject to standard boundary conditions. First the hydrogen problem using a 5-level plus continuum atomic model is solved (Heinzel, 1995). To obtain the gas density, the helium is added but the helium ionization in computing the electron density within the atmosphere is neglected. The hydrogen resonance lines Lα and Lβ are synthesized with standard angle-averaged partial frequency redistribution (PRD) for the scattering part of the source function. All other hydrogen lines are treated in the complete redistribution. The microturbulence, taken from the initial VAL model, is consistently included in the hydrostatic equilibrium as the turbulent pressure and it enters also in the line broadening calculations.

The resulting electron densities are then used, together with the temperature structure, in the Ca II and Mg II versions of the MALI code. The first one solves the non-LTE problem for a 5-level plus continuum model of Ca II–Ca III ions. This governs the Ca II H and K resonance lines, the Ca II infrared triplet lines and the five continua. Again, PRD is used for both resonance lines H&K. The detailed synthesis of the Ca II 854.2 nm line is performed, using all relevant broadening mechanisms. The Mg II version uses a 5-level plus continuum Mg II–Mg III atomic model and treats the two resonance lines Mg II k&h and the triplet lines. Both resonance lines are again computed using the PRD approach.

The mean observed profiles of all studied lines are obtained by averaging over the observing periods of the line profiles with removed Doppler shifts. To compare a synthetic line profile with an actual mean observed one, the least-squares method is used. It provides a way to test how well a sample synthetic profile matches with the mean observed one. The sum of square differences χ^2 between the synthetic and observed profiles, the merit function, is defined as

$$\chi^2 = \sum_{\lambda} g_\lambda (I_\lambda^{syn} - I_\lambda^{obs})^2, \tag{3.2}$$

where I_λ^{syn} and I_λ^{obs} are the synthetic and local mean observed profiles' intensities, respectively, and g_λ are weights assigned to individual wavelengths. The merit function is a measure of the fit quality and the best fit corresponds to its minimum. The merit function for a given I_λ^{obs} is constructed in a two-parameter space, corresponding to the grid of pre-computed synthetic profiles and model atmospheres parametrized by p_m and p_T (see Section 2.5.1). Its minimum determines the pair of best-fit parameters $[p_\mathrm{m}, p_\mathrm{T}]_\mathrm{min}$ and thus the best-matching model atmosphere.

3.5 Line-formation heights

Knowledge of the effective formation height of the hydrogen, calcium and magnesium lines in the solar chromosphere is essential for the determination of the range of heights in the chromosphere, where the energy carried by acoustic waves and that released by radiation have to be compared (see Section 7). In Equation 2.7, the specific intensity at each given frequency is a Laplace transform of the source function. If we compute this intensity from the center to the wings of spectral line and also for continua, we can obtain a synthetic spectrum. The formation heights can be obtained from the contribution function $C_\nu(z)$, defined as

$$C_\nu(z) = S_\nu(\tau_\nu)\exp(\tau_\nu/\mu)\chi(\nu)/\mu, \tag{3.3}$$

From Equation 2.7, the emergent intensity is thus

$$I_\nu = \int C_\nu(z)\mathrm{d}z, \tag{3.4}$$

which describes the contribution of different atmospheric layers to the emergent intensity I_ν at the considered frequency ν and the geometrical height in the atmosphere z (e.g., Gurtovenko et al., 1974).

The MALI code (Section 3.4) is also used to compute $C_\nu(z)$ of the Hα, Hβ, Ca II K&H, Ca II 854.2 nm, and Mg II k&h lines in quiet- and active-Sun atmospheric models. The panels of Figures 3.5 and 3.6 show $C_\nu(z)$ of the Hα and Hβ lines in the six initial models VAL A–F. The colors, from light orange to black, are scaled in ten steps of log $C_\nu(z)$ between the minimum and maximum values of the contribution function.

In the line center of Hα, the main contribution arises from chromospheric layers and the photosphere contributes only in the coolest models A and B. The contribution for the the Hβ center is strongly influenced by the photosphere, but

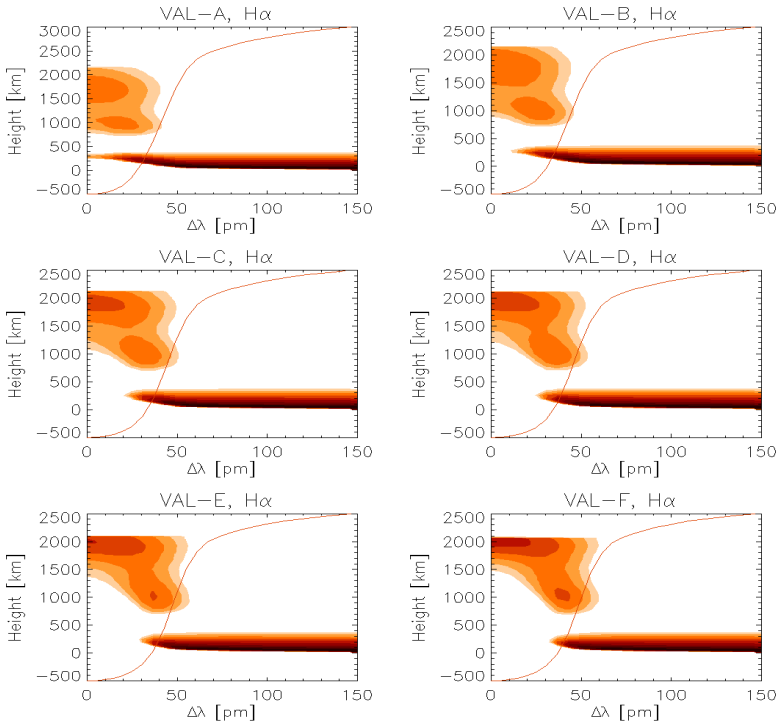

Figure 3.5: Contribution functions of Hα line in the initial models VAL A–F together with corresponding synthetic line profiles (red lines). The colors change from light orange to black in ten steps of log $C_\nu(z)$ between the minimum and maximum.

the photospheric contribution decreases with increasing temperature of the models from A to F. Figures 3.7, 3.8, 3.9 and 3.10 show $C_\nu(z)$ of the Ca II 854.2 nm, Ca II K, Mg II k and Mg II h lines, respectively. We can see that unlike Hβ, the centers of the Ca II and Mg II lines are formed mainly in the chromosphere.

Contribution functions computed from two typical scaled models that characterize the quiet Sun (BBSO data set, see Section 4.3.2) and bright chromospheric features (VTT data sets, see Section 4.1.2) in our observations are plotted for different wavelength distances $\Delta\lambda$ from the line center and different heights in Figure 3.11. We can see that the central parts of line profiles are formed largely in the chromosphere, each of them in different ranges of heights.

We can select an appropriate frequency (or wavelength) in the line profile to sample different depths in the atmosphere. Obviously, centres of the lines under study are formed in the highest chromospheric layers. With increasing frequency difference $\Delta\nu$ from the centre, the formation height generally shifts to lower layers, but in a strongly non-linear and ambiguous way. A careful selection of $\Delta\nu$ (or $\Delta\lambda$) that avoids strong contributions from the photosphere allows us to sample lower chromospheric layers. This approach is used for Doppler velocity measurements at different heights in the chromosphere (Chapter 4).

The effective formation height z_ν^{eff} is calculated as the weighted average of heights with the weights corresponding to $C_\nu(z)$ for a given frequency

$$z_\nu^{\mathrm{eff}} = \int_0^{z_{\max}} C_\nu(z)\, z\, \mathrm{d}z \Big/ \int_0^{z_{\max}} C_\nu(z)\, \mathrm{d}z. \tag{3.5}$$

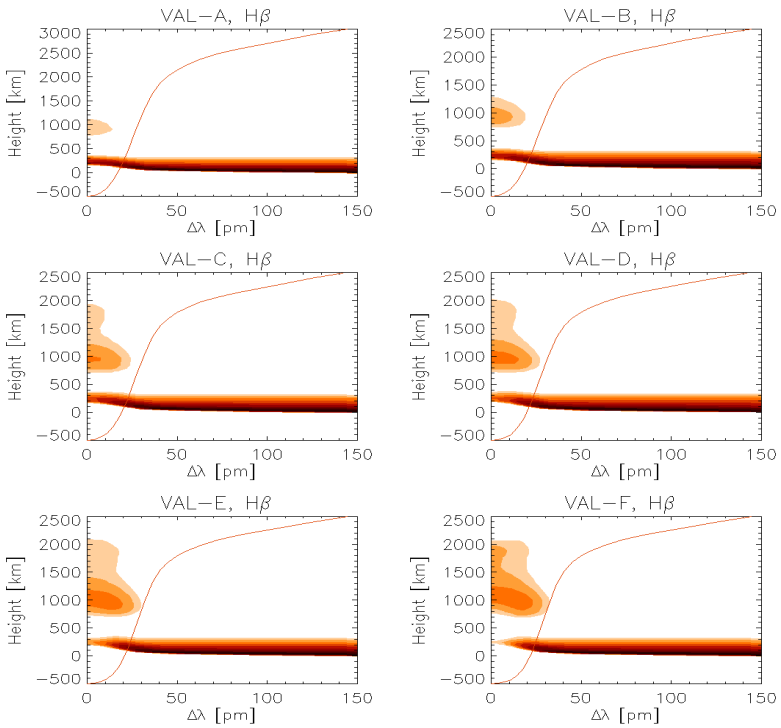

Figure 3.6: Contribution functions of Hβ line in the initial models VAL A–F together with corresponding synthetic line profiles (red lines). The colors change from light orange to black in ten steps of log $C_\nu(z)$ between the minimum and maximum.

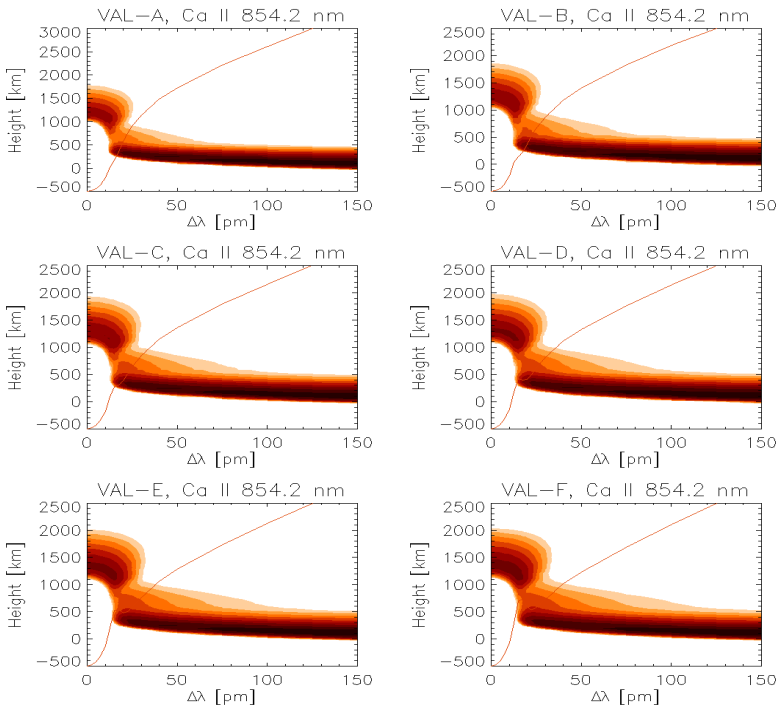

Figure 3.7: Contribution functions of Ca II 854.2 nm line in the initial models VAL A–F together with corresponding synthetic line profiles (red lines). The colors change from light orange to black in ten steps of log $C_\nu(z)$ between the minimum and maximum.

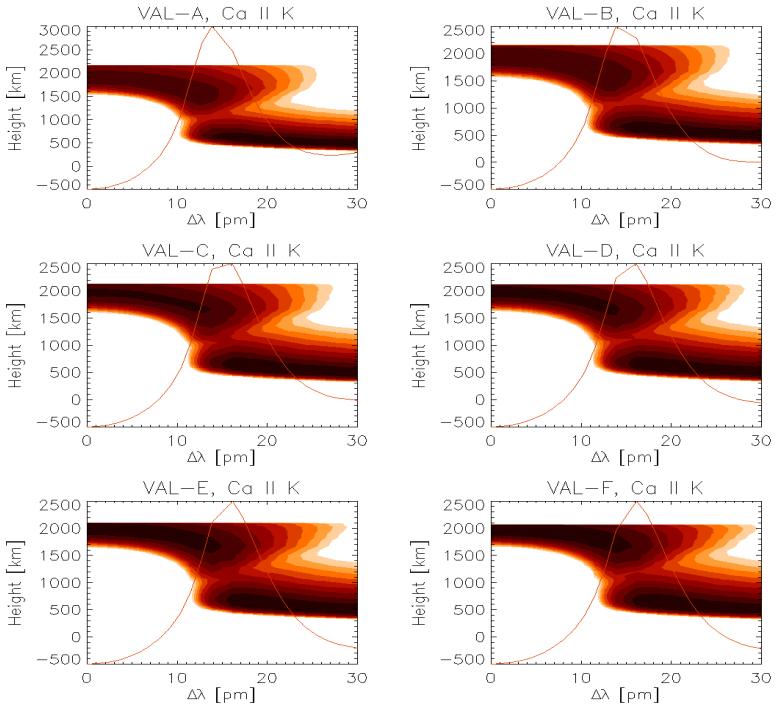

Figure 3.8: Contribution functions of Ca II K 393.4 nm line in the initial models VAL A–F together with corresponding synthetic line profiles (red lines). The colors change from light orange to black in ten steps of log $C_\nu(z)$ between the minimum and maximum.

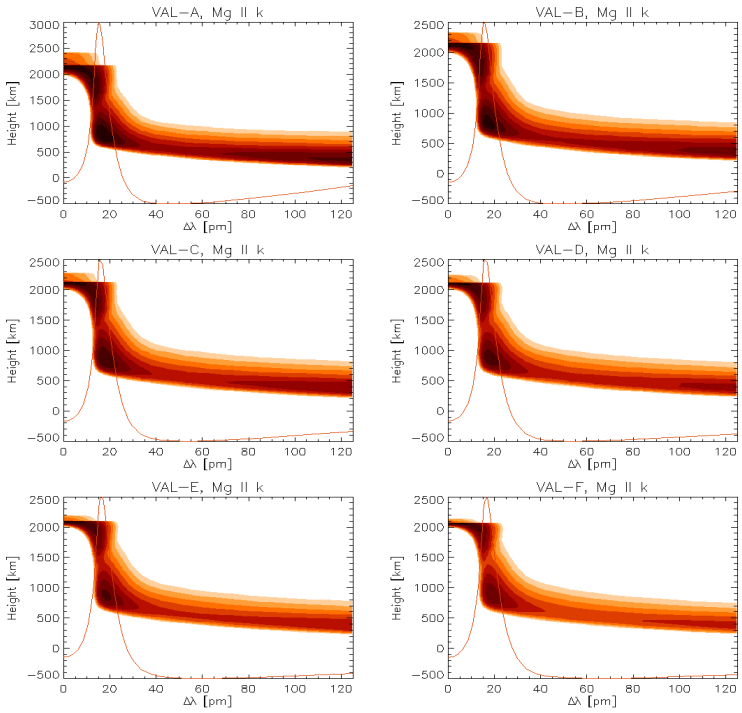

Figure 3.9: Contribution functions of Mg II k 279.55 nm line in the initial models VAL A–F together with corresponding synthetic line profiles (red lines). The colors change from light orange to black in ten steps of log $C_\nu(z)$ between the minimum and maximum.

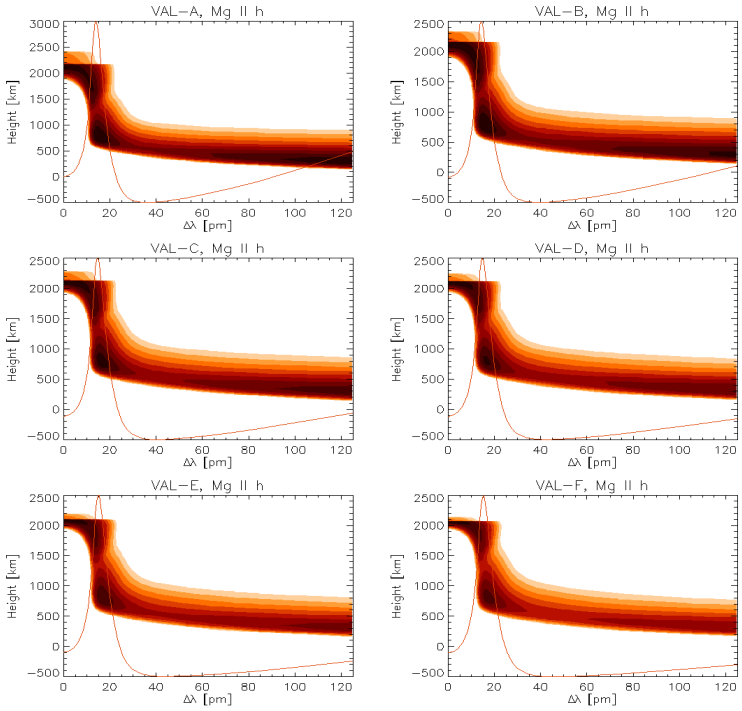

Figure 3.10: Contribution functions of Mg II h 280.27 nm line in the initial models VAL A–F together with corresponding synthetic line profiles (red lines). The colors change from light orange to black in ten steps of log $C_\nu(z)$ between the minimum and maximum.

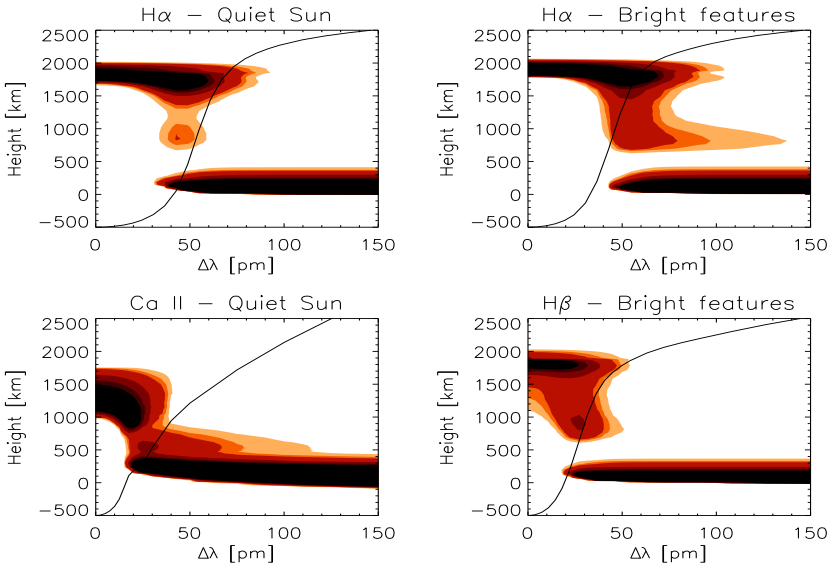

Figure 3.11: Contribution functions of the Hα, Hβ, and Ca II 854.2 nm lines for two typical models derived from our observations – quiet Sun (*left*) and bright chromospheric features (*right*). The colors change from light orange to black with increasing values of the contribution function. Black lines show corresponding synthetic line profiles.

We obtained typical formation heights using all models in each observed data set and found the most frequent ones. The Hα line center is formed typically at 1800 km in the quiet-Sun atmosphere and at 1900 km in bright chromospheric features. For the Ca II 854.2 nm line in the quiet Sun, the typical formation height of the line center is 1400 km and the inner wings at $\Delta\lambda = \pm 13$ pm are formed at 1000 km. From contribution functions computed at this $\Delta\lambda$ for each pixel in the BBSO data set (Section 4.3.2) we find that only 4 % of pixels have a contribution from the photosphere, which is smaller than 1 %. The Hβ line is more problematic. Its inner wings at $\Delta\lambda = \pm 18$ pm are formed typically at 1600 km in bright chromospheric features (Figure 3.11) but 18 % of pixels in the VTT data set (Section 4.1.2) have photospheric contributions larger than 20 % at this wavelength. The selection of $\Delta\lambda$ for Hβ and Ca II was intended to measure Doppler velocities in the deepest possible chromospheric layers with a minimum contribution from the photosphere. The most frequent typical formation heights, stated above, were accepted as the reference heights for the calculation of radiative losses and deposited acoustic fluxes.

The scatter of typical formation heights around the reference height is characterized by standard deviations of 20 km in the middle and upper chromosphere of the quiet-Sun region (BBSO data set, Ca II and Hα) and 100 km in the upper chromosphere of weak active regions with a wide variety of models (VTT data sets, Hα and Hβ). Although the latter value is large, it does not introduce any error into physical quantities and radiative losses computed from the models, because they refer to fixed reference heights. The difficulty arises in Doppler velocities, which are sometimes measured at heights different from the reference ones (see Chapter 4). We analyzed root-mean-squared (rms) Doppler velocities σ_v measured at different $\Delta\lambda$, corresponding to the formation-height uncertainty of ± 100 km, in the Hα and Hβ profiles of the VTT data sets. The relative difference $\Delta\sigma_v/\sigma_v$ was approximately of 7 % in the central parts of profiles formed purely in the chromosphere and increased by a factor of two at $\Delta\lambda$ with photospheric contribution. Because the acoustic energy flux is proportional to σ_v^2, its relative error was estimated to $\Delta\sigma_v^2/\sigma_v^2 \simeq 2\Delta\sigma_v/\sigma_v \simeq 15\,\%$ and 30 %, respectively. For the BBSO data set, the relative error of the acoustic flux is 3 %.

In the IRIS data sets (Section 4.4.2), we found effective formation heights of those parts of the line profile where the Doppler velocities are measured, that is, the central reversal ($z_2, \Delta\lambda = 0$) and the half-maximum intensity of the emission core (z_1). Here, $\Delta\lambda$ varies in the range 0.20–0.23 Å for the k line and 0.18–0.21 Å for the h line, according to the model atmosphere. We obtained effective formation heights z_1 and z_2 for all models assigned along the slit of each IRIS data set. The Mg II k and h lines behave similarly. The emission core of the k line is formed only by a few tens of kilometers higher then the core of the h line, so that we define the effective formation heights z_1 and z_2 as the average of heights obtained for both lines and adopt them for the reference ones.

Figure 3.12 shows these heights in typical quiet- and active-Sun data sets (QS11 and AR10, see Section 4.4.2). We see that the effective formation heights of the central reversal at most of the positions in the quiet Sun, characterized by low-temperature model atmospheres, are between 2000–2200 km, while those of active regions (hot models) are mainly in the range of 1700–1900 km. For the

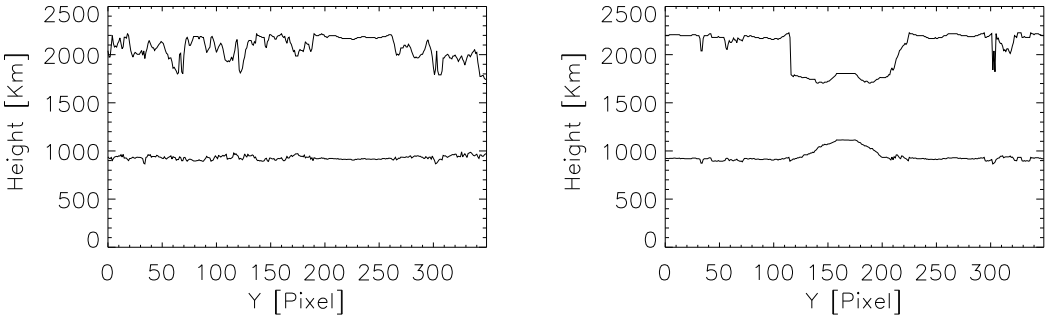

Figure 3.12: Lower and upper effective formation heights of the Mg II lines in the typical quiet-Sun IRIS data set – QS11 (left) and active-region data set – AR10 (right) are plotted versus the position along the spectrograph slit.

emission core, the effective formation heights are in the range 900–1000 km and 1000–1200 km in quiet and active regions, respectively.

Chapter 4

Observations and data analysis

4.1 VTT data sets

The Vacuum Tower Telescope (VTT, Schröter et al., 1985; von der Lühe, 1998) and the GREGOR telescope (Schmidt et al., 2012) are operated by three German institutes: the Astrophysikalisches Institut Potsdam (AIP), the Kiepenheuer Institut für Sonnenphysik (KIS), and the Max-Planck-Institut für Sonnensystemforschung (MPS) at the Spanish Observatorio del Teide on Tenerife, Canary Islands.

VTT is a classical solar telescope with two coelostat mirrors (D=80 cm). The main advantage of the coelostat system is the stationary (non-rotating) solar image in the laboratory. The sunlight transmitted into the telescope falls to the primary and secondary mirrors. The primary mirror is a 70-cm one with a focal length of 46 m. The secondary mirror deflects the light path to the primary focus. To avoid internal seeing, the entire optical path between the mirrors is evacuated. The telescope is situated in a tower 38 m high. In Figures 4.1 and 4.2, the VTT building and the beam geometry are shown, respectively. The VTT adaptive optics (AO) system was developed at KIS in 1998. The main purpose of this system is to improve the image quality in all instruments. Under good seeing it provides a spatial resolution of about $0.2''$ at 500 nm for short exposure times. The VTT instrumentation is designed for high-resolution spectroscopy.

GREGOR is the largest European solar telescope with the aperture of 1.5 m. Currently, its most important post-focus instrument is the GREGOR Infrared Spectrograph (GRIS, Collados et al., 2012), working in the wavelength ranges around 1 and 1.5 μm.

4.1.1 VTT echelle spectrograph

This long-slit echelle grating spectrograph with a predisperser is a powerful tool for diagnostic spectroscopy. Maps of solar regions can be scanned thanks to a dependable interaction between the telescope and the AO tip-tilt system. The spectrograph has a spectral resolution of more than 750 000 and the predisperser allows to observe simultaneously three different wavelength bands. Three exchangeable gratings with different blaze angles are available to optimize the light passing through a system. Data acquisition is performed with up to three PCO 4000 CCD cameras. The image scale in the focal plane of the spectro-

Figure 4.1: Vacuum Tower Telescope with open dome. The image is taken from the neighboring GREGOR telescope. Courtesy KIS web page.

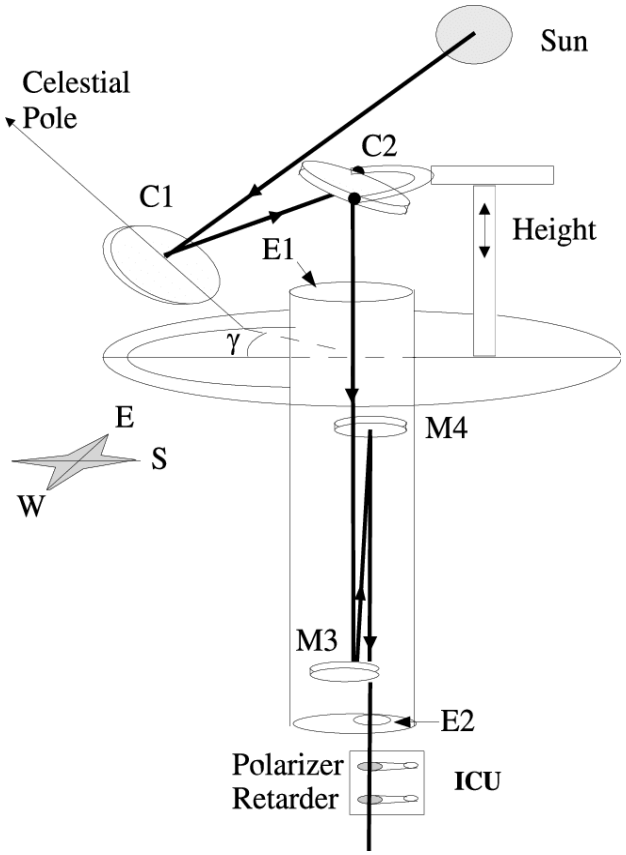

Figure 4.2: Beam geometry of the VTT. The coelostat consists of two flat aluminum-coated mirrors (C1 and C2), which feed the light beam into the telescope. M3 is the imaging mirror (f=46 m). M4 folds the light down to the laboratories. E1 and E2 are the entrance and exit windows of the evacuated tube. Courtesy KIS web page.

graph is 8.98″/mm. Data calibration packages are available to produce level-1 data. The spectra are calibrated for dark and flat-field frames using the software package "sTools" developed in AIP. All routines are written in the Interactive Data Language (IDL) and are documented in the headers. More details about the VTT and echelle spectrograph are given in the VTT's web page (`http://www.leibniz-kis.de/en/observatories/vtt/`).

4.1.2 Observations

The observations were performed in the years 2018 and 2019 using the VTT echelle spectrograph and, in 2018, together with GRIS at GREGOR (Abbasvand et al., 2020b). GRIS was observing the photospheric line Fe I 1564.9 nm in the spectropolarimetric mode to measure vector magnetic field in the target of 2018 December 11. More details about the polarimeter are presented in Collados et al. (2007). The polarimetric calibration was carried out using the calibration unit in the secondary focus of GREGOR (Hofmann et al., 2012).

The first data set was obtained on 2018 December 11 and the second on 2019 June 6. In both cases, quiet regions with the presence of weak chromospheric plages and small pores near the disk center were scanned. Two PCO 4000 CCD cameras were mounted at the echelle spectrograph to acquire spectra in two different spectral regions. The first one was centered at the Hα line at 656.28 nm and the second one at the Hβ line at 486.13 nm. The seeing conditions were very good and stable during the observing campaigns, with a granular rms-contrast of 5–6 % in a continuum window centered at a wavelength of 500 nm. The relevant characteristics of both data sets are summarized in Table 4.1.

VTT Observations		
	2018 December 11	2019 June 6
Time	11:42 UT	10:15 UT
Target	Weak AR - pore	Weak AR - plage
Scanned lines	Hα 656.28 nm (I) Hβ 486.13 nm (I)	Hα 656.28 nm (I) Hβ 486.13 nm (I)
Coordinate	-423″E, 147″N	416″E, 122″N
Cosine of heliocentric angle	0.88	0.89
No. of sp. points	2004 (Hα); 1560 (Hβ)	334 (Hα); 334 (Hβ)
Wavelength spacing	0.41 pm (Hα); 0.3 pm (Hβ)	1.66 pm (Hα); 1.21 pm (Hβ)
Wavelength range	138 pm (Hα); 100.8 pm (Hβ)	555.3 pm (Hα); 403.3 pm (Hβ)
Field of view	14.4″ × 222.66″	50.4″ × 180″
Region of interest	14.4″ × 45.54″	50.4″ × 126″
Pixel size	0.36″ × 0.18″	0.36″ × 0.36″
Exposure time	300 ms	80 ms
Raster scan time	25 s	25 s
No. of sp. scans	60	305

Table 4.1: Parameters of the VTT data sets

Mean profiles of the Hα and Hβ spectral lines were obtained by time-averaging over the observing period of each series of the observed profiles with removed Doppler shifts. They are used to find the most appropriate semi-empirical models (Sections 2.5.1 and 3.4) at each location in the regions of interests (ROIs) . In both observations, we concentrated on ROI that included a plage, a tiny pore, and a quiet-Sun area. The locations of the ROIs in the Hα context images obtained by the Global Oscillation Network Group (GONG, Harvey et al., 1996) at the Observatorio del Teide site are shown in Figure 4.3. Note that the ROI on June 6 was close to a filament.

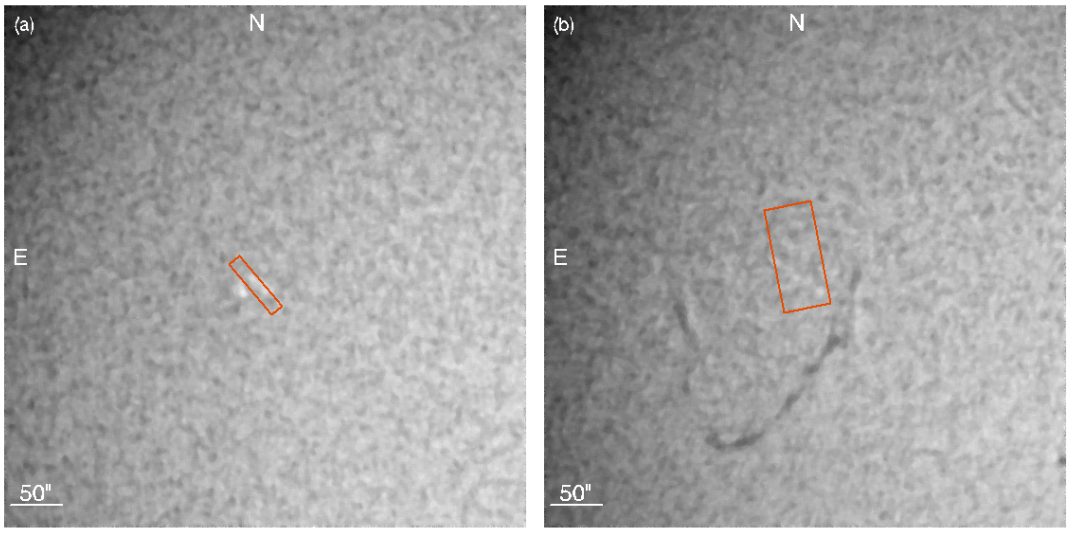

Figure 4.3: Context Hα images (GONG) with regions of interest outlined by red rectangles. (a) 2018 December 11, 11:42 UT; (b) 2019 June 6, 11:00 UT.

4.1.3 Data processing

- **Doppler velocity**
  The Doppler velocities were measured for two purposes: (1) to remove Doppler shifts from the spectroscopic observations to calculate time-averaged line profiles and (2) to obtain purely chromospheric Doppler velocities required for the calculation of acoustic fluxes. In the first case, we measured the Doppler velocities in the inner wings using the bisector positions of the Hα and Hβ cores at five intensity levels from 40 % to 70 %, where 0 % corresponds to the line-core intensity and 80 % to the line-wing intensity near the continuum. We used the `bisec_abs_lin.pro` routine included in the KIS IDL library. Figures 4.4 and 4.5 show the bisector positions for both lines in the June data set. The five bisector positions were averaged and converted into the Doppler velocities assuming that the quiet-Sun regions within the field of view are at rest on average.
  In the second case, to estimate the deposited acoustic flux, we measured the Doppler velocities in the line center of Hα, using a parabolic fit around the minimum intensity (orange parts in Figure 4.4 and 4.5). The Hβ velocities were obtained from an average shift of five bisector points, [0.36, 0.38, 0.40,

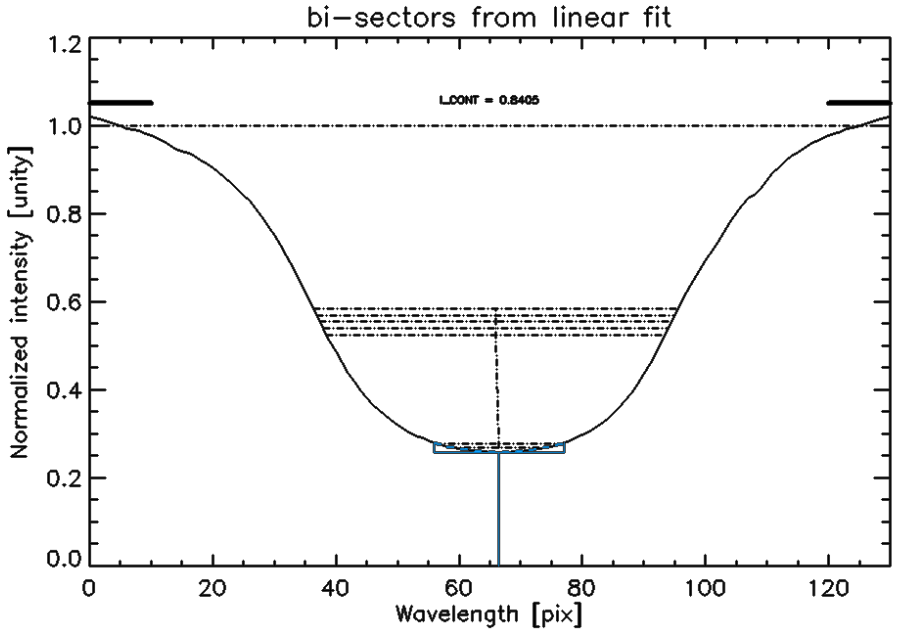

Figure 4.4: A plot made by `bisec_abs_lin.pro` showing bisector positions for Hα. Blue part represents a parabolic fit around the minimum intensity.

0.42, 0.44], close to $\triangle\lambda = \pm 18$ pm from the line center (see Section 3.5 for the $\triangle\lambda$ determination). Figure 4.6 shows the Doppler velocities of both lines for data sets.

- **Magnetic field**
  The magnetic-field strength and inclination are necessary for the acoustic-flux calculation. For the December 11 data set, the full-Stokes profiles of the Fe I 1564.8 nm line obtained with GRIS at 09:34 UT were inverted to derive the magnetic field vector in the photosphere. The observations had 400 scan steps of 0.135″ and 424 pixels, 0.136″ each, along the slit. The whole map was completed in 25 min. The data were reduced with the standard GRIS-procedures (for a basic description see Collados, 1999). For the inversion, we used the Stokes Inversion based on Response functions code (SIR) by Ruiz Cobo and del Toro Iniesta (1992). We restricted ourselves to a one-component model atmosphere and assumed that the magnetic field and the Doppler velocities were constant over the height range where the Fe I line was formed. Besides the field strength, the SIR code provides also the inclination and azimuth of the magnetic field along the line-of-sight (LOS). We solved the 180° ambiguity using the code AMBIG (Leka et al., 2009) and transformed the magnetic field inclination and azimuth to the local reference frame (LRF) using routines from the AZAM code (Lites et al., 1995).
  The magnetic-field map for the June 6 and also December 11 data sets (for the December data set, there are two different sources of magnetic information) are data products from the Helioseismic and Magnetic Imager (HMI, Schou et al., 2012) onboard the Solar Dynamics Observatory (SDO, Pesnell et al., 2012). The HMI Vector Magnetic Field Pipeline (Hoeksema et al., 2014) obtains the magnetic-field vector from Stokes parameters. The

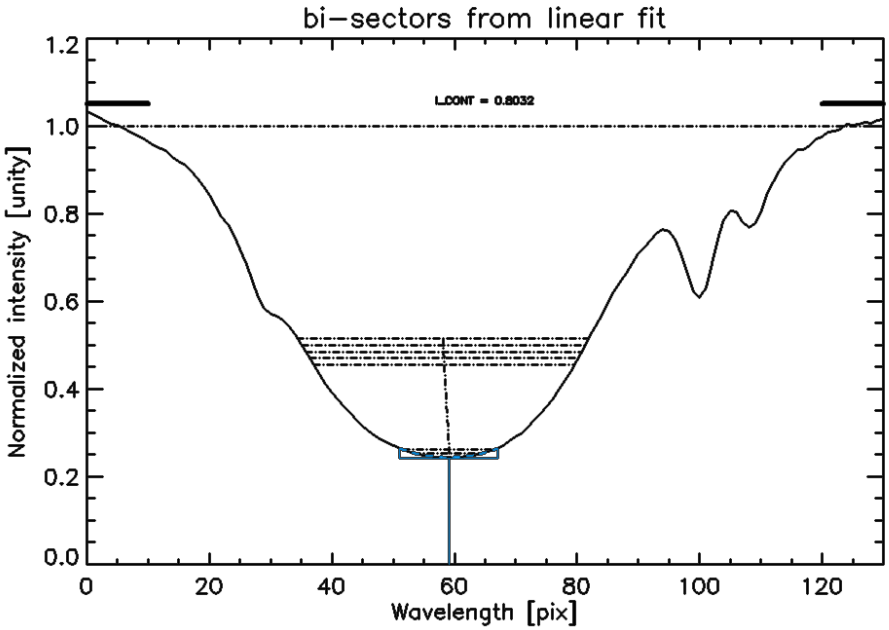

Figure 4.5: Bisector positions for Hβ. Blue part represents a parabolic fit around the minimum intensity (not used).

Stokes parameters are measured at six wavelength positions across the Fe I 617.3 nm line for the full solar disc and are inverted using the Very Fast Inversion of the Stokes Vector code (VFISV, Borrero et al., 2011; Centeno et al., 2014). VFISV solves the radiative-transfer equation considering the Milne-Eddington atmosphere. The azimuth is disambiguated according to the existence of a strong field. In regions with strong magnetic field and their surroundings, the azimuth that makes the magnetic field closer to radial is selected. In regions with weak magnetic field, the azimuth that makes the magnetic field vector more similar to the potential field vector is selected. The inverted vector magnetic field angular parameters, i.e., azimuth and inclination, are referred to the LOS frame and they are converted to the LRF using the AZAM code. The used data sets were observed on December 11 at 12:00 UT, June 6 at 11:24 UT and the full-disc maps of continuum intensity, magnetic-field strength, and inclination were cropped to match the ROIs.
The Stokes Q and U signals were noisy in regions with weak magnetic field strength ($B < 100$ G for the December 11 scan and $B < 125$ G for the June 6 scan) and the inversion codes returned unreliable LOS inclinations θ near 90°. To remove these unreliable values, we applied a mask that set θ to zero in the regions where B was weak and θ was between 85° and 90°. Figure 4.7 shows the maps of photospheric magnetic field strength and LRF inclination for both data sets. Both maps are displayed from HMI data products. In Figure 4.8, the same ROI is shown in the GRIS windows. The spatial resolution of the GRIS magnetic-inclination map was by a factor of two better than that of HMI.

- **Spatial alignment**
  To align the spectroscopic observations with magnetic-field maps, we need

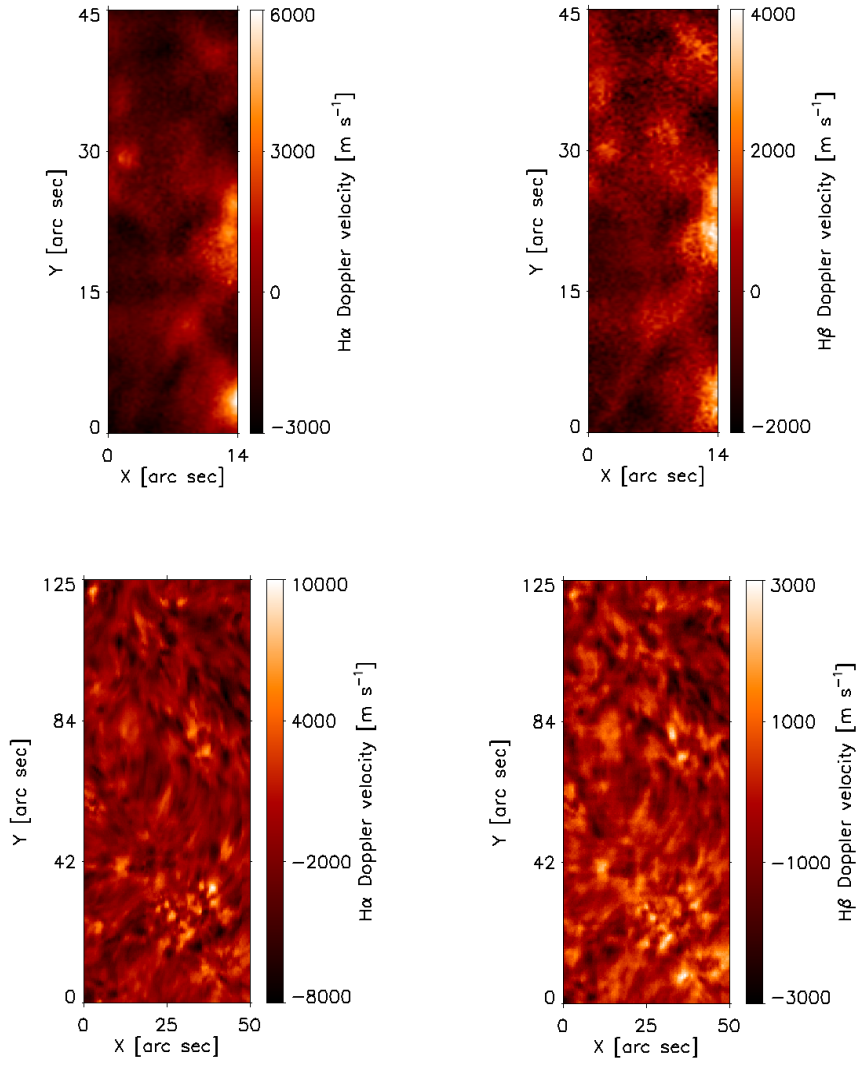

Figure 4.6: Maps of instantaneous Doppler velocities in the line center of Hα and close to $\triangle\lambda = \pm 18\,\mathrm{pm}$ from the line center of Hβ for December 11 at 11:57 UT (top) and June 6 at 11:24 UT (bottom).

to compare the pores and granulation observed in the VTT continuum (reference images) to those seen in the SDO/HMI and GRIS continuum images (transformed images). These features can be identified in both types of continuum images. The transformed and the reference images are inputs for the following semi-automatic spatial alignment procedure.

First, a pair of co-temporal images is inspected visually by the routine `setpts.pro` (or `setpts_roi.pro`) implemented within the IDL SolarSoft System (SSW, Freeland and Handy, 1998). The routine serves for an interactive definition of common points in two images. Then the set of reference points is used to calculate a linear transform, which maps one image onto another, by the SSW function `caltrans.pro`. Finally, the initial transform parameters are entered into the SSW function `auto_align_images.pro` by T. Metcalf, which looks for the best spatial alignment of an image pair through their cross-correlation. Five cross-alignment parameters (i.e., $[x, y]$

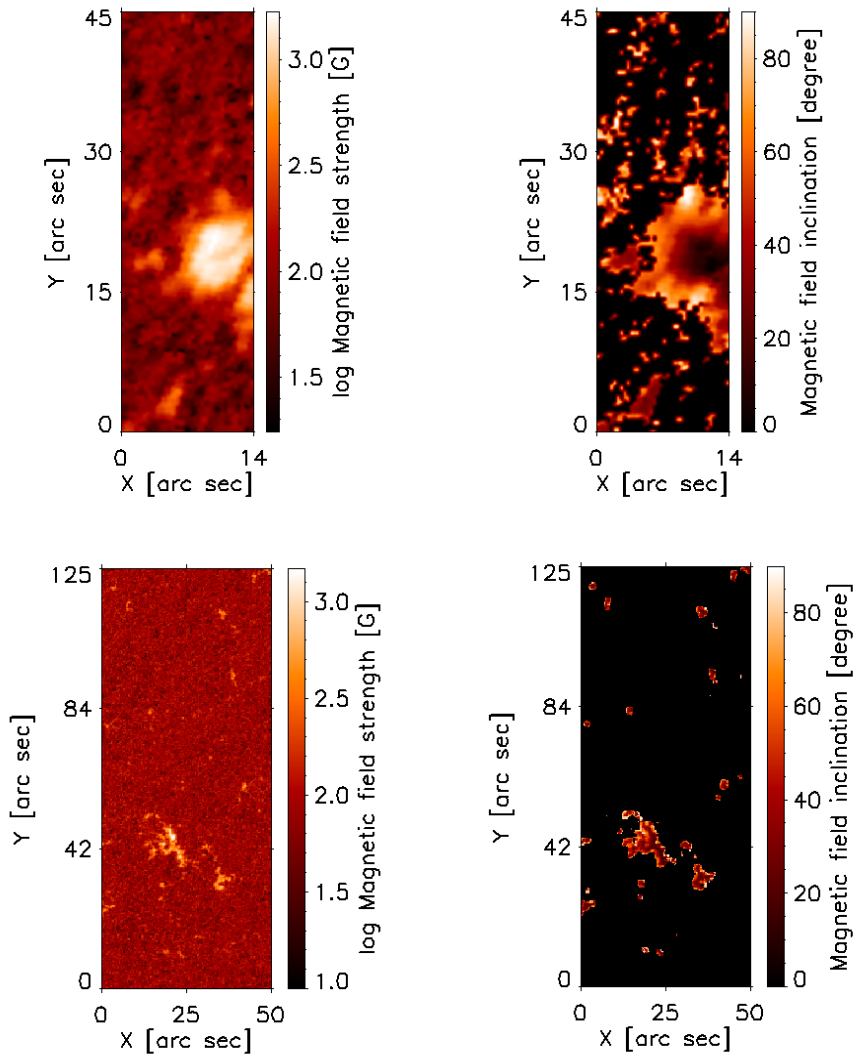

Figure 4.7: Maps of photospheric magnetic-field strength and inclination in the ROIs for December 11 (top) and June 6 (bottom). Both maps are derived from HMI data.

shifts, $[x, y]$ zoom factors, and rotation angle), which yield the maximum cross-correlation, are inferred in two subsequent calls of the function. In the first call, the downhill simplex method (Press et al., 1992), implemented as the `amoeba.pro` routine, is applied. Its results are used as initial parameters for the second call, using the more robust Powell method (Press et al., 1992). By this two-step procedure a satisfactory spatial alignment between the co-temporal image pairs VTT – SDO/HMI and VTT – GRIS (December) and VTT – SDO/HMI (June) are achieved with the cross-correlation coefficients of 0.85, 0.92 and 0.87, respectively.

4.2 IBIS data set

The Interferometric BIdimensional Spectropolarimeter (IBIS, Cavallini, 2006) was, until 2019, attached to the Dunn Solar Telescope (DST), which is a vertical-

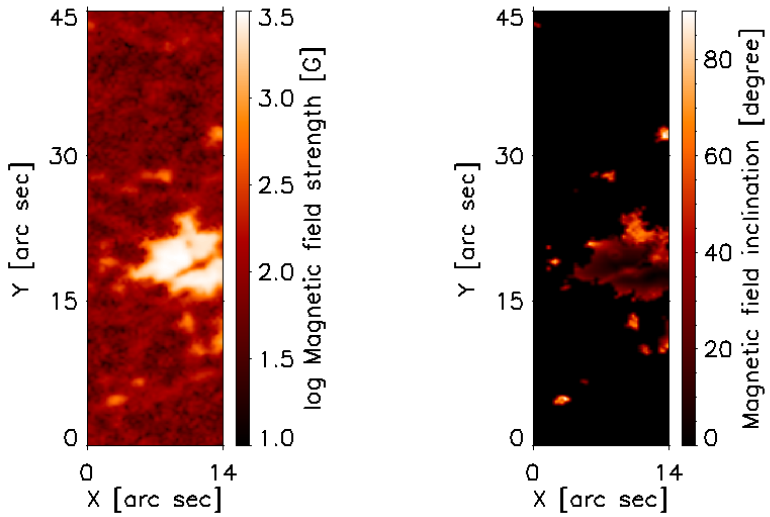

Figure 4.8: Maps of photospheric magnetic-field strength and inclination in the ROI for December 11, derived from GRIS data.

axis solar telescope located at Sacramento Peak, New Mexico. The DST was designed for high-resolution imaging and spectroscopy and its adaptive optics was upgraded in 2004 to compensate the Earth's atmosphere blurring. In 1969, the DST was introduced as the world's premier high spatial resolution optical solar telescope. The optical path begins at a two-mirror turret on top of the tower and travels 59 m underground to reach the primary mirror. Then it goes to optical windows that are located in the optical laboratory. The optical path is evacuated to eliminate image distortion due to convection in the telescope and the heat produced by focusing the solar light. A large horizontal rotating observing platform is used to correct image rotation.

4.2.1 Spectropolarimeter IBIS

The Interferometric bidimensional spectropolarimeter is a dual interferometer and spectropolarimeter. It scans the Sun in spectral lines between 550–860 nm range and creates time series of high-quality imaging, spectroscopy, and polarimetry. It has a large circular field of view combined with a spectral resolving power of R = 200000 and spatial resolution of approximately 0.2″. IBIS is a classically mounted dual Fabry-Pérot instrument constructed by the Arcetri Observatory in Florence, Italy. In spectroscopic mode, it has a circular field of view of 95″ diameter with a spatial sampling of 0.098″. In spectro-polarimetric mode, the field of view is split into two smaller rectangles through a mask, where each one covers about half of the unblocked field. IBIS has an additional parallel broad-band channel with the same image scale as the narrow-band channel that serves as light intensity and image distortion reference. The instrument was dismantled from DST in 2019. More details about the DST and IBIS are given in the DST's web page (`https://sunspot.solar/`).

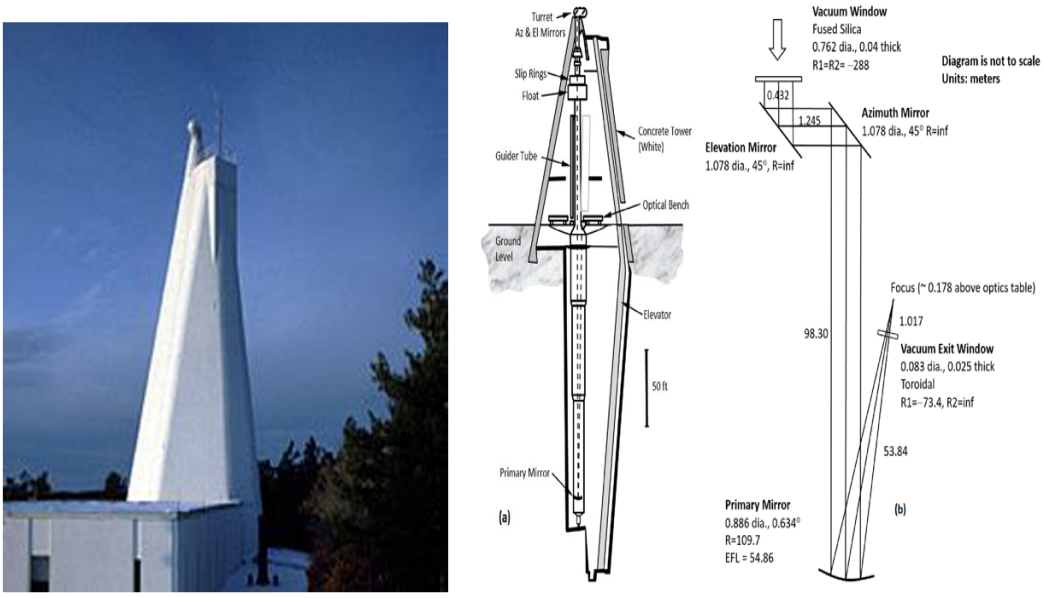

Figure 4.9: Dunn Solar Telescope, its building, and optical scheme (image from Underwood et al., 2017).

4.2.2 Observations

A large isolated solar pore in the active region NOAA 11005 was observed on 2008, October 15 from 16:34 to 17:44 UT with IBIS, using the DST adaptive optics system (Rimmele et al., 2004). The bipolar active region NOAA 11005 lived from October 11 to 16, 2008. The pore was in the leading part of the region with location at 25.2 N and 10.0 W (heliocentric angle $\theta = 23°$, $\mu = \cos\theta = 0.92$) and decayed slowly. A superpenumbra surrounded the pore (Sobotka et al., 2013). The region of interest (ROI) included a weak chromospheric plage located in the eastern part of the field of view (FOV), with the same magnetic polarity as the pore (Figure 4.10).

The data set (cf. Sobotka et al., 2013) has 80 scans and each scan contains a full Stokes (I,Q,U,V) 21-point scan of the Fe I 617.33 nm line with wavelength spacing 2 pm and a 21-point I-scan of the infrared Ca II 854.2 nm line with wavelength spacing 6 pm. At each wavelength in the Fe I line, six modulation states I $\pm$ [Q,U,V] were acquired. Each sequence therefore consists of 21 $\times$ 6 (Fe I) + 21 (Ca II) = 147 narrowband images. The exposure time was 80 ms for a single image and the time resolution was 52 s for one sequence. From this, the I-profile of the Ca II line was scanned in 6.4 s. The size and pixel scale of the narrowband images are 512 $\times$ 512 pixel and 0.167″, respectively. As a consequence of the IBIS polarimetric setup, the FOV was reduced to 228 $\times$ 428 pixels, that is, 38″ $\times$ 71.5″. Synchronously with the narrowband images, broadband (WL) frames at $\lambda = 621.3 \pm 5$ nm were acquired with an equal exposure time of 80 ms. The relevant characteristics of this data set are summarized in Table 4.2.

The narrowband images were corrected for motion and distortion, using as a reference a series of WL frames reconstructed by the multi-frame blind deconvolution method (MFBD, van Noort et al., 2006). Then, the standard reduction pipeline (Viticchié et al., 2010) was applied to the narrowband data to correct for

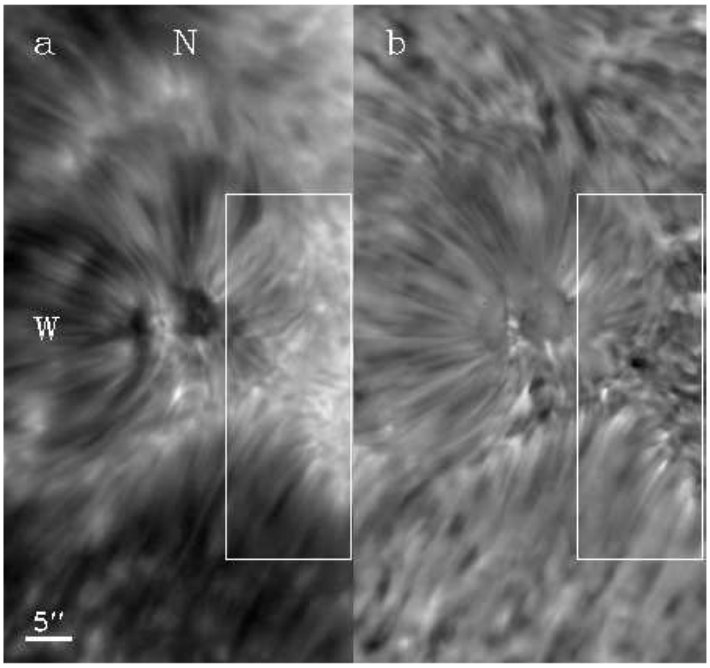

Figure 4.10: A snapshot at 17:10 UT of the full FOV (38″ × 71.5″) with the pore NOAA 11005. (a) Ca II 854.2 nm line center intensity, (b) Doppler map at $h \sim 1000$ km. The velocities range from -4.5 km s^{-1} (black, toward the observer) to 5.9 km s^{-1} (white, away from the observer). The ROI is outlined by a white rectangle. Courtesy Sobotka et al. (2016).

the instrumental blue shift (Cavallini, 2006) and the instrument- and telescope-induced polarizations.

IBIS Observation	
Date	2008 October 15
Time	16:34–17:44 UT
Scanned lines	Fe I 617.33 nm (I, Q, U, V)
	Ca II 854.2 nm (I)
Coordinate	10″W, 25.2″N
Cosine of Heliocentric angle	0.92
No. of spectral points	21 in each line
wavelength spacing	2 pm (Fe I); 6 pm (Ca II)
Field of view	38″×71.5″
Region of interest	13.7″×39.7″
Pixel size	0.167″×0.167″
Spatial resolution	0.4″
Exposure time	80 ms
Raster scan time	52 s
No. of spectral scans	80

Table 4.2: Parameters of the IBIS data set

4.2.3 Data processing

- **Doppler velocity**
  Chromospheric Doppler velocities were measured in the Ca II 854.2 nm line. According to Cauzzi et al. (2008), the wings 50–70 pm far from the line center come from the middle photosphere 200–300 km above the unity optical depth in the 500 nm continuum, while the line core is formed in the middle chromosphere between 900 and 1500 km. The Ca II 854.2 nm core shows significant Doppler shifts caused by chromospheric oscillations. Line-of-sight (LOS) velocity maps were measured (1) in the inner wings of the core at $\Delta\lambda = \pm 18$ pm that are formed approximately at 1000 km, using the "double-slit" method (Garcia et al., 2010). This method consists in the minimization of difference between intensities of light passing through two "slit" located at a certain distance in the opposite wings of the emission core. The line profile is shifted by sub-pixel distances with respect to the "slits" to find the minimum intensity difference. The distance between the "slits" determines the depth of the profile, for which the shift is measured. The velocities were also measured (2) in the line center formed at about 1400–1500 km, using a parabolic fit to five wavelength points. The reference zero of the Doppler velocity was defined as a time and space average of all measurements. Measurements (1) and (2) gave practically identical results, with slightly (by 4 %) higher amplitudes detected by (2).
  Mean profiles of the Ca II 854.2 nm line were obtained by time-averaging over the observing period of each series of the observed profiles with removed Doppler shifts. They are used to find the most appropriate semi-empirical models at each location in the ROI (Sections 3.4 and 2.5.1).

- **Magnetic field**
  The magnetic field configuration in the photosphere, necessary for the calculation of the acoustic energy flux in Chapter 6, was retrieved using the Stokes inversion code based on response functions (SIR, Ruiz Cobo and del Toro Iniesta, 1992), applied to the Fe I 617.33 nm Stokes profiles. Two nodes were set for the temperature and one node for all the other parameters such as the magnetic-field vector and the LOS velocity. The microturbulent velocity was fixed at 1.3 km s^{-1}, the macroturbulence at zero, the spatial stray-light contamination was set to 15 %, and the IBIS spectral instrumental profile was included in the inversion. The retrieved magnetic field inclination and azimuth were transformed to the local reference frame using the routines of the AZAM code (Lites et al., 1995) and the azimuth ambiguity was resolved using the method by Georgoulis (2005). We selected a scan at 17:10 UT in the middle of the observation to represent the magnetic field configuration. Since the Stokes Q and U signals were noisy in regions with weak magnetic field strength (B < 300 G), resulting in false values of the inclination $\theta \approx 90°$ (horizontal direction), a mask was applied to set $\theta > 85°$ to zero in such regions. For B > 300 G all the inclination values were allowed. The region of interest that covered the plage to the East of the pore together with some quiet Sun area was set to 82 × 238 pixels, that is, 13.7″ × 39.7″ (Figure 4.10). The maps of photospheric magnetic field

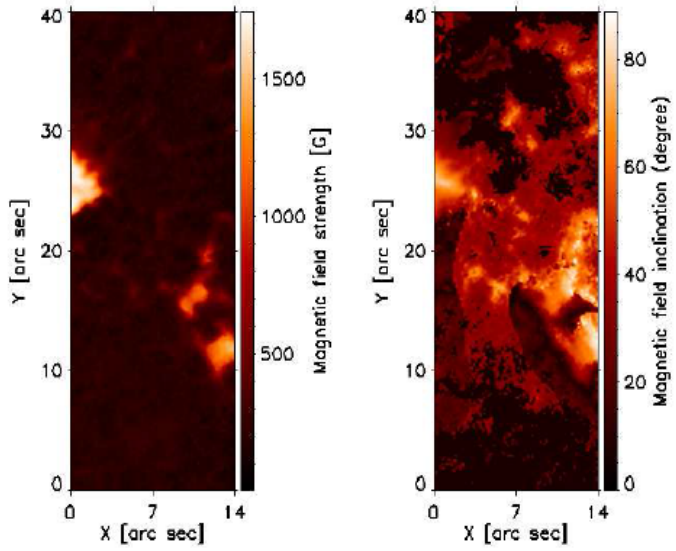

Figure 4.11: Maps of photospheric magnetic field strength and inclination in the IBIS ROI.

strength and inclination retrieved from the inversion of the Fe I 617.33 nm Stokes profiles are shown in Figure 4.11.

4.3 BBSO data set

The Big Bear Solar Observatory (BBSO) is located on the north side of Big Bear Lake in California at an altitude of 2067 m with excellent seeing conditions. Its main instrument is the 1.6-m Goode Solar Telescope. The Goode Solar Telescope (GST, Goode et al., 2003) is an reflecting, off-axis Gregorian system consisting of a parabolic primary mirror, heat reflector, elliptical secondary mirror and diagonal flat mirrors. It is equipped with an adaptive optics system. Figure 4.12 shows a cutaway sketch of the GST with respect to the locations of six equipped scientific instruments. A 100″ circular opening on the heat stop defines an 70″ × 70″ square FOV on the focal planes. Solar light is imaged by primary and secondary mirrors and then folded through the declination axis. Post-focus instruments are mounted at the end of this axis in the optical laboratory. The Fast Imaging Solar Spectrograph (FISS) is also mounted on the horizontal bench in this lab.

4.3.1 GST instruments

The Fast Imaging Solar Spectrograph (FISS, Chae et al., 2013) is a result of collaboration between BBSO and Korean solar community. It is designed to study fine structures in the solar chromosphere. The spectrograph is made up of a field scanner, a slit, an off-axis parabolic mirror, an echelle grating, pre-filters, and two CCD cameras. The single parabolic mirror is used as both collimator and imager, which can be considered as quasi-Littrow configuration. Dispersed beams are collected by two CCD cameras that are preceded by order-

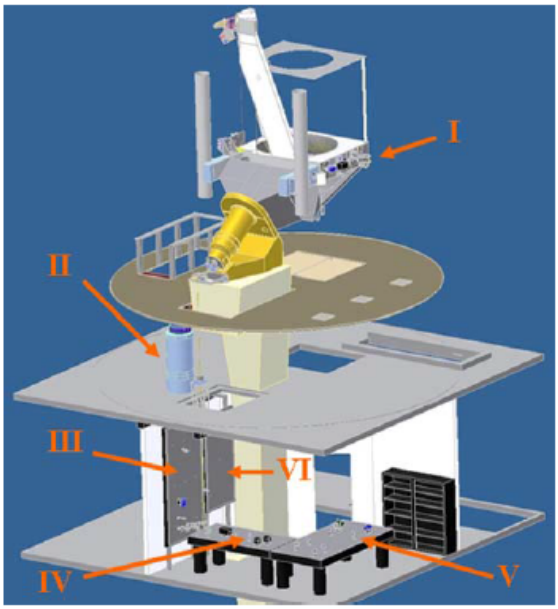

Figure 4.12: Sketch of the New Solar Telescope showing six scientific instruments: I. Nasmyth Focus Filtergraph; II. Cryogenic Infrared Spectrograph (CYRA); III. Adaptive Optics (AO); IV. Near Infra-Red Imaging Spectropolarimeter (NIRIS); V. Visible Imaging Magnetograph (VIM); VI. Fast Imaging Solar Spectrograph (FISS). Courtesy Cao et al. (2010).

selecting narrowband filters, so that images of two spectral bands can be acquired simultaneously. According to the orientation of the grating, various kinds of dual-band combination can be obtained. The spectral resolution is about 4 pm for Hα and 5 pm for Ca II 854 nm. The wavelength range is from 400 to 1000 nm. The two-mirror field scanner is capable of providing fast scanning mode (8 s for a 60″ scan) for the simultaneous observations in Hα and Ca II 854 nm.

The Near Infra-Red Imaging Spectropolarimeter (NIRIS Cao et al., 2010) takes advantage of dual Fabry-Pérot etalons that provide field of view of about 85″. The dual-beam optical design provides two simultaneous polarization maps onto a 2024 × 2048 HgCdTe closed-cycle He-cooled IR array. The spectral lines for NIRIS are the Fe I 1565 nm doublet which are the most Zeeman sensitive lines for the diagnostics of the magnetic field in the lowest layers of the photosphere, while the He I 1083 nm multiplet is the best diagnostics of upper chromospheric magnetic fields. More details about the GST, FISS and NIRIS are given in `http://www.bbso.njit.edu/`.

4.3.2 Observations

The data set was obtained with FISS at GST in a service mode (Abbasvand et al., 2020b). Simultaneous observations of the spectral lines Ca II 854.2 nm and Hα make it possible to measure the deposited acoustic flux in the middle as well as in the upper chromosphere. The target was a quiet-Sun area located exactly at the center of the solar disc, to minimize possible projection effects (Ghosh et al., 2019). Some small magnetic elements were dispersed in this area. The advantage of FISS is its high spectral and spatial resolution combined with

GST/FISS Observation	
Data set	2019 October 3
Time	17:46 UT
Target	Quiet Sun
Scanned lines	Hα 656.28 nm
	Ca II 854.2 nm
Coordinates	0″E, 0″N
Cosine of heliocentric angle	$\mu = 1.00$
No. of spectral points	512 (Hα)
	502 (Ca II 854.2 nm)
Wavelength spacing	1.9 pm (Hα)
	2.6 pm (Ca II 854.2 nm)
Wavelength range	972.8 pm (Hα)
	1305.2 pm (Ca II 854.2 nm)
Field of view	20″ × 41″
Region of interest	13.12″ × 38.4″
Pixel size	0.16″ × 0.16″
Exposure time	60 ms
Raster scan time	22.9 s
No. of spectral scans	210

Table 4.3: Parameters of the BBSO data set.

short exposure times that facilitate fast scanning of the observed area on the Sun. The seeing was good and stable during the 80-minute period of observation that was selected for further analysis. With the aid of the adaptive optics system installed at GST, high-order correction of atmospheric seeing was provided within an isoplanatic patch, with a gradual roll off of the correction at larger distances (Shumko et al., 2014). The raw data were calibrated using standard dark- and flat-field procedures and the FISS data were compensated for image rotation in the coudé focal plane of the telescope. The relevant characteristics of the data set are summarized in Table 4.3. Additional observations were taken with NIRIS to obtain information about the magnetic field. Due to some calibration issues, it was not possible to invert and use these spectropolarimetric data.

4.3.3 Data processing

- **Doppler velocity**
  Like in Section 4.1.3, Doppler velocities were measured (1) to remove Doppler shifts from the spectroscopic observations to calculate time-averaged line profiles and (2) to obtain purely chromospheric Doppler velocities required for the calculation of acoustic fluxes. We used the `bisec_abs_lin.pro` routine from the KIS IDL library. This routine returns line shifts at pre-selected intensity levels in the line profile (a bisector method) and the shift of the line centre, derived from a parabolic fit around the minimum intensity. The shifts were converted into the Doppler velocities assuming that the quiet-Sun regions within the field of view are at rest on average.
  To remove Doppler shifts, we averaged bisector positions at five intensity

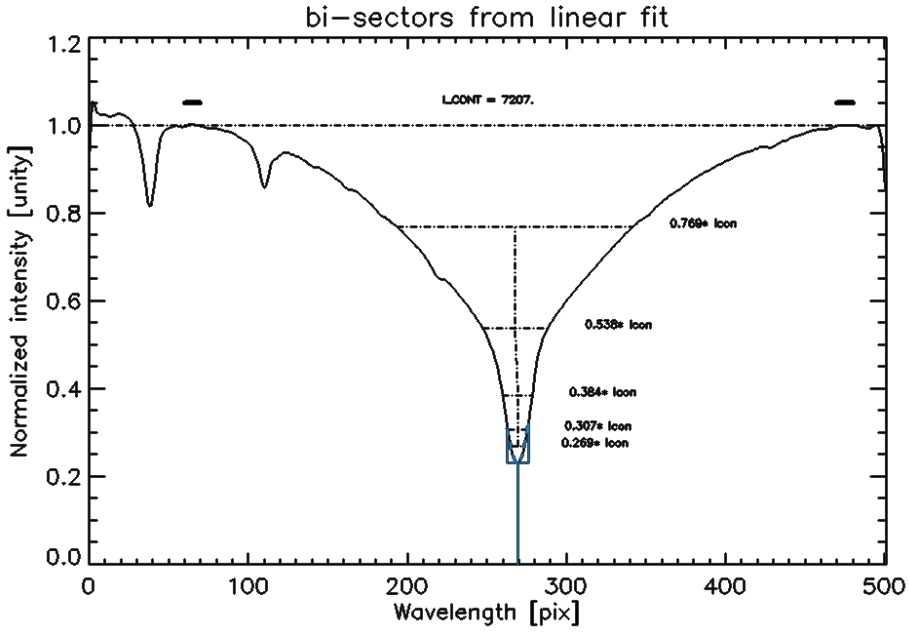

Figure 4.13: A plot made by `bisec_abs_lin.pro` showing bisector positions for Ca II 854.2 nm. Blue part represents a parabolic fit around the minimum intensity.

levels from 40 % to 70 %, where 0 % corresponds to the line-center intensity and 80 % to the line-wing intensity near the continuum. The whole line profile was then moved back by the obtained average shift. To obtain the chromospheric velocities, we used the line-center shifts of Hα and Ca II 854.2 nm lines (parabolic fit) and bisector shifts of Ca II at line-profile intensity level corresponding to the wavelength distance $\Delta\lambda = \pm 13$ pm from the line center that was found from contribution functions (see Section 3.5).
Figures 4.13 and 4.14 display the bisector intensity levels for Ca II and Hα at [0.05, 0.1, 0.2, 0.4, 0.7] and [0.02, 0.05, 0.17, 0.37, 0.6], where the corresponding wavelength distances from the line centers are [10, 15, 23, 52, 189] pm and [21, 32, 54, 71, 98] pm, respectively. Figure 4.15 shows the Doppler velocities in the ROI at 18:24 UT. The rms Doppler velocities σ_v in the line centers of Ca II and Hα were calculated by averaging over the ROI and their mean values are 1.65 and 2.30 km s^{-1}, respectively.
Mean profiles of the two spectral lines were obtained by time-averaging over the observing period of the observed profiles with removed Doppler shifts. They are used to find the most appropriate semi-empirical models at each location in ROIs (Sections 3.4 and 2.5.1).

- **Magnetic field**
  The photospheric magnetic-field strength and inclination are necessary for the acoustic-flux calculation. We expected to obtain this information from NIRIS, however, due to some calibration issues, the inversion of the spectropolarimetric data failed. Therefore we retrieved the magnetic information from another source, HMI (refer to Section 4.1.3). The spatial resolution of HMI magnetic-field vector maps is 1″.
  The HMI data sets were obtained on October 3 at 18:12 UT and the full-

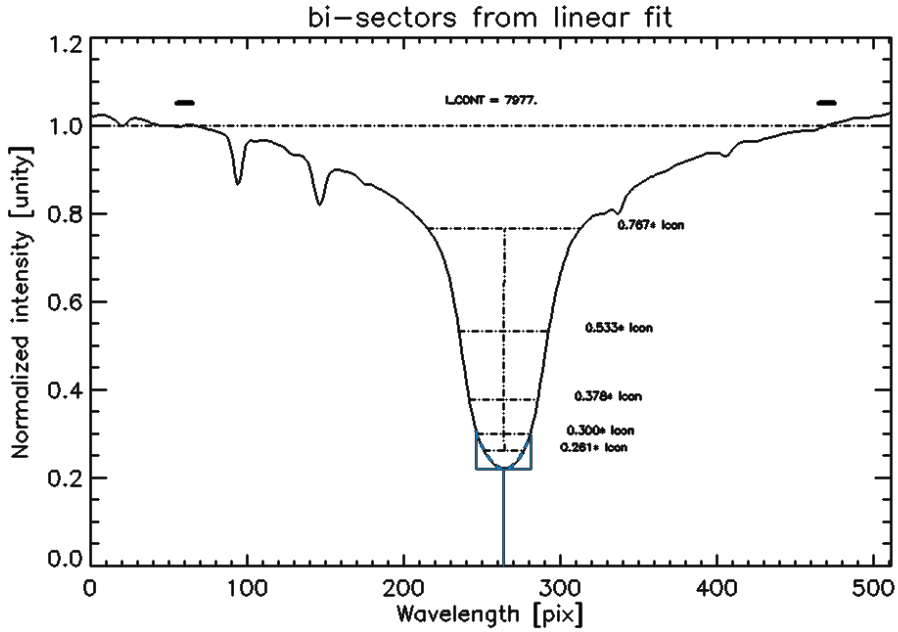

Figure 4.14: A plot made by `bisec_abs_lin.pro` showing bisector positions for Hα. Blue part represents a parabolic fit around the minimum intensity.

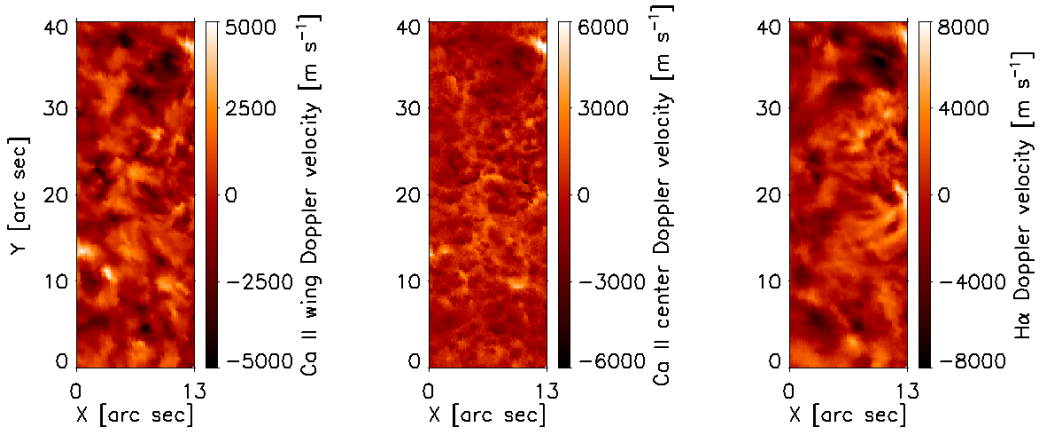

Figure 4.15: Maps of instantaneous Doppler velocities at $\Delta\lambda = \pm 13$ pm from the line center of Ca II 854.2 nm (left), in the center of Ca II 854.2 nm (middle), and the center of Hα (right) at 18:24 UT.

disc maps of continuum intensity, magnetic-field strength, and inclination were cropped to match the ROI. For the magnetic-field strength lower than $|B| < 125$ G, the inversion code returns unreliable LOS inclinations $\theta \approx 90°$ because of noisy Stokes Q and U signals. To remove these unreliable values, we applied a mask that set θ to zero in the regions where $|B|$ was below this limit. Figure 4.16 shows the resulting masked maps of photospheric LRF inclination and maps of $|B|$ in logarithmic scale.

- **Spatial alignment**
  The alignment procedure was completely discussed in Section 4.1.3. The satisfactory spatial alignment between the co-temporal image pairs GST – HMI is achieved with the cross-correlation coefficients of 0.90.

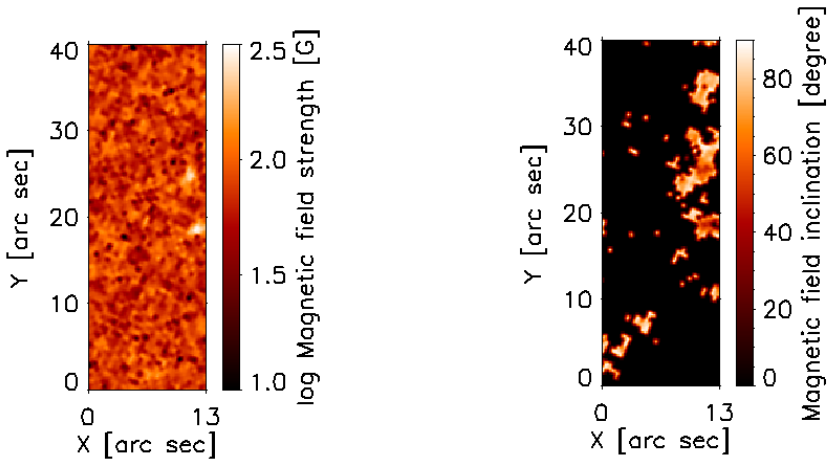

Figure 4.16: Maps of photospheric magnetic-field strength and inclination in the BBSO ROI of October 3.

4.4 IRIS data sets

The Interface Region Imaging Spectrograph (IRIS, De Pontieu et al., 2014) is a small explorer spacecraft, which provides simultaneous spectra and images of the photosphere, chromosphere, transition region, and corona with 0.33″–0.4″ spatial resolution, 2 s temporal resolution and 0.05 Å spectral resolution over a FOV of up to 175″ × 175″. IRIS was launched into a Sun-synchronous orbit on 27 June 2013 using a Pegasus-XL rocket and consists of a 19-cm UV telescope that feeds a slit-based dual-bandpass imaging spectrograph. Its primary goal is to understand how heat and energy move through the lower levels of the solar atmosphere. IRIS is sensitive to emission from plasma at temperatures between 5000 K and 10 MK and it is designed to study the flow of mass and energy through an interface region between the photosphere and corona. Approximately eight GB of data are acquired by IRIS each day and made available for unrestricted use within a few days after the observation. For more details, the reader can refer to De Pontieu et al. (2014). Figure 4.17 shows a schematic view of the IRIS spacecraft.

4.4.1 Instrument

IRIS carries a single instrument: an ultraviolet telescope combined with a grating spectrograph. The Cassegrain telescope's primary mirror has a diameter of 19 cm. While it will only be able to see about one percent of the Sun at a time, it will be able to resolve features that are as small as 240 km. Such high resolution serve as a microscope for instruments that capture images of the whole Sun simultaneously, for example the NASA's Solar Dynamics Observatory (SDO, Pesnell et al., 2012). The images from IRIS telescope record observations of material at specific temperatures, ranging from 5000 K to 65000 K (up to 10 million K during solar flares) covering the solar photosphere, chromosphere, and transition region. The instrument captures a new image every five to ten seconds, and spectra about every one to two seconds.

IRIS obtains spectra in passbands 1332–1358 Å, 1389–1407 Å, and 2783–

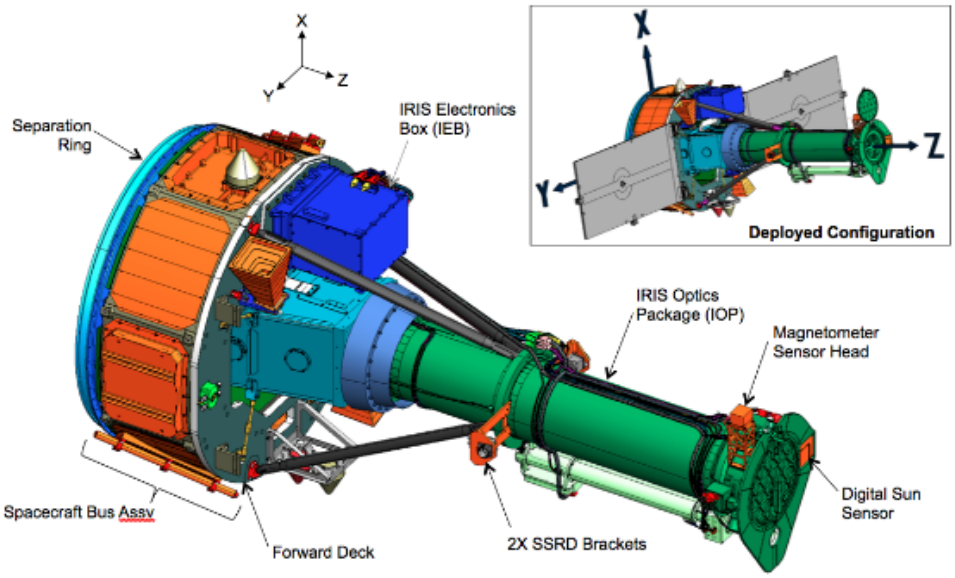

Figure 4.17: Schematic view of IRIS showing the 19-cm UV telescope with and without solar panels. Light from the Cassegrain telescope (green) is fed into the spectrograph box (light blue).

2834 Å including spectral lines that are formed in the chromosphere (Mg II h 2803 Å and Mg II k 2796 Å) and transition region (C II 1334/1335 Å and Si IV 1394/1403 Å). Slit-jaw images that sample regions up to $130'' \times 175''$ at a variety of spatial samplings (from $0.33''$ up) in four different passbands (C II 1330 Å, Si IV 1400 Å, Mg II k 2796 Å, and Mg II wing 2830 Å) can be taken simultaneously with spectral scans. The fully reduced and calibrated level-2 data, used in our analysis, were retrieved from the web pages `https://iris.lmsal.com/search/`.

4.4.2 Observations

We studied 23 level-2 data sets observed in the lines Mg II k 2796.35 Å and h 2803.52 Å (Abbasvand et al., 2021). Details of the data sets are presented in Table 4.4. The targets were quiet Sun and weak active regions located close to the center of the solar disc. IRIS provides high-resolution slit-jaw images (SJIs) as well as spectra of areas covered by the slit. These observations had the spatial sampling of $0.33''$/pixel along the slit and $0.33''$/pixel perpendicular to the slit with the exception of OBSID 3660106120, where the spatial sampling was $1''$/pixel. The spectral pixel size was 51.2 mÅ. We used continuous series of spectral scans that were not contaminated by tracks of cosmic particles. Usually, only one slit position was utilized, but in four cases of active-region observations we included two positions to increase the statistical weight of our results. The IRIS slit-jaw images in the 2796 Å passband were used to align the spectroscopic observations with magnetic-field maps. We have to note that in eight data sets (QS1, QS2, AR1, AR5, AR6, AR7, AR8, and AR9) the slit-jaw images were not recorded.

The IRIS Mg II k&h calibrated level-2 data have been processed for dark current subtraction, flat-field correction, geometrical correction and wavelength

Table 4.4: List of IRIS observations. Data labels are: QS for quiet Sun and AR for active region

Data	Date and Time	Slit position	OBSID	Raster Cadence [s]	t_{exp} [s]	No. of spectral scans
QS1	2017-05-22 07:31UT	1	3633105426	24.7	2	648
QS2	2019-03-03 14:16UT	1	3630109417	36.7	8	400
QS3	2019-05-17 08:54UT	1	3620106017	20.8	4	280
QS4	2019-05-20 09:05UT	1	3620106017	20.8	4	200
QS5	2019-05-25 08:44UT	1	3620106017	20.8	4	230
QS6	2019-06-14 06:43UT	1	3620106417	20.8	4	380
QS7	2019-06-15 11:13UT	1	3620106417	20.8	4	450
QS8	2019-06-16 11:13UT	1	3620106417	20.8	4	450
QS9	2019-06-19 08:09UT	1	3620106417	20.8	4	240
QS10	2019-06-19 11:09UT	1	3620106417	20.8	4	420
QS11	2019-07-06 07:30UT	1	3660106017	20.8	4	230
QS12	2019-07-17 07:29UT	1	3660106017	20.8	4	175
AR1	2015-06-25 07:29UT	1	3630105426	24.7	4	199
AR2	2015-07-08 22:16UT	4	3660106120	20.8	4	400
AR3	2015-07-22 14:47UT	1	3660108117	36.7	8	431
AR4	2015-07-22 14:47UT	2	3660108117	36.7	8	431
AR5	2017-05-20 07:31UT	1	3633105426	24.7	2	630
AR6	2017-05-20 07:31UT	3	3633105426	24.7	2	630
AR7	2017-05-21 07:31UT	1	3633105426	24.7	2	300
AR8	2017-05-21 07:31UT	3	3633105426	24.7	2	300
AR9	2017-05-25 07:33UT	2	3633105426	24.7	2	430
AR10	2019-06-12 07:01UT	1	3620106417	20.8	4	400
AR11	2019-06-12 07:01UT	4	3620106417	20.8	4	400

calibration (De Pontieu et al., 2014; Wülser et al., 2018). We then performed a radiometric calibration to convert the IRIS data, originally in units of data number (DN), into absolute intensity units (erg s^{-1} cm^{-2} sr^{-1} $Å^{-1}$) applying the `iris_calib_spectrum` function, which is available in the IRIS package of the SolarSoft system (Freeland and Handy, 1998). We used time-dependent effective areas (in cm^2) for the radiometric calibration by specifying the date and time of each observation. For each position along the slit of each data set, the mean profile calibrated in absolute intensity units was obtained by time-averaging over the observing period. It was used to find the most appropriate local semi-empirical model.

4.4.3 Data processing

- **Doppler velocity**
  Doppler shifts of the k&h emission and central reversal were measured to obtain chromospheric Doppler velocities required for the calculation of acoustic fluxes. An illustration of the measurement methods is shown in Fig. 4.18. We looked for the positions of the central reversal and the emission core in

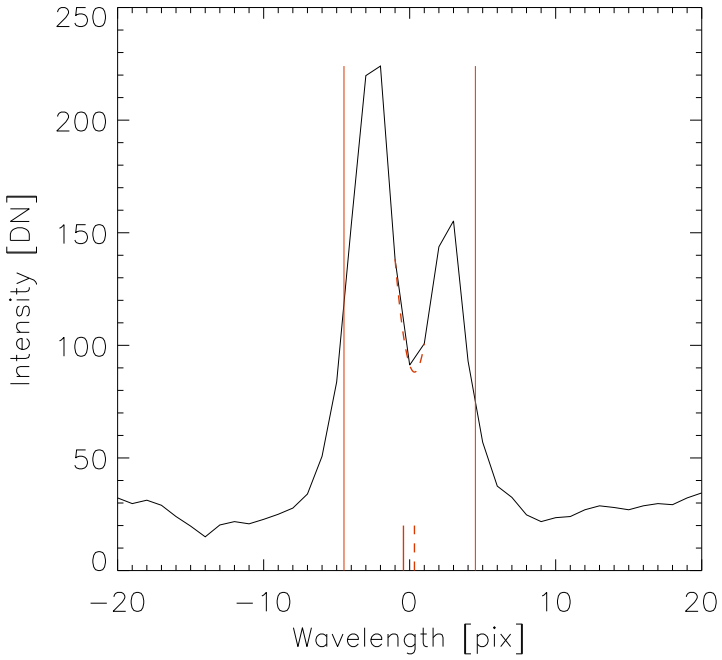

Figure 4.18: Doppler shifts measurement in observed Mg II k profile: parabolic fit for the central reversal and double-slit method for the emission core.

a spectral region 2.05 Å (40 pixels) wide around the approximate line center. The central-reversal position was determined by means of the 3-point parabolic fit of the profile minimum between the two emission peaks. For those profiles where the central reversal was missing (single-peaked emission profiles), the central-reversal velocity was set to zero and marked as an outlier.

Doppler shifts of the emission core, including both emission peaks, were measured by means of the double-slit method (Garcia et al., 2010) described in Section 4.2.3. We selected the "slit" distance to match the half intensity difference between the emission maximum and the absorption-profile minimum, so that shifts of the whole emission core were measured independently of the emission peaks and central reversal. Because the widths of the k&h emission cores change with physical conditions in the chromosphere, the "slit" distance was adapted to the emission-core width measured for each time instant and position along the spectrograph slit.

The shifts were converted into Doppler velocities, defining the reference zero as the time-average of measurements for each position along the slit separately, and 2D time-position Dopplergrams were constructed. Outliers and failures of measurements were replaced by interpolated values obtained by median filtering (5×5 pixels surroundings) of these Dopplergrams. This way, pairs of Dopplergrams for the k and h lines were obtained. Because the Dopplergrams in the pair were always nearly identical, their average (Fig. 4.19) was used for the acoustic-flux calculation.

- **Model atmospheres**
  The best-matching models were obtained by fitting synthetic k&h profiles

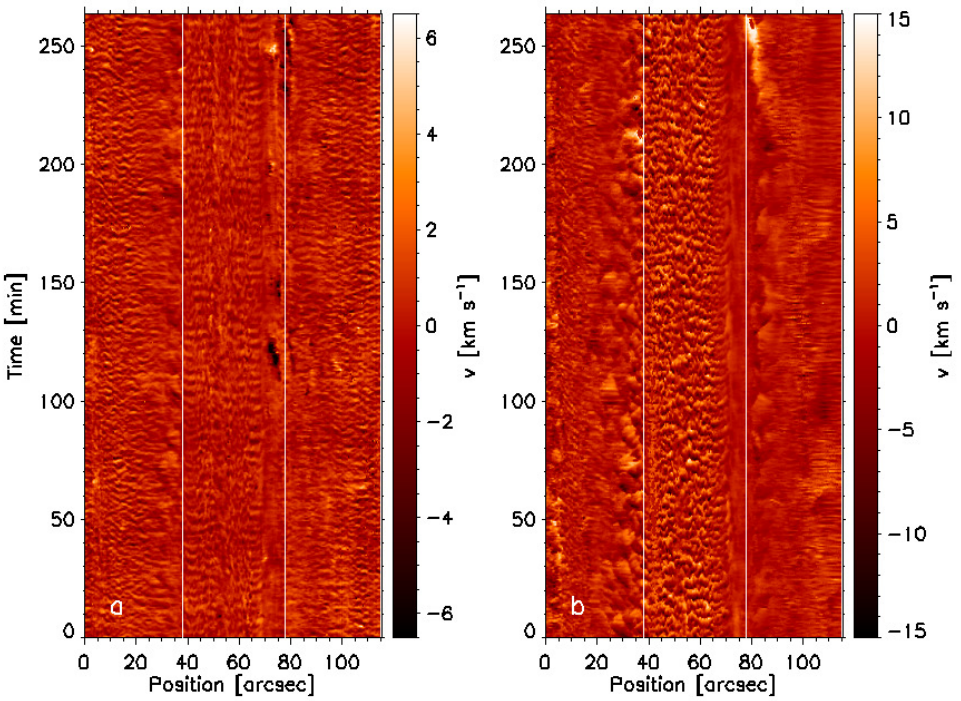

Figure 4.19: Example of a Dopplergram – data set AR4. *a* – velocities of the emission core; *b* – velocities of the central reversal. White vertical lines delimit a magnetic region.

to the observed time-averaged ones. We have to note that the observed profiles have broader emission cores and shallower central reversals than our pre-computed synthetic profiles. This is caused partly by the IRIS instrumental profile, which can be described by a Gaussian function with a full width at half maximum of 53 mÅ (De Pontieu et al., 2014). A major part of the broadening, however, is model-dependent. Judge et al. (2020) pointed out that the effect can be explained by 3D radiative transfer but when 1D models are used, the broadening is mimicked by micro- and/or macroturbulent motions. Because the microturbulence is fixed in our grid of models, we adopted the macroturbulence as a free parameter. The macroturbulence can be approximated by a Gaussian distribution of velocities. So, the synthetic profiles were first convolved with a Gaussian kernel that included the instrumental profile and macroturbulence and then compared with the observed ones.

The model atmospheres were assigned to different positions along the slit of each data set in two steps: (1) to find the best-matching initial VAL model and macroturbulent velocity and (2) to select the optimal final model from the grid of scaled models. Because we do not know the height profiles of the velocity fields and the velocities themselves are small, we simply used the static code, which computed only a half of the synthetic profile, beginning at $\Delta\lambda = 0$. The whole synthetic profiles were completed by mirroring and the observed time-averaged profiles were also symmetrized. First, synthetic profiles of four initial VAL models convolved with macroturbulent velocities characterized by Gaussian σ in the range of 0–8 $\mathrm{km\,s^{-1}}$ and the

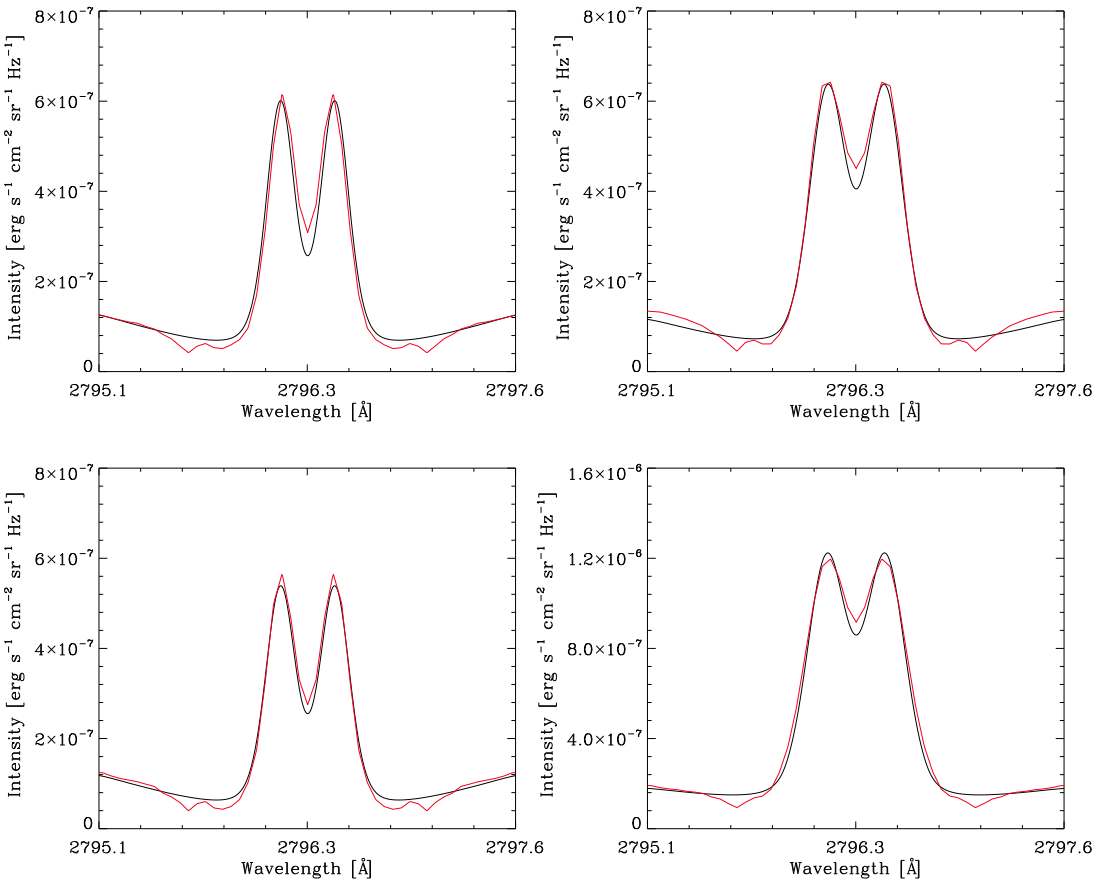

Figure 4.20: Examples of fit of Mg II k synthetic profiles (black) to the observed time-averaged ones (red) for two different positions in quiet (QS5, left column) and active (AR7, right column) regions.

instrumental broadening with equivalent $\sigma \simeq 2.41$ km s^{-1} were compared with the observed profiles to find the best match, that is, the minimum of the sum of squared differences between the convolved synthetic and observed time-averaged profiles (merit function). The matching distributions of macroturbulent velocity were characterized by $\sigma = 4$–7 km s^{-1} with a maximum at 5.5 km s^{-1}. Then the matching initial VAL model and macroturbulent velocity at each position along the slit were used as an input to the second step. Synthetic profiles produced by the grid of models derived from the initial one were convolved with the macroturbulent velocity and instrumental broadening and the final model for each position along the slit was selected by minimizing the merit function. The fit of synthetic to time-averaged observed profiles is illustrated in Fig. 4.20, where two examples of quiet-Sun profiles (*left*) and two of active region (*right*) are shown.

- **Magnetic field**
  The photospheric magnetic-field strength and inclination are necessary for the acoustic-flux calculation. The magnetic-field maps are a data product from the Helioseismic and Magnetic Imager (HMI, Schou et al., 2012) onboard the Solar Dynamics Observatory (SDO, Pesnell et al., 2012). Data were retrieved using the Very Fast Inversion of the Stokes Vector code

(VFISV, Borrero et al., 2011; Centeno et al., 2014). The procedure was discussed in Section 4.1.3. Because the HMI Stokes Q and U signals were noisy in weak magnetic-fields ($|B| < 125$ G), the inversion code returned false values of the inclination $\theta \approx 90°$. We applied a mask allowing to accept inclination values only when $|B|$ was above 125 G.

- **Spatial alignment**
  The HMI data sets were obtained at the middle instant of each observation, including continuum intensity, magnetic-field strength, and inclination. Then the HMI and IRIS continuum images were aligned by means of a semi-automatic spatial alignment procedure described in detail in Section 4.1.3. For those data sets where continuum slit-jaw images were not recorded, we aligned IRIS and HMI images in accordance with heliographic coordinates of IRIS observations.

Chapter 5

Radiative cooling

In Section 2.2, it is mentioned that if there is no heating or cooling of the solar atmosphere by non-radiative mechanisms or any types of wave motions, then the sum of all net radiative cooling and heating from the atmosphere would be zero. In other words, the total net radiative loss in a hydrostatic state signifies the amount of non-radiative heating energy flux necessary to maintain the prescribed temperature structure at the given depth. In this chapter, the net radiative losses are assessed from the chromospheric spectral lines and continua. These are important in knowing cooling and heating mechanism throughout the solar atmosphere. In the following, I refer to the work of Vernazza et al. (1981), who described the net radiative cooling rate in a comprehensive way.

The net radiative cooling for a line transition can be defined as

$$h\nu\left[n_u\left(A_{ul}+B_{ul}\bar{J}\right)-n_l B_{lu}\bar{J}\right]\equiv\Phi_{ul}, \tag{5.1}$$

where n_l and n_u are the lower and upper level number densities, A_{ul}, B_{ul}, and B_{lu} are the Einstein emission and absorption coefficients, and

$$\bar{J}=\int\chi_\nu J_\nu d\nu, \tag{5.2}$$

where χ_ν is the line absorption coefficient normalized ($\int\chi_\nu d\nu=1$) and J_ν is the mean intensity at the frequency ν within the spectral line. The loss function can be derived from Equation 5.1 as

$$\Phi_{ul}=h\nu n_u A_{ul}\rho, \tag{5.3}$$

where ρ is net radiative bracket (Thomas, 1960), given by

$$\rho=1-\frac{\bar{J}}{S^L} \tag{5.4}$$

The frequency-independent line source function S^L only depends on the number densities and the statistical weights g_u and g_l according to

$$S^L=\frac{2h\nu^3}{c^2}\left[\frac{n_l}{n_u}\frac{g_u}{g_l}-1\right]^{-1} \tag{5.5}$$

and S^L relates to $\bar{J}$ and the statistical equilibrium parameters ϵ and B^S by

$$S^L=\frac{\bar{J}+\epsilon B^S}{1+\epsilon}. \tag{5.6}$$

Assuming complete frequency redistribution (CRD) throughout the line, the monochromatic line source function S_ν^L is equal to S^L. In the resonance lines of Ca II, Mg II, Lα and Lβ, the source function and mean intensity are computed using the partial-redistribution method (more details are described in Appendix A of Vernazza et al., 1981).

The net radiative cooling rate for the bound-free transition from continuum m to bound state k is

$$\Phi_m \equiv 4\pi n_m \left[b_m^{-1} \int_{\nu_m}^{\infty} a_m(\nu)\beta_\nu(\alpha_\nu + J_\nu)d\nu - \int_{\nu_m}^{\infty} a_m(\nu)d\nu \right] \tag{5.7}$$

(here $\alpha_\nu = 2h\nu^3/c^2$, $\beta_\nu = exp[-h\nu/kT]$, $b_m = n_m n_k^*/n_k n_m^*$, and a_m is the photoionization cross section). The photoionization rate is

$$R_{mk} = 4\pi \int_{\nu_m}^{\infty} (h\nu)^{-1} a_m(\nu) J_\nu d\nu. \tag{5.8}$$

From Equations 5.7 and 5.8, we can write

$$\Phi_m \sim h\nu_m(n_k R_{km} - n_m R_{mk}) \tag{5.9}$$

where R_{mk} and R_{km} are photoionization and radiative recombination rates, respectively, and ν_m is the ionization-limit frequency.

In Figure 5.1, the net radiative cooling rates per unit volume due to the lines and continua of hydrogen for VAL C model are plotted. The plot shows that Lα line gives the most important hydrogen radiative cooling rate for $T > 10^4$ K. This rate continues throughout the plateau region in the temperature range $2 \times 10^4 < T < 3 \times 10^4$ K. The total contribution of all cooling rates (all hydrogen transitions) is plotted by a solid line in the same figure and it is small throughout the chromosphere.

The cooling rates due to constituents other than hydrogen are shown in Figure 5.2. They are calculated for VAL C and plotted for the total hydrogen contribution, the Ca II K, H, and infrared triplet lines, the Mg II h, k lines, the H^- ion, the Mg I b triplet and Na I D lines, the lines Si II λ 181.6 nm and He I λ 58.4 nm, and the continua of Si II at 152.4 nm and 168.1 nm, Fe I at 157.5 nm and 176.8 nm, Mg I at 162.2 nm, and He I at 50.4 nm. A list of integrated net radiative cooling rates $\int \Phi dh$ (Φ is a function of depth h) for the Ca II and Mg II lines, Lα, and H^- is shown in Table 5.1. Negative values of Φ in the $T_{\rm min}$ region are assumed to be zero in each integral.

In techniques developed by Carlsson and Leenaarts (2012b), the net effect of all the radiative transfer was explained as a combination of three factors: (i) an optically thin radiative loss function, representing the local energy loss through radiation of an atom in the right ionisation stage, (ii) the probability of escaping this energy from the atmosphere, and (iii) the fraction of atoms in the ionisation stage. As there is no obvious general physics-based approximation, all these factors must be empirically determined.

In another part of their paper, Carlsson and Leenaarts (2012b) attempted to model the chromospheric absorption of radiation emitted in the corona. Accordingly, almost half of this radiation is emitted towards lower layers such as chromosphere and among this the major rate can be absorbed in the chromosphere. The corona emissions are mainly in the far UV band, and indicate the

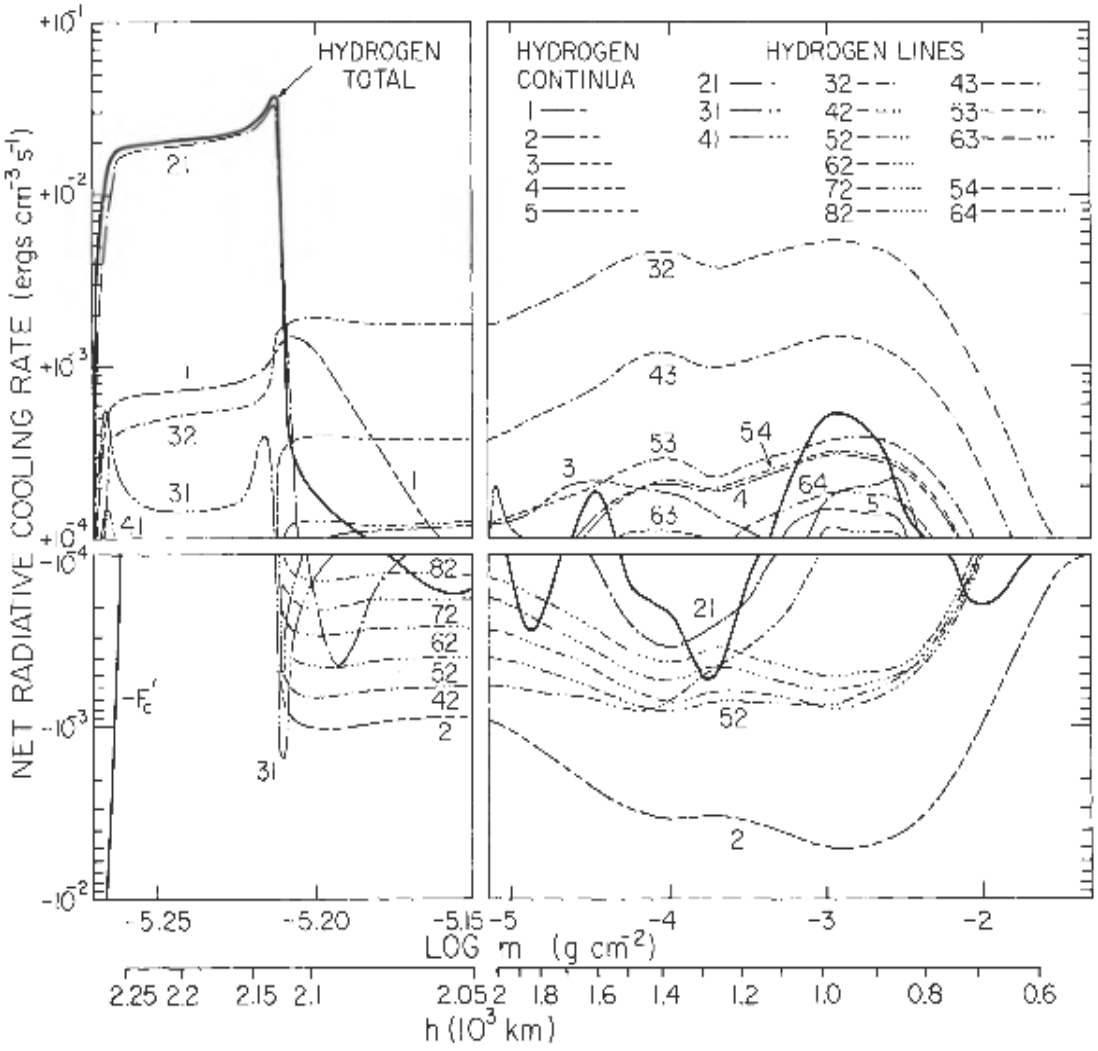

Figure 5.1: Net radiative cooling rates for hydrogen transitions computed from VAL C. The negative of the conductive flux gradient is shown in the lower left panel (Figure 48 of Vernazza et al., 1981).

Constituent	Net cooling rate
Ca II K	7
Ca II 854.2 nm	7
Ca II 849.8 nm	6
Ca II 866.2 nm	5
Ca II H	5
Mg II k	5
Mg II h	4
Lα	3
H^- (bf)	2
H^- (ff)	2
Total	46

Table 5.1: Integrated net radiative cooling rates in units of 10^5 erg cm^{-2} s^{-1} (Table 29 of Vernazza et al., 1981)).

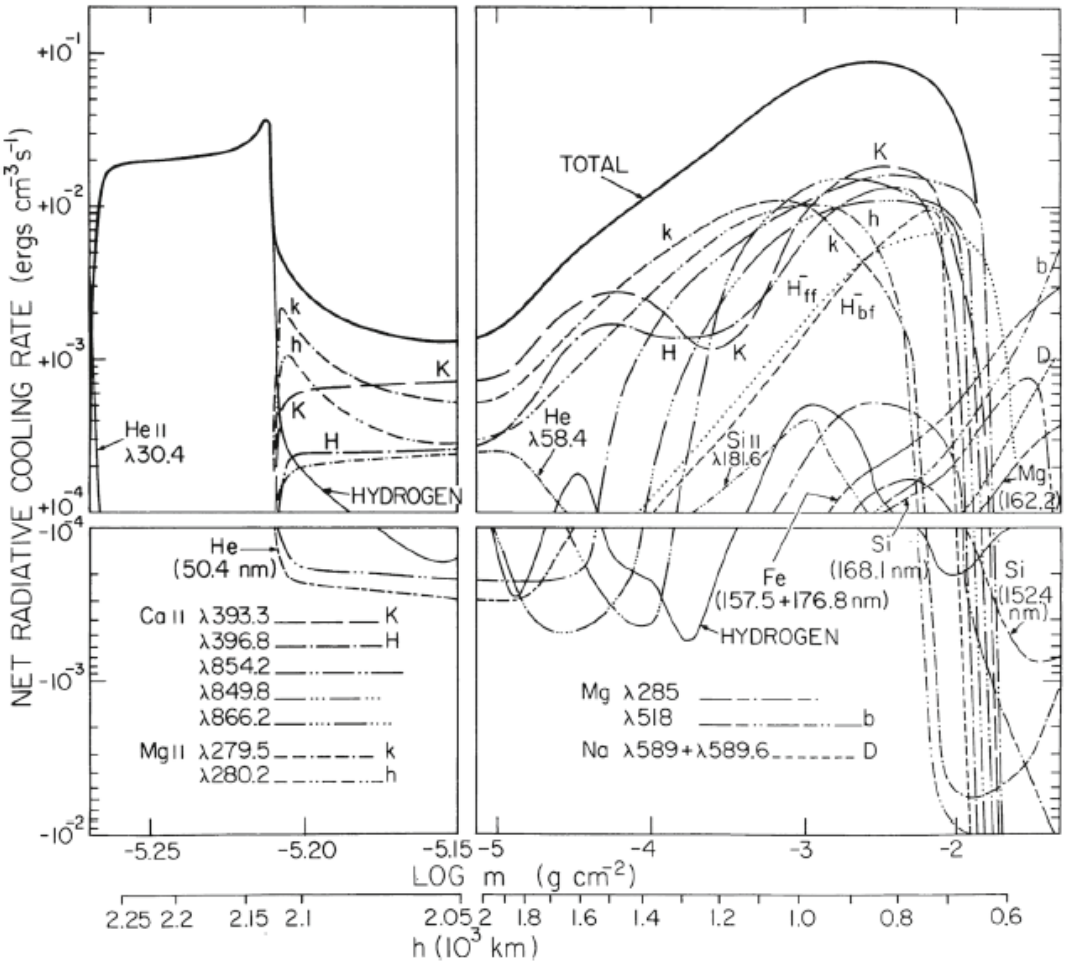

Figure 5.2: Net radiative cooling rates for H, Ca II, Mg II, H^- and other constituents calculated from VAL C (Figure 49 of Vernazza et al., 1981).

extinction of sources at H I, He I, and He II continua. Most of 3D radiative transfer codes are already used to compute the atmospheric radiation. When using 1D models, the spreading of radiation in the horizontal directions is ignored and this can lead to large heating when radiation of emission of small local sources is forced to be absorbed in an individual vertical radiative column.

Figure 5.3 of the Leenaarts (2020) shows an example of radiative losses computed in a 3D simulation with the Bifrost code (Gudiksen et al., 2011). The photospheric cooling rate per mass has a small contribution up into the chromosphere and is largest in the photosphere. Coronal radiative losses are significant throughout the whole corona. The largest contribution is in the transition region and just below the transition region owing to Lα cooling. Cooling rate of Ca II and Mg II lines and heating from the absorption of coronal radiation continues relatively moderate somewhat deeper in the chromosphere. The radiative losses are very sensitive to temperature, whereas the mechanisms that dissipate non-thermal energy are not so sensitive to it.

In our work, we use the 1D non-LTE radiative-transfer code based on the MALI technique (Heinzel, 1995) to calculate radiative losses in the chromosphere (Section 3.4). Having computed the atomic level populations for all bound states

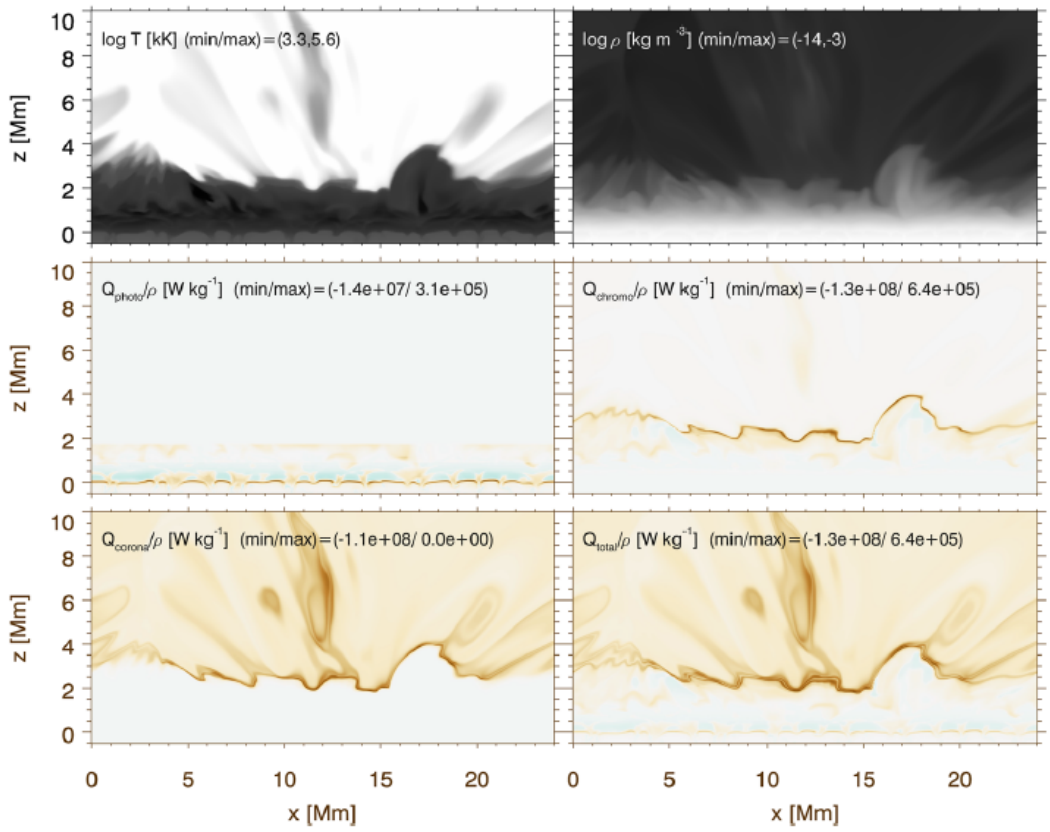

Figure 5.3: Radiative cooling act in different atmospheric regimes computed in a 3D simulation with the Bifrost code. *Top row*: temperature and density through the simulation. The panels labeled Q_{photo}, Q_{chromo}, Q_{corona} and Q_{total} show the photospheric, chromospheric, coronal and the sum of the previous three panels losses per mass unit using the methods from Carlsson and Leenaarts (2012b), respectively. The lower-right panel clearly shows that the largest radiative losses occur in the transition region. Brown color indicates cooling, blue color represents heating. Figure reproduced from a simulation by Leenaarts (2020).

and the mean radiation fields of all line transitions, we evaluate the net radiative cooling rates using formula 5.1 (Eq. (21) of Vernazza et al., 1981). For bound-free hydrogen continua we integrate the differences between emission and absorption over the continuum wavelengths; Ca II and Mg II continua are neglected. We tested this standard approach using the VAL C model and our loss function relatively closely resembles that shown in Fig. 5.2. Also, our total losses integrated over chromospheric heights are in agreement with those in Table 5.1. We note that these losses are completely dominated by hydrogen, Ca II, and Mg II lines.

Chapter 6

Deposited acoustic flux

6.1 Acoustic flux

Acoustic waves, generated by turbulent motions, were suggested for the energy transport from lower layers of the solar atmosphere to the upper layers and their heating by Biermann (1948) and Schwarzschild (1948). Numerous theoretical and observational studies have pursued this aim. Carlsson et al. (1997) performed different simulations using sequences of measured velocities, not including short-period waves, to model sub-photospheric velocities at the upper boundaries of solar surface. Their work reproduced brightness fluctuations and symmetries in and around the line core of Ca II H. This simulation showed a large temperature outings on time average, while there was no temperature rise outwards. As a consequence, they concluded that in non-magnetic areas, chromospheric temperature rise could not exist. On contrary, the UV observations of the solar chromosphere exhibit emissions everywhere and all of the time (Kalkofen et al., 1999).

Reardon et al. (2008) studied properties of the solar chromosphere in the high-frequency regime using the chromospheric power spectra in the Ca II 854.2 nm line and found the presence of significant oscillatory fluctuation power above the cutoff frequency ($5.2 < \nu < 10$ mHz). It means that the chromospheric high-frequency power is not only the result of short-period waves, but also is the signature of turbulence, which is generated within the chromosphere by shock oscillations near the cut-off frequency. They also discussed that the acoustic flux carried to the chromosphere (1800–2500 W m^{-2}) and atmospheric gravity waves flux (5000 W m^{-2}) found by Straus et al. (2008), on average, can heat the chromosphere. Still there are many uncertainties in the frequency distribution of acoustic flux in the photosphere, where the observations cannot detect them.

Contributing to the atmospheric-heating debate, Bello González et al. (2010a) analysed the high-resolution spectropolarimetic data taken with the IMaX/Sunrise instrument and reported that acoustic flux is mainly found in intergranular lanes, rapidly evolving granules, and in regions with splitting granules and forming dark regions. They computed the power of the energy flux of $\sim$ 6400–7700 W m^{-2} at the height of $\sim$250 km in the 5.2–10 mHz range, twice larger that their previous computations. They used the high spatial resolution data to confirm that acoustic waves, coming from energetic processes occurring at small scales, play an important role in energy transport through the quiet-Sun atmosphere. Ra-

jaguru et al. (2019) recently found that the mean acoustic energy flux over the quiet Sun between the upper photosphere and lower chromosphere and over the 2-5 mHz frequency is about 2200–2600 W m^{-2}, twice larger than was estimated by Jefferies et al. (2006).

Significant evidences from the theoretical research show that acoustic waves can heat the internetwork regions (i.e., the non-magnetic regions) on the Sun (Ulmschneider and Musielak, 2003). Based on simulations, Carlsson and Stein (1992) reported that when the acoustic wave dissipation is fully employed, the Ca II H line behavior is very similar to the observed one. Cuntz et al. (2007) studied the physical nature of acoustic heating in the solar chromosphere using three different lines. They claimed that high-frequency acoustic waves are sufficient to heat the internetwork regions in the solar chromosphere.

Beck et al. (2009) investigated the energy content of velocity oscillations in several photospheric spectral lines and the chromospheric Ca II H line at the heights between 250 and 1000 km. They found that the energy of the rms velocity of a spectral line (Fe I 396.93 nm with the formation height at 600 km) in the wing of Ca II H was already below the chromospheric energy requirement given by Vernazza et al. (1981), while the order of mechanical energy at around h=500 km is as same as the chromospheric radiative losses. The energy content in higher layers is insufficient to maintain the temperature stratification of the semi-empirical models.

In 2005, Ulmschneider et al. (2005) presented an assessment of the chromospheric heating by short-period waves ($<$ 20 s). They produced a reasonable solar chromospheric model with a monochromatic wave of 20 s period and a realistic amount of acoustic flux. They discussed that 1D simulations with wave spectra are deficient due to the fact that most of the short period waves can be destroyed by shock merging. Wedemeyer-Böhm et al. (2007) used 3D numerical simulations to show that a factor of 10 in the short-period energy fluxes are missed in too low spatial resolution. Carlsson et al. (2007) investigated high-resolution time sequences of Ca II H filtergrams from SOT/Hinode and reported that the high-frequency acoustic flux in the quiet chromosphere is very low to balance the chromospheric radiative losses, it is only 800 W m^{-2}.

For two reasons it is highly difficult to detect the short-period waves from observational point: (1) the response functions for the velocity information extend over a height range of at least 200 km (a maximum around 200 km), which severely decreases any wave signal with periods shorter than 60 s; (2) the waves are expected to have small horizontal extension well below 1″. During the last decade, efforts were undertaken to overcome the observational obstacles. The presence of short-period waves and their strong spatial and temporal alternation is demonstrated in a wavelet analysis of the Fe I 543.4 nm line data acquired by a 2D spectrometer (Wunnenberg et al., 2002). It has been pointed out that the observable signal of small-scale fluctuations along the line of sight, short-period waves, is diminished due to expanding response function over the atmospheric heights (e.g. Cram et al., 1979; Mein and Mein, 1980).

Bello González et al. (2009) calculated transmissions of velocity amplitudes in the VAL C solar atmospheric model assuming velocities of vertically propagating waves with moderate amplitudes $v_0(z)$ and periods from 30 to 190 s. They hypothesized that the acoustic energy flux is roughly constant through the atmo-

sphere, therefore

$$\rho(z) \cdot v_0^2(z) \approx \text{const}, \tag{6.1}$$

or

$$v_0(z) = v_0(z=0) \cdot \exp^{z/(2H)}, \tag{6.2}$$

where $\rho(z)$ is the mass density and H is the density scale height assumed to be 110 km. The wave propagation velocities were derived from the phase velocity using the dispersion relation

$$k_z^2 = \frac{\omega^2 - \omega_{\rm ac}^2}{c_s^2} - \frac{(\omega^2 - \omega_{\rm BV}^2)k_h^2}{\omega^2}, \tag{6.3}$$

where $\omega = 2\pi\nu$ is the angular frequency, $k_{\rm z}$, $k_{\rm h}$, $\omega_{\rm ac}$, and $\omega_{\rm BV}$ are the vertical and horizontal wave numbers, the acoustic cut-off and Brunt-Väisälä frequencies, respectively, with $\omega_{\rm ac} = \gamma g \cos\theta/(4\pi c_{\rm s})$ and $\omega_{\rm BV} = \sqrt{\gamma - 1}\, g/c_s$. Here, $c_{\rm s} = \sqrt{\gamma P_{\rm g}/\rho}$ is the sound speed, $\gamma = 5/3$ is the ratio of specific heats, and g the surface gravity acceleration. The sound speed was taken as $c_{\rm s} = 7$ km s^{-1}; $P_{\rm g}$ is the gas pressure, ρ the density, and θ the magnetic-field inclination in the photosphere, which reduces the acoustic cut-off frequency (Cally, 2006). Hence the acoustic cut-off frequency is $\omega_{\rm ac} = 3.26 \times 10^{-2}$ s^{-1} ($\nu_{\rm ac} = 5.2$ mHz) and the cut-off period is $P_{\rm ac} = 193$ s.

Wave propagation conditions are strongly connected with the acoustic cut-off frequency. It plays an important role in finding regions in the solar atmosphere where the waves are reflected. Lamb (1932) studied both an isothermal and non-isothermal atmosphere with a linear temperature profile and introduced the concept of acoustic cut-off. Later, several authors followed his work and presented different formulation for the cut-off period (e.g. Routh et al., 2006; Fawzy and Musielak, 2012; Routh and Musielak, 2014). Numerical simulations of acoustic waves were done by e.g. Ulmschneider et al. (1978); Carlsson and Stein (1997); Fawzy and Musielak (2012) to study and explore the acoustic cut-off frequency and the contribution of the waves to atmospheric heating. Wiśniewska et al. (2016) studied acoustic waves observationally and demonstrated that the most of analytical formulae obtained by previous attempts could not interpret well the observational data, because the cut-off frequency does not change with height through the solar chromosphere as expected. In the context of oscillations, it is proposed that waves with frequencies below below 4 mHz become fading and only higher frequencies freely propagate upward to the chromosphere and their amplitude grows (e.g., Lites and Chipman, 1979; Lites et al., 1982). In other report in case of magnetic field and its role in propagation, Heggland et al. (2011) presented that the longer periods greater than 4 min can easily travel to the transition region within the presence of high magnetic fields. A review on some observations that can confirm this theory was also published by De Pontieu et al. (2003, 2005).

The magnetic-field topology imposes a significant effect on the waves propagating into the solar atmosphere by lowering the cut-off frequency for acoustic waves, thus allowing the trapped waves with frequencies below the cut-off frequency ($\nu_c = 5.2$ mHz) to propagate into the upper atmosphere (Stangalini

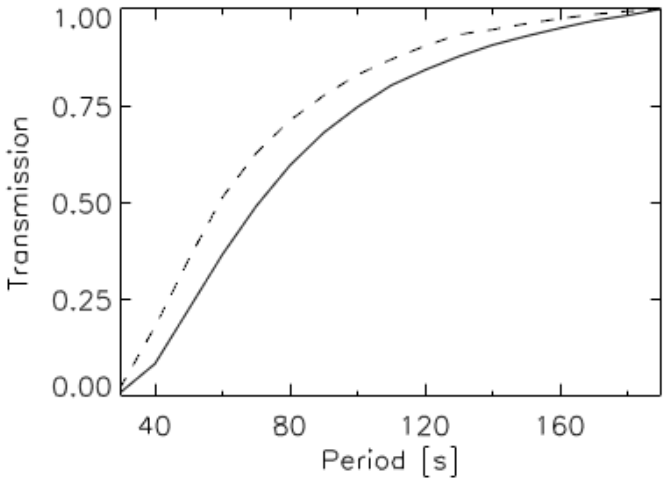

Figure 6.1: Transmission of solar atmosphere for acoustic waves as a function of wave period with infinite spectral resolution (dashed) and after applying the convolution with spectrometer function and filtering (Bello González et al., 2009, their Fig.3).

et al., 2011; Kontogiannis et al., 2014, 2016). Rajaguru et al. (2019) identified that magnetic filed elements (plages and sunspots), which are relatively less inclined, provide a channel for those lower frequency waves (2–4 mHz) to propagate higher to the chromosphere thanks to the reduction in cut-off frequency.

The phase velocity for vertically propagating waves, $k_{\rm h}$=0, can be derived from Equation 6.3, following Bello González et al. (2009)

$$v_{ph} = \frac{\omega}{k_z} = \frac{c_s}{\sqrt{1-(\omega_{\rm ac}/\omega)^2}}, \tag{6.4}$$

and the group velocity for the energy transportation is

$$v_{gr} = \frac{d\omega}{dk_z} = c_s \cdot \sqrt{1-(\omega_{\rm ac}/\omega)^2}. \tag{6.5}$$

The latter authors plotted the transmission of the acoustic wave amplitudes by the atmospheric model as a function of period (Figure 6.1). They assumed that for P = 190 s the transmission is equal to one. The dashed curve is the result of a spectrometer with infinite resolution and the solid curve results from the convolution of emergent line profiles with the spectrometer's profile and a filtering in wavelength. The velocity power can be corrected using the square of the transmission curves, which is called a "transfer function" $TF(\nu)$ of the atmosphere.

The acoustic flux spectra and the total acoustic flux for the layers where the velocity signal is formed can be estimated as

$$F_{ac}(\nu) = \rho \cdot P_v(\nu) \cdot v_{gr}(\nu)/TF(\nu), \tag{6.6}$$

where ρ is the mass density at the level of formation and the correction of the flux spectra are obtained by dividing the term by $TF(\nu)$. Then the total acoustic flux

over all frequencies between the acoustic cut-off $\nu_{\rm ac}$ and the maximum observed frequency $\nu_{\rm max}$ is

$$F_{\rm ac,tot} = \int_{\nu_{\rm ac}}^{\nu_{\rm max}} F_{\rm ac}\, {\rm d}\nu. \tag{6.7}$$

The transfer function relates to the transmission of the wave amplitudes by the solar atmosphere as a function of frequency. It is proportional to the ratio of the velocity amplitude observable as a Doppler shift of the given line to the true amplitude. Its value is unity if the entire wave signal is observed as the Doppler shift of the spectral line throughout the atmosphere at a given frequency, whereas values smaller than unity represent some loss of the signal because of the extent in height of the spectral-line contribution functions. In general, the most affected are short-period (small-scale) fluctuations. A detailed time-dependent model of the atmosphere is needed to derive this value. In this work, *we set this function equal to unity for all frequencies*, which means that the observed Doppler signal of all waves at a given frequency is detected throughout the solar atmosphere. This rough approximation may lead to underestimated acoustic-flux values at higher frequencies.

The values of gas pressure $P_{\rm g}$ and density ρ are taken in each pixel of the ROIs from the corresponding scaled model atmosphere at two reference heights z_1 and z_2 (Section 3.5). The deposited acoustic flux $\Delta F_{\rm ac}$ is the difference between the incoming acoustic energy flux at the lower reference height z_1 and the outgoing one at the upper reference height z_2,

$$\Delta F_{\rm ac} = F_{\rm ac,tot}(z_1) - F_{\rm ac,tot}(z_2). \tag{6.8}$$

A part of the incoming energy flux is dissipated in the chromosphere between z_1 and z_2 and likely converted into radiation, while the outgoing part continues to propagate higher in the atmosphere. Radiative losses (Chapter 5) that have to be compared with $\Delta F_{\rm ac}$ are integrated over chromospheric layers between the same reference heights.

6.2 Properties of observed waves

The properties of (magneto)acoustic waves were also investigated using the analysis of wavelet spectra in the IRIS data sets (Abbasvand et al., 2021). For each data set and every position along the slit we computed a wavelet spectrum for both Dopplergram series representing the lower and upper boundaries of the studied chromospheric layer. These boundaries were defined using effective formation heights of the Mg II k&h emission cores and central reversals (see Section 3.5). The wavelet analysis was performed using Python's PyCWT package, which is based on Torrence and Compo (1998). In addition to the wavelet spectra utilising the Morlet wavelet as a mother wavelet, we computed also the cross-wavelet spectra and the wavelet coherence comparing data series in the lower and upper formation heights. The cross-wavelet spectrum finds regions in time-frequency space where the time series show high common power. The wavelet coherence, on the other hand, finds regions in time-frequency space where the two time series

co-vary, but do not necessarily have high power. The wavelet coherence allows also to compute the phase shifts between the series.

The wavelet spectra obtained from the Dopplergrams at each observed pixel, that is, a position along the slit in each data set, show a quite complicated pattern (see examples in Fig. 6.2). At the lower-height boundary, a significant power excess is seen in the frequency band around 5 mHz. The islands of the significance on the wavelet power spectrum have an intermittent nature, with a period of an order of 500–1000 s with a significant power, swapping with a period of an order of 200–500 s where the wavelet power is not above the significance threshold for the non-magnetic (quiet Sun) pixels. For the pixels classified as a magnetised atmosphere, where the magnetic induction is above the 125 G threshold, the wavelet power seems to be shifted towards smaller frequencies and the intermittency is more severe, because, in general, the wavelet power is smaller in the magnetised atmosphere.

In the case of the upper-height boundary and the non-magnetic pixels, the wavelet power spectrum is much richer. We observe continuous islands of significant power from 3 mHz to 10 mHz and beyond. The intermittency increases with the increasing frequency such that at frequencies larger than about 10 mHz the islands of significant and insignificant wavelet power swap each about 100 s. In the case of the magnetized atmosphere, the wavelet power seems to be present almost everywhere in the power map.

Cross-wavelet power and wavelet-coherence spectra show a complicated pattern as well. Instead of comparing the wavelet power spectra for each and every observed pixel, we took a statistical approach to learn about the typical or common behavior.

From the wavelet coherence determined for each pixel, we computed the resulting phase shift between the upper- and lower-height boundary of the chromospheric layer as a function of frequency. For each pixel, the phase shift was averaged in the time domain, separately for all time epochs and for those time epochs, where the wavelet coherence was above the significance threshold. From the modeled atmosphere, we determined the geometrical height difference. Knowing these two quantities, we could determine the time lags between the two boundaries and the corresponding phase speeds as a function of frequency. We followed the classical wave description, taking

$$\Delta\varphi = \omega\Delta t \quad \text{and} \quad \Delta h = c\Delta t, \tag{6.9}$$

where $\Delta\varphi$ stands for the determined wavelet phase shift, ω is the frequency, Δt is the time lag, $\Delta h = z_1 - z_2$ the geometrical height difference, and c is the phase speed.

In order to learn about the typical behavior, we averaged the phase shifts over all representation of the non-magnetic (quiet-Sun) pixels and pixels in the magnetised atmosphere. The averaged phase shifts $\Delta\varphi$ computed separately for the non-magnetic and magnetic pixels are plotted in Fig. 6.3. On average, we clearly see indications for the upward propagating waves (the phase shifts are positive) with typical phase shifts from 60 to 100 degrees. We have to say that we do not consider the information obtained for the frequencies smaller than 2 mHz trustworthy, as these frequencies are near the resolution limits 0.12–0.54 mHz given by the lengths of the observing series. The drop of the phase shift between 2 mHz

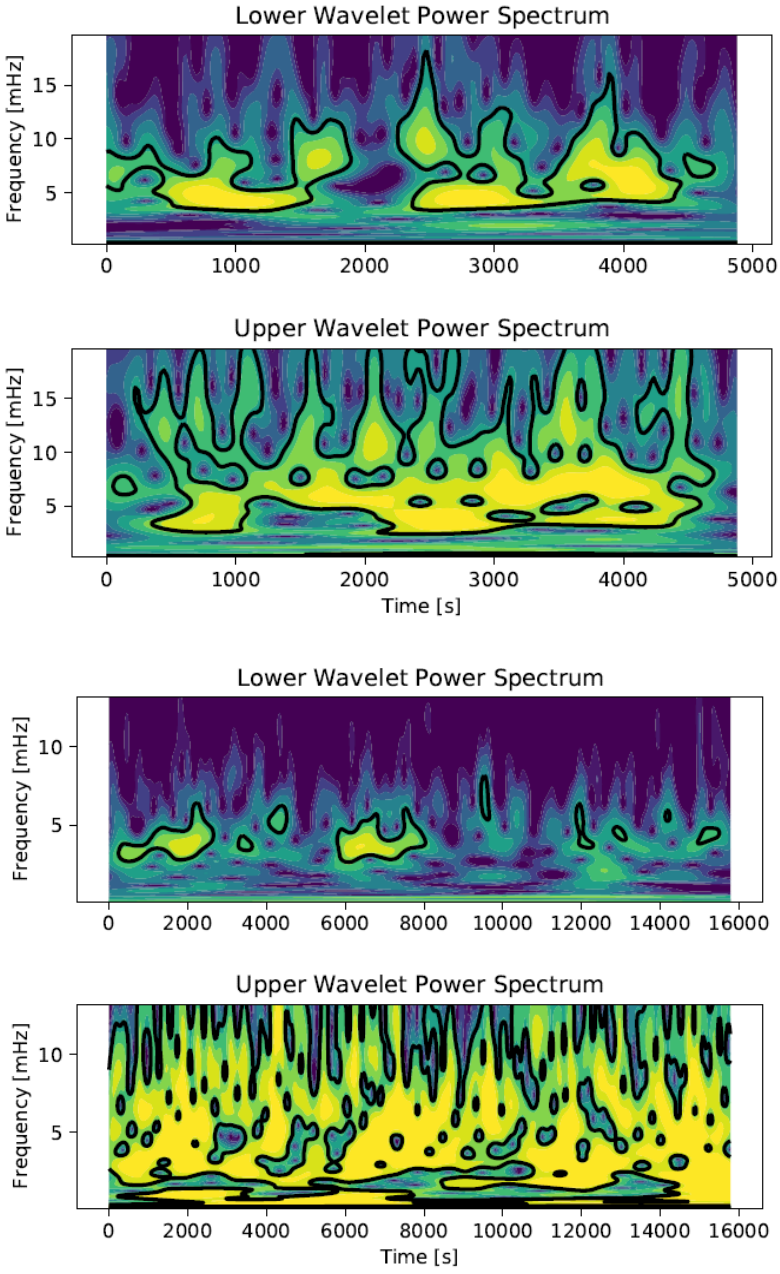

Figure 6.2: Examples of the wavelet power spectra computed for a pixel in the non-magnetic atmosphere (upper pair of plots) and for a pixel classified as the magnetized atmosphere (lower pair of plots), always for the lower- and upper-height boundary of the chromospheric layer under study. The solid black contours encircle the islands of the statistical significance of the power.

and 6 mHz for the magnetised pixels seems significant. In this frequency region, we most often observe a significant wavelet coherence in the magnetic pixels. The phase shifts correspond to the time lags between 30 and 100 s decreasing with frequency. This characteristic time shift was independently confirmed by a cross-correlation of the Dopplergram series in selected pixels.

The mean Δh is about 1100 km for the non-magnetic pixels and about 800 km for the magnetic ones. This allows us to infer the average phase speed corre-

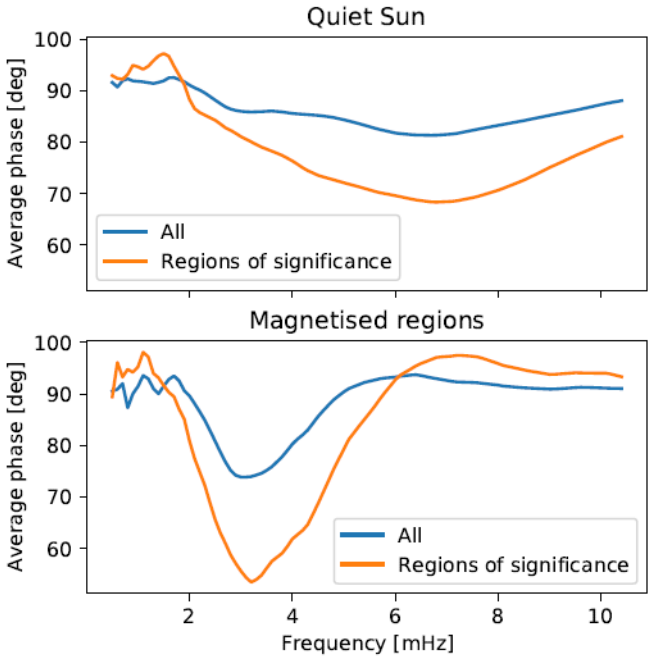

Figure 6.3: Average wave phase shifts between the upper- and lower-height boundaries of the chromospheric layer under study plotted separately for the non-magnetic (upper panel) and magnetic (lower panel) pixels. The averages are plotted for all contributions in the time-frequency wavelet spectrum (blue) and only for those contributions, where a statistically significant wavelet coherence was indicated (orange).

sponding to the wave propagation. These average phase speeds are plotted in Fig. 6.4. According to our atmospheric models, the typical speeds of sound are 7–8 $\mathrm{km\,s^{-1}}$ for the lower-height boundary and 10–12 $\mathrm{km\,s^{-1}}$ for the upper-height boundary. We cannot determine directly the Alfvén speed as we do not know the induction of the magnetic field in these layers. By taking a reasonable estimate of 100 G, we obtain the estimates for the Alfvén speeds of 20–40 $\mathrm{km\,s^{-1}}$.

The Dopplergram visualisation (Fig. 4.19) indicates that the time evolution of the Doppler velocity has a different character at the lower- and upper-height boundaries. Whereas at the lower boundary the Dopplergram series is visually compatible with the pattern of waves, at the upper boundary the wave-like character is suppressed by a structure similar to shocks. That is, the Doppler velocity exhibits a fast increase in magnitude followed by a much slower decrease. This is true for the quiet-Sun regions, but for the magnetized regions, the character of the Doppler velocity resembles waves even at the upper boundary.

The phase speeds for the regions with a large statistical significance, displayed in Fig. 6.4, indicate that the signal with frequencies larger than 2 mHz, which we find trustworthy, spreads with supersonic velocities. With the exception of the frequency range 3–5 mHz for the magnetic pixels, the phase speed monotonously increases with frequency. This is consistent with the nature of shocks, where the fast increases of Doppler velocity are naturally mapped to large frequencies in the frequency space, as the steep increases characteristic of discontinuities.

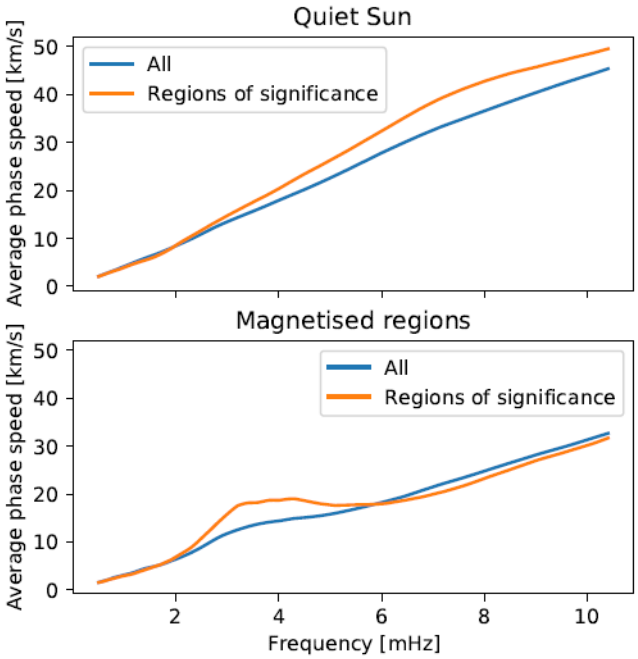

Figure 6.4: Average wave phase speeds between the upper- and lower-height boundaries of the chromospheric layer under study plotted separately for the non-magnetic (upper panel) and magnetic (lower panel) pixels. The averages are plotted for all contributions in the time–frequency wavelet spectrum (blue) and only for those contributions, where a statistically significant wavelet coherence was indicated (orange).

In the frequency range 3–5 mHz for the magnetic pixels, the phase speed is almost constant, at about 18 $\mathrm{km\,s^{-1}}$. This is supersonic and likely corresponds to the presence of the fast magnetoacoustic mode propagating upwards. We need to mention here that the typical inclination of the magnetic field in those pixels is non-negligible but rather small on average. We therefore compare the pixels at the lower- and upper-height boundaries that do not have to share the same field line. Thus, in principle, we cannot observe pure Alfvénic motions. Because of the line of sight (with respect to the direction of the magnetic field) we possibly observe a component of the hydromagnetic waves, and as the derived phase speed is supersonic, we interpret this as a fast mode. At this point we cannot rule out the presence of the flux-tube waves. On the other hand, the wavelet spectra do not resemble the power spectra of the wave trains indicating flux-tube waves (see e.g. Mészárosová and Gömöry, 2020).

Chapter 7

Deposited Acoustic Flux Compared to Radiative Cooling

In this chapter, a quantitative comparison of deposited acoustic energy flux with total integrated radiative losses is studied. The comparisons are made in the middle and upper chromosphere of the quiet Sun and weak plage regions located in the central zone of solar disc. The spectral lines Hα, Hβ, Ca II 854.2 nm and Mg II k&h provide information about different ranges of heights in the chromosphere according to their effective formation heights in quiet and active areas (see Section 3.5). For the middle chromosphere, two different ranges are used, 900–1500 km in the IBIS data set and 1000–1400 km in the BBSO data set. At a short notice, in IBIS ROI the models are derived from VAL B, where the formation heights are lower compared to VAL C, which is used in BBSO ROI. In the same manner, in the upper chromosphere the ranges are set to 1400–1800 km in BBSO and 1600–1900 km in VTT data sets. The deposited acoustic fluxes $\Delta F_{\rm ac}$ and the total radiative losses L are computed for those height ranges.

In IRIS observations, 23 different data sets including 12 quiet-Sun and 11 active regions are utilized to compare $\Delta F_{\rm ac}$ and L in the middle and upper chromosphere. The quiet-Sun atmospheres were represented by scaled initial VAL C and D models, providing the best match of synthetic to local-time averaged observed profiles. In the case of active-region atmospheres, best-matching models from the grids of scaled initial VAL E and F models were selected. The most important ingredients for $\Delta F_{\rm ac}$ calculation are the Doppler velocity power spectra, gas density and pressure at the lower-boundary (the half-maximum intensity of the emission core of the Mg II k&h lines) and upper-boundary (effective formation heights of the central reversal of the Mg II k&h lines) heights, and the magnetic-field inclination.

7.1 IBIS data set - quiet and weak active regions

The initial semi-empirical models, VAL B–F, were assigned to all pixels within the ROI in accordance with the brightness of the Ca II 854.2 nm line core (Figure 7.1 (a) and (b)). A scaled model from the grid (see Section 2.5.1) was selected using the best match of the synthetic $I_{\rm syn}$ to the local time-averaged observed profile $I_{\rm obs}$ of the line. The best match means that the sum of squared differences between the synthetic and observed profiles is at minimum. In total, 1737 differ-

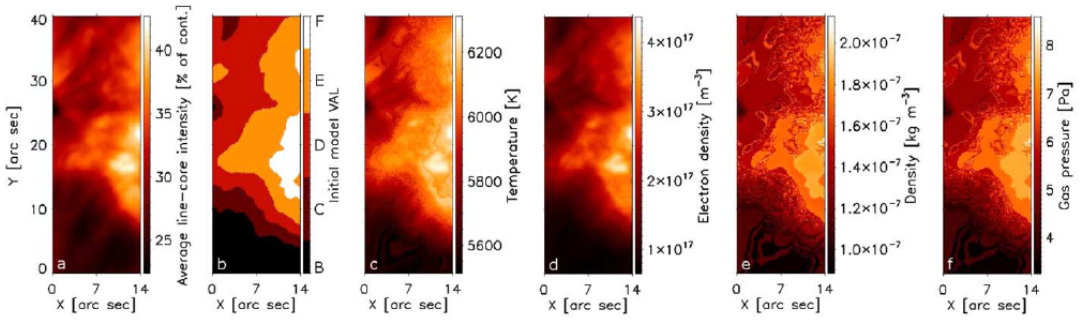

Figure 7.1: Maps of (*a*) Ca II 854.2 nm line-core intensity, (*b*) selection of initial models, (*c*) temperature, (*d*) electron density, (*e*) density, and (*f*) gas pressure. The maps (c)–(f) are retrieved from resulting scaled models at z=900 km.

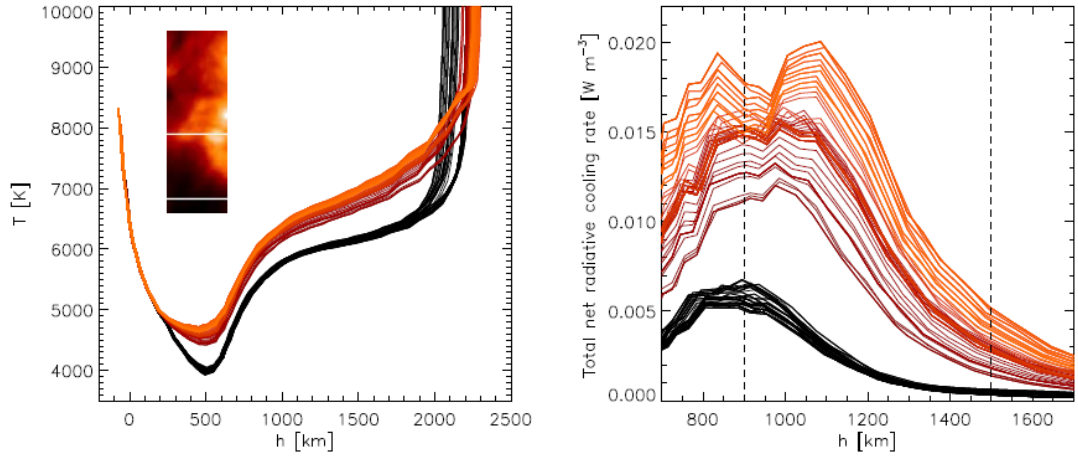

Figure 7.2: *Left*: examples of quiet-Sun temperature stratifications with height (black) at positions along the bottom white line in the inset image of the line-core intensity. Red-to-orange temperature curves correspond to positions from left to right along the top white line that crosses the plage. *Right*: total net radiative cooling rates vs. height in quiet Sun (black) and plage (red–orange) at the same positions. Vertical dashed lines delimit the integration range.

ent models were used in the ROI. The retrieved values of model T, n_e, ρ, and P_g at the geometrical height z=900 km are shown in Figure 7.1(c)–(f).

Because each position in the ROI is characterized by a 1D model unrelated to its surroundings, the maps of ρ and P_g have a noisy appearance. However, the local differences are small — for example, the standard deviation of gas pressure in the "noisy" subfield $6'' < x < 11''$, $30'' < y < 40''$ is 0.5 Pa (9 % of the mean value). In Figure 7.2, typical temperature stratifications of quiet Sun and plage are depicted by two horizontal white lines. Their positions are showed in the inset image of the Ca II 854.2 nm line-core intensity: the quiet-Sun temperatures (black curves) correspond to the bottom white line, while those in the plage are taken along the top white line, and the colors of the temperature curves change from dark red to orange moving from left to right.

The total net radiative cooling rates are calculated for each model in the ROI and integrated over the height range 900—1500 km. The right panel of Figure 7.2

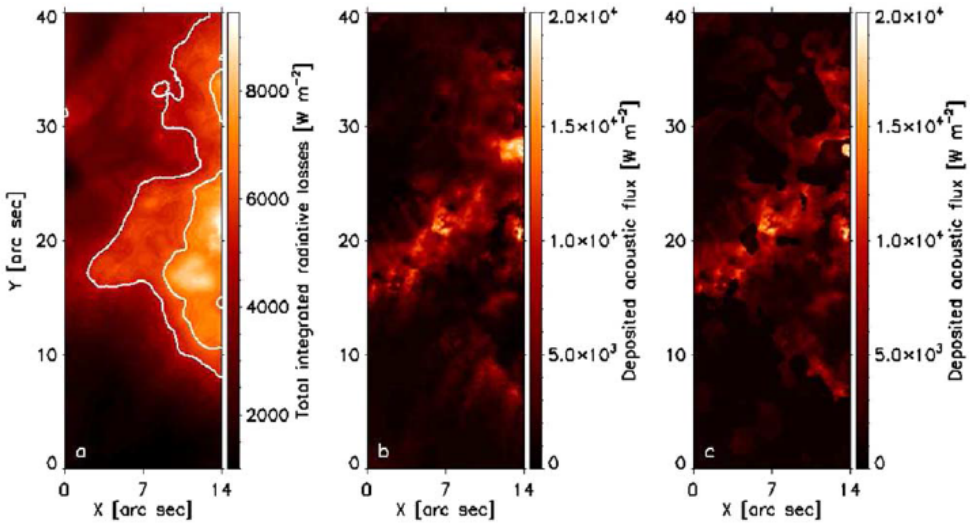

Figure 7.3: (*a*) Total integrated radiative losses map with contours of 5000 and 6500 W m^{-2}. The deposited acoustic-flux maps are calculated using (*b*) the original magnetic inclination angles and (*c*) the corrected ones.

shows examples of the height dependence of cooling rates in the quiet Sun and plage at the same positions as the temperature stratifications. In the plage, the total cooling rates have a maximum at z=1000–1100 km, which corresponds to maximum cooling rates of Ca II (the Mg II contribution is by an order lower). A secondary peak, caused by enhanced contribution of H and H$^-$ continua in hot and dense atmospheres, appears around z=800 km in the brightest part of the plage (orange curves). It does not enter our integration range. The map of the total integrated radiative losses is displayed in 7.3.

We calculate the deposited acoustic fluxes (see Chapter 6) using two different sets of magnetic-field inclinations to estimate the influence of uncertainties in the inclination angle: (1) original inclination angles retrieved from the inversion, including the unreliable values near 90° in weak-field or nonmagnetic regions. The resulting map of the deposited acoustic flux is shown in Figure 7.3(b). (2) Corrected inclination angles, where the unreliable values are set to zero by means of the mask described in Section 4.2.2. The corresponding deposited acoustic-flux map is shown in Figure 7.3(c). The coefficient of spatial correlation between the total integrated radiative losses and the deposited acoustic flux is 0.47 in the case of (1) and 0.50 in the case of (2).

Scatter plots of total integrated radiative losses L versus the acoustic energy flux $\Delta F_{\rm ac}$ deposited in the chromosphere between z=900–1500 km are shown in Figure 7.4(a) and (b) for the original inclination angles and the corrected ones, respectively. The red solid line represents mean values of $\Delta F_{\rm ac}$ that fall into 200 W m^{-2} wide bins of the L histogram. The bins must contain at least 100 points to calculate the mean value. Likewise, the green line represents median values. The red dashed lines delimit the $\pm 1\sigma$ range that characterizes the scatter of individual points in each bin. When the unreliable horizontal magnetic inclination is included (Figure 7.4(a)), the deposited acoustic fluxes in the quiet-Sun area (L< 5000 W m^{-2}) almost double those calculated using the corrected inclination values (Figure 7.4(b)). This is not realistic because of too many points

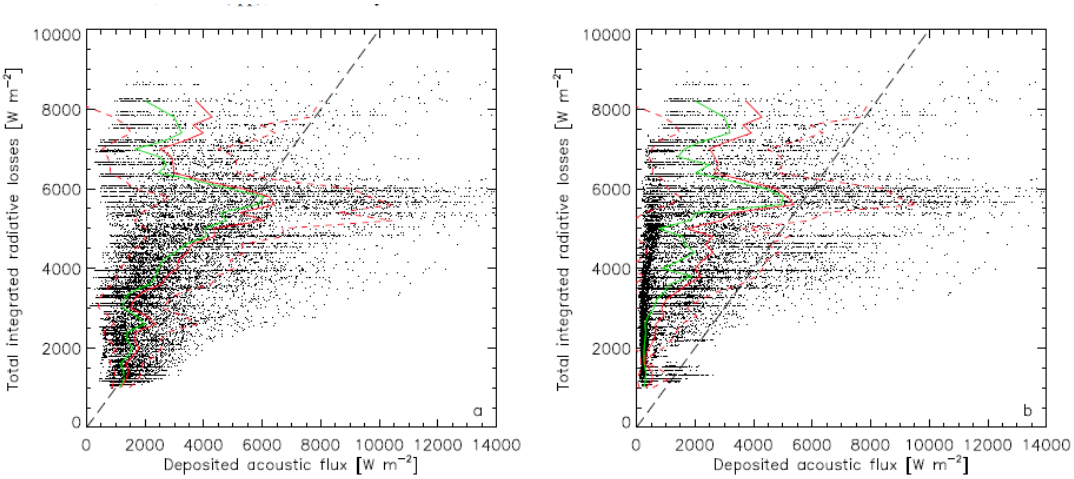

Figure 7.4: Scatter plots of total integrated radiative losses vs. deposited acoustic flux in the IBIS ROI. The acoustic fluxes are calculated using (*a*) the original magnetic inclination angles and (*b*) the corrected ones. Solid lines show average (red) and median (green) values together with red dashed lines of $\pm 1\sigma$. The straight dashed line represents the full balance of radiative losses by acoustic-flux deposit.

where $\Delta F_{\rm ac} > L$. The increase of $\Delta F_{\rm ac}$ is much smaller in the plage, where the magnetic inclination is determined reliably. In the further discussion, we shall use the deposited acoustic fluxes calculated using the corrected inclination angles.

For most of the points (88 %) in the plot (Figure 7.4(b)), $\Delta F_{\rm ac} < L$ that is, the deposited acoustic flux is insufficient to balance the radiative losses and maintain the semi-empirical temperature at corresponding positions in the ROI. The scatter of $\Delta F_{\rm ac}$ versus L is large, so that we have to express the contribution of the deposited acoustic flux to the radiative losses statistically, using the ratios $\overline{\Delta F_{\rm ac}}/L$ and median$(\Delta F_{\rm ac})/L$. Their values start at 0.3 (median 0.2) for $L < 3500$ W m^{-2} and increase to 0.5 (median 0.3) for $3500 < L < 5000$ W m^{-2} in the quiet area. They reach 0.7 (median 0.6) with a peak of 0.9 for $5000 < L < 6500$ W m^{-2} at the periphery of the plage, where the magnetic inclination is large, and drop to 0.5 (median 0.4) for $L > 6500$ W m^{-2} in the brightest part of the plage with the nearly vertical magnetic field.

The fit quality $\chi^2_{\rm min}$ changes with the position in the ROI. We define the bad-fit areas as where $\chi^2_{\rm min}$ is larger than 2σ of its statistical distribution. Several of them, where the observed profiles are broader than the synthetic ones, coincide with regions of enhanced magnetic field in the pore and plage. Contours that outline the bad-fit areas together with the map of magnetic-field strength are shown in Figure 7.5(a). The Zeeman broadening of the Ca II line with Landé factor g=1.1 probably does not play a major role. Rather, this effect might be explained by the fact that our 1D semi-empirical models do not account for the complex 3D distribution of thermodynamic and magnetic parameters in such areas. The bad-fit areas represent 12.5 % of the data set and a mask is made to remove the affected points from the scatter plot of L versus $\Delta F_{\rm ac}$. This removal alters the plot shown in Figure 7.4(b) and the derived statistical values only in the part of $L > 6500$ W m^{-2}, corresponding to the brightest plage region, where

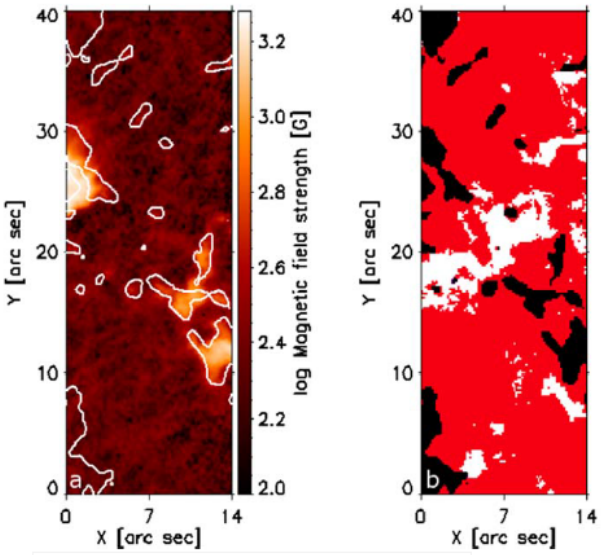

Figure 7.5: (*a*) Map of magnetic-field strength (in logarithmic scale) with contours of areas where the fit of synthetic to observed Ca II line profiles is worse than 2σ. (*b*) Areas of radiative losses smaller than the deposited acoustic flux (white) together with the bad-fit areas (black).

$\overline{\Delta F_{\rm ac}}$ becomes larger by the factor of 1.3 on average and its contribution to the total integrated radiative losses $\overline{\Delta F_{\rm ac}}/\ \overline{L}$ increases from 0.5 to 0.6.

In 12 % of the points of our data set, the deposited acoustic energy flux is larger than the total integrated radiative losses ($\Delta F_{\rm ac} > L$). Regions formed by these points are shown in Figure 7.5(b) together with the bad-fit ones in white and black colors, respectively. The $\Delta F_{\rm ac} > L$ regions appear at locations where the magnetic inclination is larger than 60° and temporal variations of Doppler velocity and intensity of the Ca II 854.2 nm core are strong, i.e., around the border between the pore's superpenumbra and plage (subfield $0'' < x < 10''$, $15'' < y < 25''$) and partly at the periphery of the plage.

Compared to the results of Sobotka et al. (2016), the median values of $\Delta F_{\rm ac}$ are consistent except the brightest parts of the plage ($L > 6500$ W m^{-2}), where the magnetic inclination was overestimated. Moreover, the revision of the magnetic inclination map resulted in an increase of $\Delta F_{\rm ac}$ at the plage periphery ($L \simeq$ 6500 W m^{-2}). Other differences can be explained by improved values of the gas density, to which the acoustic fluxes are directly proportional. The present set of 1737 atmospheric models provides a more realistic density distribution than the simple grid of only seven models.

We have shown that the deposited acoustic-flux energy in the middle chromosphere of quiet Sun balances 30 %–50 % of the energy released by radiative losses. The energy carried by (magneto)acoustic waves in the plage supplies 50 %–60 % of the radiated energy at locations with a vertical magnetic field and 70 %–90 % in regions where the magnetic field is inclined more than 50°. These values are statistical averages of results with a large individual scatter and they are based on one observation of a single small solar area. They are also critically sensitive to the correct determination of the magnetic-field inclination, particularly in the quiet-Sun region. We also have to note that the area considered as quiet Sun in

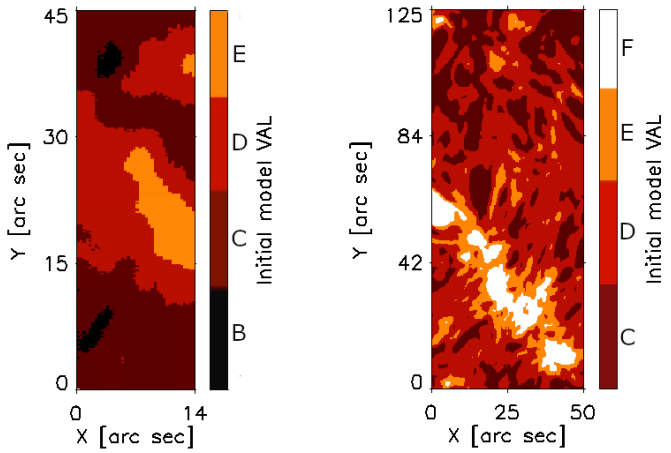

Figure 7.6: VTT data: initial models for December 11 (*left*) and June 6 (*right*).

the IBIS ROI is close to the plage and it falls within the extended canopy region of the plage's magnetic field. The effect of "magnetic shadows", which are related to the elevated magnetic field forming the Ca II fibrils (Vecchio et al., 2007; Kontogiannis et al., 2010), reduces the oscillatory power in this region. Consequently, the deposited acoustic flux in this quiet-Sun area may be lower than that in quiet regions far from the plage.

7.2 VTT data sets - quiet and weak active regions

In two observational campaigns, we observed two weak active regions including plages and small pores on 2018 December 11 and 2019 June 6 with the VTT echelle spectrograph in the hydrogen lines Hα and Hβ (see Section 4.1.2). Moreover, the Doppler velocities observed in the line center of Hα (reference height z_2=1900 km in active regions, see Section 3.5) and at the distance $\Delta\lambda = \pm 18$ pm from the line center of Hβ (reference height z_1=1600 km) are used to calculate acoustic energy fluxes (Chapter 6). The most favourable selections of initial models for the ROIs of the December and June data sets are VAL B–E and VAL C–F, describing the ROIs by 482 and 657 different scaled models, respectively. Figure 7.6 shows this selection for the December and June data sets.

The values of gas pressure P_{g} and density ρ are taken in each pixel of the ROIs from the corresponding scaled model atmosphere at two reference heights z_1 and z_2. The deposited acoustic flux ΔF_{ac}, i.e.,the difference between the incoming acoustic energy flux at the lower reference height z_1 and the outgoing one at the upper reference height z_2, is calculated as well. The summary of the first three quantities is listed in Table 7.1, where the velocity magnitudes are represented by the rms Doppler velocity, the gas densities and pressures by their mean values and standard deviations obtained by averaging over the corresponding ROIs.

The amplitudes of Hβ velocities are quite small in comparison with Hα. This implies that the mean incoming acoustic flux $\langle F_{\mathrm{ac,tot}}(1600\,\mathrm{km})\rangle$ is very small, be-

Table 7.1: Reference heights $z_{\rm ref}$, rms Doppler velocities σ_v, mean densities $\langle\rho\rangle$, and mean gas pressures $\langle P_{\rm g}\rangle$ at the reference heights.

Data set	$z_{\rm ref}$ [km]	σ_v [km s^{-1}]	$\langle\rho\rangle$ [kg m^{-3}]	$\langle P_{\rm g}\rangle$ [Pa]
Dec 11	1600	0.83	$(2.96 \pm 1.57) \times 10^{-9}$	0.158 ± 0.086
	1900	1.11	$(6.27 \pm 4.01) \times 10^{-10}$	0.070 ± 0.028
Jun 6	1600	0.79	$(3.18 \pm 1.32) \times 10^{-9}$	0.173 ± 0.070
	1900	1.64	$(6.13 \pm 3.87) \times 10^{-10}$	0.087 ± 0.023

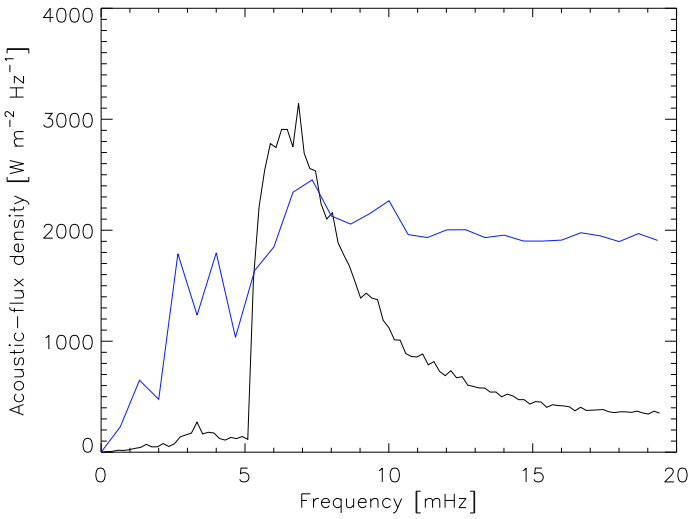

Figure 7.7: Frequency distribution of the incoming acoustic-flux density at $z_1 = 1600$ km averaged over the whole ROIs (magnetic plus non-magnetic areas) of December 11 (*blue*) and June 6 (*black*).

ing equal to 40 and 15 W m^{-2} for the December and June data sets, respectively. The difference between two data sets can be explained by different frequency distributions plotted in Figure 7.7. The December data show a significant contribution at frequencies in the ranges 1–5 mHz (thanks to the large fraction of magnetised area) and 8–20 mHz, induced probably by seeing, which was not sufficiently good during the observation.

The deposited acoustic fluxes $\Delta F_{\rm ac}$ and total integrated radiative losses L are computed and integrated for the range $z = 1600$–1900 km in the upper chromosphere. The maps of $\Delta F_{\rm ac}$ and L for both ROIs are displayed in Figure 7.8. Enhanced radiative losses of the order 10^4 W m^{-2} are observed in the central part of the plage on June 6. This area is characterized by hot atmospheric models, obtained by scaling the initial model VAL F (see Figure 7.6), for which a strong contribution of hydrogen Lyman-α to L at $z > 1800$ km becomes important.

In Figure 7.9, typical temperature stratifications of quiet Sun and plage are depicted by two horizontal white lines. Their positions are showed in the inset image of the Hα line-core intensity: the quiet-Sun temperatures (black curves) correspond to the top white line, while those in the plage are taken along the bottom white line, and the colors of the temperature curves change from dark red to orange moving from left to right. The total net radiative cooling rates are calculated for each model in the ROI and integrated over the reference-height

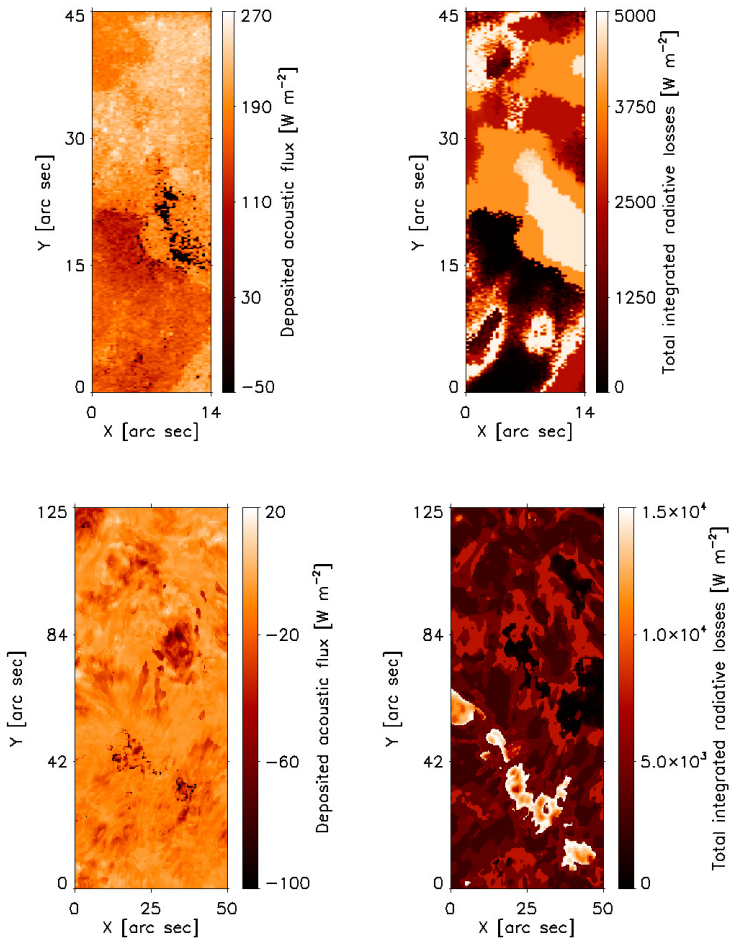

Figure 7.8: The deposited acoustic energy flux (*left*) and the total integrated radiative losses (*right*) for the range z=1600–1900 km (upper chromosphere) in the ROIs of December 11 (*top*) and June 6 (*bottom*).

range 1600–1900 km. The right panel of Figure 7.9 shows examples of the height dependence of cooling rates in the quiet Sun and plage at the same positions as the temperature stratifications. Figure 7.10 additionally displays the height dependence of cooling rates for the main contributors: hydrogen, Ca II, and Mg II.

Figure 7.11 shows the scatter and density plots comparing ΔF_{ac} and L for both ROIs. The mean, median, and standard deviation of the deposited acoustic flux are calculated in the same way as in Section 7.1. For all plotted points, the deposited acoustic flux is mostly in the range from $-50\,\mathrm{W\,m^{-2}}$ to $150\,\mathrm{W\,m^{-2}}$ and it is very small compared to the radiative losses. Its mean values are approximately 30 $\mathrm{W\,m^{-2}}$ for the December 11 data set and zero for the June 6 one. The small positive mean value of the December flux is a consequence of the high-frequency contribution induced probably by the seeing. In the density plots (Figure 7.11 *right*), pixels of magnetic and non-magnetic areas are separated and their densities are normalized to the common histogram maximum of the two areas. The bin size of the 2D histogram is 30 $\mathrm{W\,m^{-2}} \times 30$ $\mathrm{W\,m^{-2}}$. Contours are plotted at four density levels with a step of one order of magnitude, beginning at 0.03 % of the maximum. The magnetic areas of the December and June data sets include 33.0 % and 3.9 % of pixels in the ROIs, respectively.

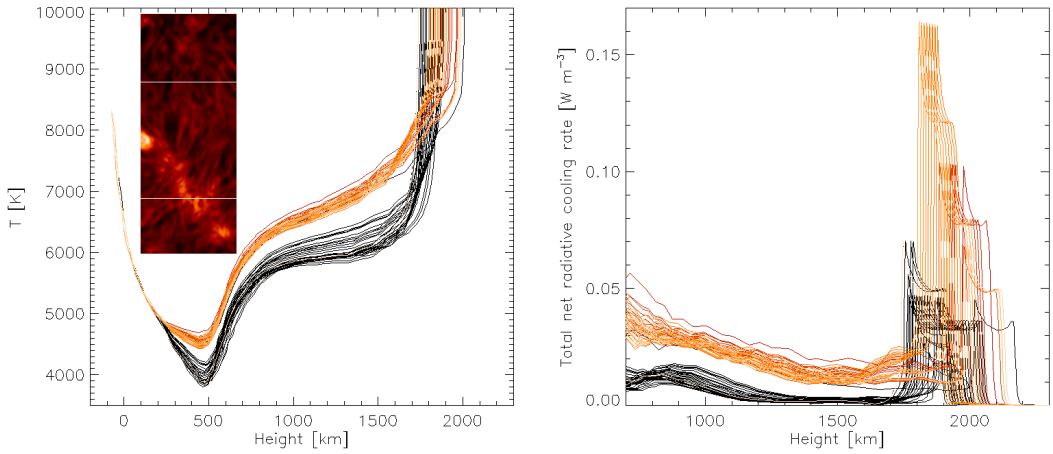

Figure 7.9: *Left*: examples of quiet-Sun temperature stratifications with height (black) at positions along the top white line in the inset image of the line-core intensity. Red-to-orange temperature curves correspond to positions from left to right along the bottom white line that crosses the plage. *Right*: total net radiative cooling rates vs. height in quiet Sun (black) and plage (red–orange) at the same positions.

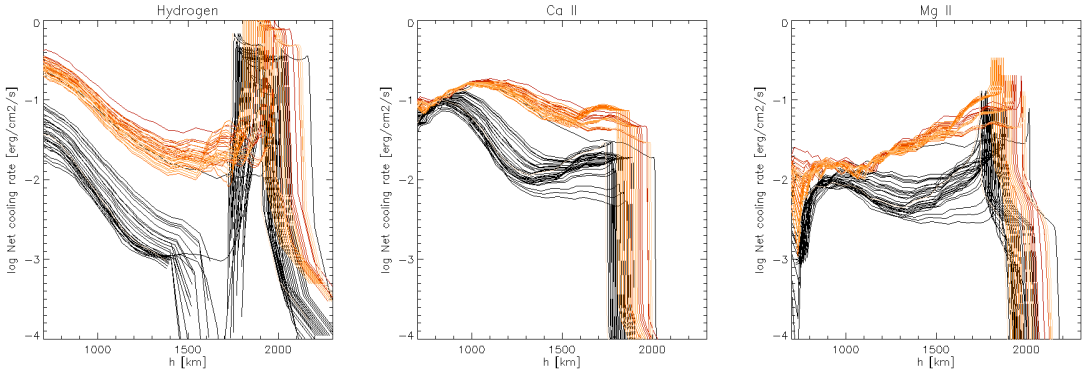

Figure 7.10: Radiative cooling rates vs. height in quiet Sun (black) and plage (red–orange) at the same positions for the main contributors, hydrogen (*left*), Ca II (*middle*) and Mg II (*right*).

A co-temporal measurement of the magnetic-field vector obtained with GRIS at the GREGOR telescope (Section 4.2.2) was used alternatively to re-compute the deposited acoustic fluxes of the December 11 data set. Because the spatial resolution of the GRIS magnetic-inclination map was by a factor of two better than that of HMI, the scatter of $\Delta F_{\rm ac}$ values was reduced but the mean and median values did not change.

Thus, the contribution of the deposited acoustic flux to the radiative losses is practically zero in the layer between $z = 1600$–1900 km. This confirms that $\Delta F_{\rm ac}$ cannot balance L in the upper chromosphere. We expect that the scatter of deposited acoustic-flux values around zero in the December and June data sets is caused by a limited accuracy in the determination of incoming and outgoing acoustic fluxes. The fact that Doppler velocities are sometimes measured at

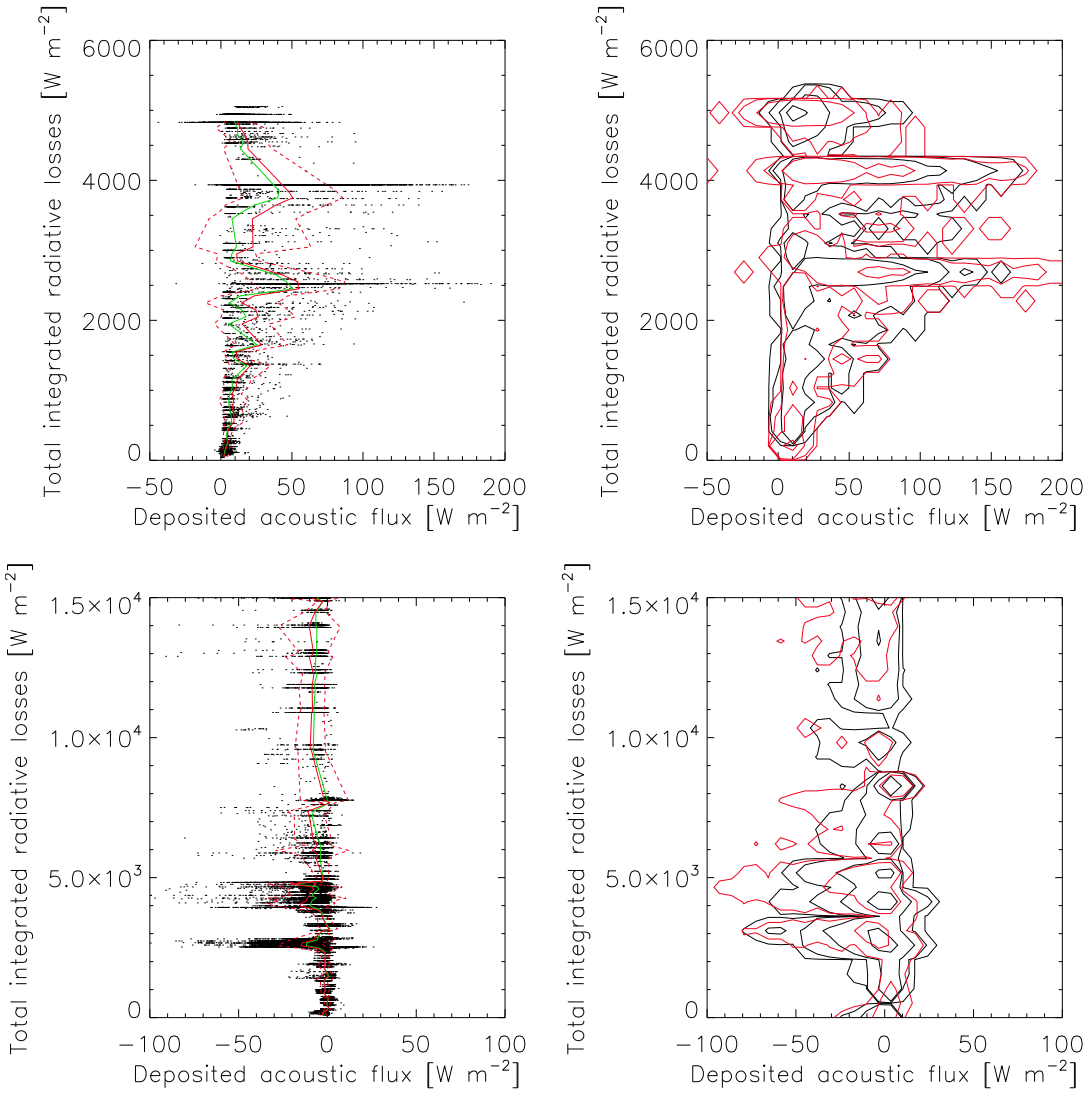

Figure 7.11: *Left*: Scatter plots of total integrated radiative losses versus deposited acoustic flux for the range z=1600–1900 km in the ROIs of December 11 (*top*) and June 6 (*bottom*). Solid lines show average (red) and median (green) values together with red dashed lines of $\pm 1\sigma$. *Right*: Density contours of the scatter plots. Contours for magnetic (red) and non-magnetic (black) areas are plotted separately at density levels of 0.03, 0.3, 3, and 30 % of a common density maximum.

heights different from the reference ones (Section 3.5), introduces the relative error of 15 % in both quantities. As a further matter, when the inner wings of Hβ are affected by a photospheric contribution, the error of the incoming acoustic flux increases to 30 %.

7.3 BBSO data set - quiet Sun

The data set obtained on 2019 October 3 with the GST/FISS instrument includes a quiet-Sun region at the center of the solar disc. The lines Ca II 854.2 nm and Hα provide the information about two different ranges of heights, 1000–1400 km

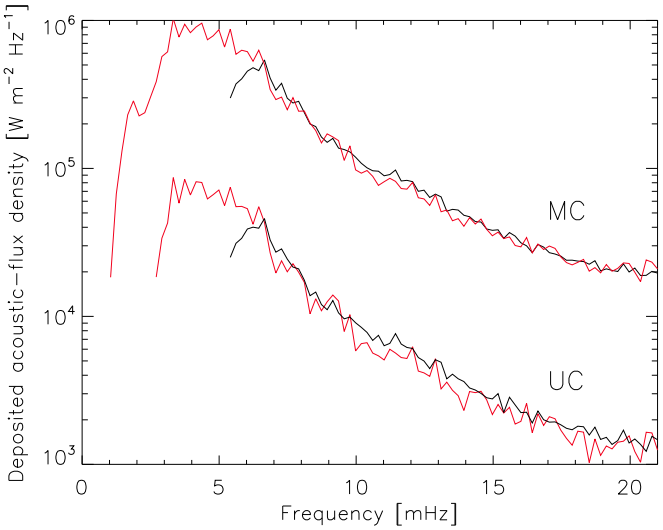

Figure 7.12: Frequency distribution of the deposited acoustic-flux density averaged over magnetic (red) and non-magnetic (black) areas of the BBSO data set. MC and UC lines correspond to the height ranges 1000–1400 km (middle chromosphere) and 1400–1800 km (upper chromosphere), respectively.

(middle chromosphere) and 1400–1800 km (upper chromosphere), because in the quiet-Sun atmosphere, the reference heights for the Ca II wing, Ca II center, and Hα center are 1000, 1400, and 1800 km, respectively – see Section 3.5. The deposited acoustic fluxes $\Delta F_{\rm ac}$ and the total integrated radiative losses L are computed for those height ranges. The best initial model for the BBSO data set was VAL C and the ROI was covered by 59 different optimal scaled models.

The frequency distribution of the deposited acoustic-flux density spatially averaged over the magnetic ($|B| > 125$ G, 11.6 % of ROI) and non-magnetic ($|B| < 125$ G, magnetic inclination set to zero, 88.4 % of ROI) areas is displayed in Figure 7.12 for the two height ranges. The maximum contribution in non-magnetic areas is at 6–7 mHz and for frequencies higher than 14 mHz, the contribution is by an order of magnitude smaller than the maximum one. The presence of inclined magnetic fields adds a substantial contribution at frequencies below 5.2 mHz, increasing the total deposited acoustic fluxes in the middle and upper chromosphere by a factor of 2.3.

The maps of the deposited acoustic flux and total integrated radiative losses are displayed in Figure 7.13. The scatter and density (2D histogram) plots of the $\Delta F_{\rm ac}$ to L pixel-by-pixel comparison are shown in Figure 7.14. The spatial distribution of $\Delta F_{\rm ac}$ is strongly intermittent, as already noted by Bello González et al. (2010b), and we observe a large scatter of $\Delta F_{\rm ac}$ versus L. For this reason, we have to analyze the contribution of the deposited acoustic flux to radiative losses statistically, using the mean, median, and standard deviation of $\Delta F_{\rm ac}$. These statistical values are calculated in 100 W m^{-2} wide bins of the L histogram and each bin must contain at least 50 points.

In Figure 7.14 *left*, the red and green solid lines represent the bin-averaged $\overline{\Delta F_{\rm ac}}$ and median values, respectively, and the red dashed lines set the boundaries of the $\pm 1\sigma$ range that characterize the scatter of individual points in each bin.

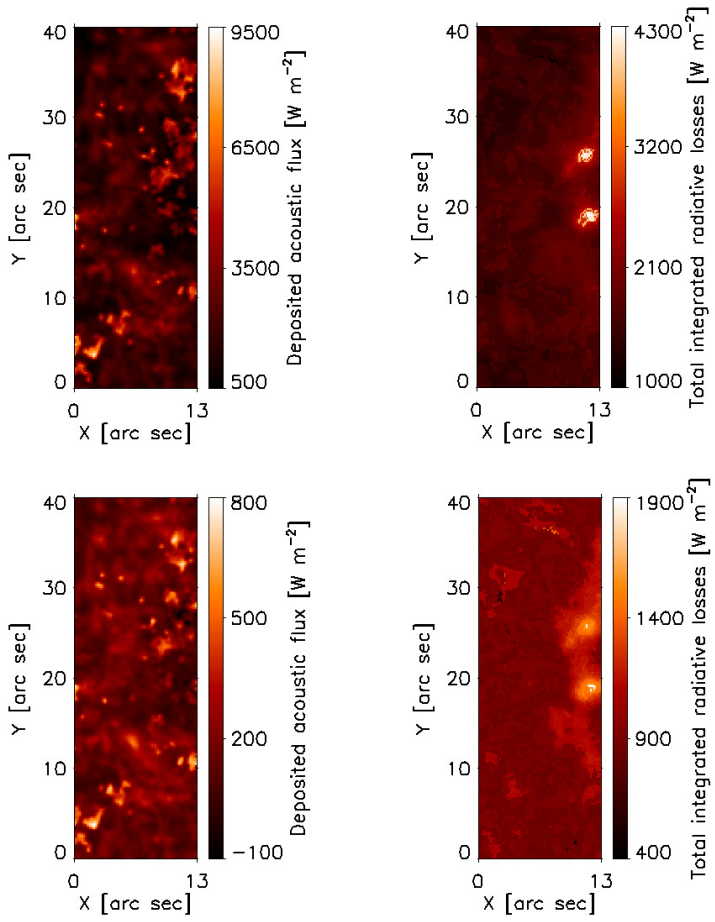

Figure 7.13: The deposited acoustic energy flux (*left*) and the total integrated radiative losses (*right*) in the ROI of the BBSO data set. *Top*: $z = 1000$–1400 km (middle chromosphere), *bottom*: $z = 1400$–1800 km (upper chromosphere).

In the density plots (Figure 7.14 *right*), pixels of magnetic and non-magnetic areas are separated and their densities are normalized to the common histogram maximum of the two areas. The bin size of the 2D histogram is 30 W m^{-2} × 30 W m^{-2}. Contours are plotted at four density levels with a step of one order of magnitude, beginning at 0.03 % of the maximum.

In the middle chromosphere, the total radiative losses integrated over the 400 km thick layer are $1000 < L < 2600$ W m^{-2} in the quiet area and reach 4300 W m^{-2} in two bright points connected with magnetic elements (bottom panels in Figure 7.14 and right panels in Figure 7.13). The ratio of the mean deposited acoustic flux to the radiative losses $\overline{\Delta F_{\rm ac}}/L$ is between 0.9 and 1.3 in the quiet area, so that the acoustic energy flux balances the energy released by radiation (top panels in Figure 7.14). However, the contribution of $\overline{\Delta F_{\rm ac}}$ to L in the two bright points is only 60 %.

In the upper chromosphere at the heights 1400–1800 km, the radiative losses ($400 < L < 1900$ W m^{-2}) are larger than the deposited acoustic flux for all the points in the scatter plot (bottom panels in Figure 7.14) and $\overline{\Delta F_{\rm ac}}/L \simeq 0.2$. This means that the deposited acoustic flux is insufficient to balance the radiative losses and maintain the semi-empirical temperature at these heights. Negative

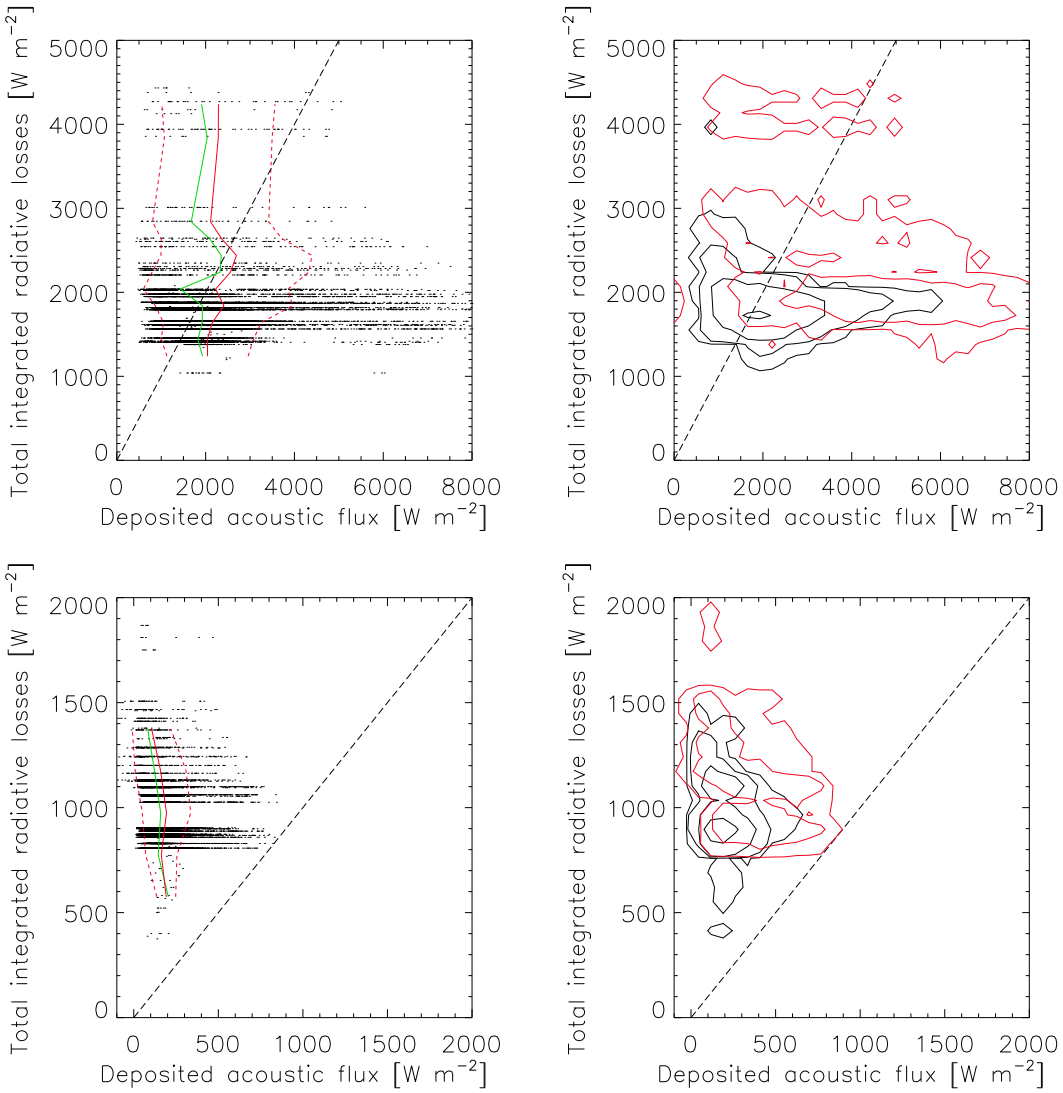

Figure 7.14: *Left*: Scatter plots of total integrated radiative losses versus deposited acoustic flux in the ROI of the BBSO data set. *Top*: $z = 1000$–1400 km, *bottom*: $z = 1400$–1800 km. Solid lines show average (red) and median (green) values together with red dashed lines of $\pm 1\sigma$. *Right*: Density contours of the scatter plots. Contours for magnetic (red) and non-magnetic (black) areas are plotted separately at density levels of 0.03, 0.3, 3, and 30 % of a common density maximum. Straight dashed lines represent the full balance of radiative losses by acoustic-flux deposit.

values of $\Delta F_{\rm ac}$ appearing at some scarce locations in the ROI are caused by the limited accuracy of our method (see Section 3.5).

To estimate the fraction of the incoming acoustic energy flux $F_{z_1} = F_{\rm ac,tot}(z_1)$ deposited in a layer between the reference heights z_1 and z_2, we use the spatially-averaged values $\langle F_{z_1} \rangle$ and $\langle \Delta F_{\rm ac} \rangle$ in the magnetic and non-magnetic areas in the ROI. The results are shown in Table 7.2 together with the corresponding spatially averaged values $\langle L \rangle$ of the total integrated radiative losses and the ratio $\langle \Delta F_{\rm ac} \rangle / \langle L \rangle$. Standard deviations characterize a large scatter of values corresponding to individual pixels in these areas. The incoming acoustic flux at

Table 7.2: BBSO data set: Spatial averages of incoming acoustic flux $\langle F_{z_1} \rangle$, its part $\langle \Delta F_{\rm ac} \rangle$ deposited between the reference heights z_1 and z_2, and corresponding radiative losses $\langle L \rangle$.

Quiet Sun	$z_1 - z_2$ [km]	$\langle F_{z_1} \rangle$ [W m^{-2}]	$\langle \Delta F_{\rm ac} \rangle$ [W m^{-2}]	$\langle \Delta F_{\rm ac} \rangle / \langle F_{z_1} \rangle$	$\langle L \rangle$ [W m^{-2}]	$\langle \Delta F_{\rm ac} \rangle / \langle L \rangle$
Magnetic,	1000–1400	4960 ± 2010	4440 ± 1814	0.90 ± 0.01	2087 ± 596	2.13 ± 1.43
11.6 % of ROI	1400–1800	520 ± 202	321 ± 191	0.62 ± 0.20	1057 ± 203	0.30 ± 0.24
Non-magnetic,	1000–1400	2085 ± 744	1871 ± 673	0.90 ± 0.01	1689 ± 180	1.11 ± 0.42
88.4 % of ROI	1400–1800	214 ± 74	147 ± 65	0.69 ± 0.10	888 ± 92	0.17 ± 0.08

1000 km is by a factor of 2.4 larger in the magnetic area than in the non-magnetic one. In both types of areas, 90 % of the incoming flux is deposited between the heights 1000–1400 km, which is sufficient to balance the radiative losses. A fraction of 0.6–0.7 of the remaining 10 % of the acoustic flux passing through the height of 1400 km is deposited below 1800 km, but its contribution to the radiative losses is small. Acoustic fluxes of 200 W m^{-2} in the magnetic area and 70 W m^{-2} in the non-magnetic one pass to layers above 1800 km.

7.4 IRIS data sets - quiet and active regions

We examined 23 IRIS data sets including 12 quiet-Sun and 11 active regions (see Section 4.4.2 and Table 4.4) to compare the deposited acoustic fluxes with radiative losses. First we present some typical examples and then results based on all the data sets together with an error estimate.

- **Cases of typical quiet and active regions**

  Relations between the acoustic fluxes and total integrated radiative losses are shown for two data sets typical for the quiet Sun (QS11) and active region (AR10) in Figure 7.15. The first row in the figure displays the effective formation heights and is identical with Figure 3.12. The second row shows the incoming acoustic fluxes $F_{\rm ac}(z_1)$ (black line) and the outgoing ones $F_{\rm ac}(z_2)$ (multiplied by ten, blue line) for each position along the slit. A fraction of the incoming energy flux is dissipated in the chromosphere between z_1 and z_2 and the rest continues to propagate higher in the atmosphere. The deposited acoustic energy fluxes $\Delta F_{\rm ac}$ (red) and the total integrated radiative losses L (black) are compared in the third row. Finally, scatter plots of L versus $\Delta F_{\rm ac}$ are displayed in the fourth row. Figure 7.16 shows another example of the quiet-Sun (QS3) and active region (AR2) data sets.
  In the quiet-Sun data set, the total radiative losses integrated over the 800–1300 km thick layers are in the range $1000 < L < 5500$ W m^{-2}, relating to the network and intranetwork structures. The ratio of the mean deposited acoustic flux to the radiative losses $\overline{\Delta F_{\rm ac}}/L$ is between 0.9 to 1.5, so that for most of the positions along the slit in the plot (Figure 7.15, third and fourth rows on the left), the deposited acoustic flux is sufficient to balance the radiative losses and maintain the observed chromospheric temperature at the corresponding positions. In this case, 98 % of the incoming acoustic

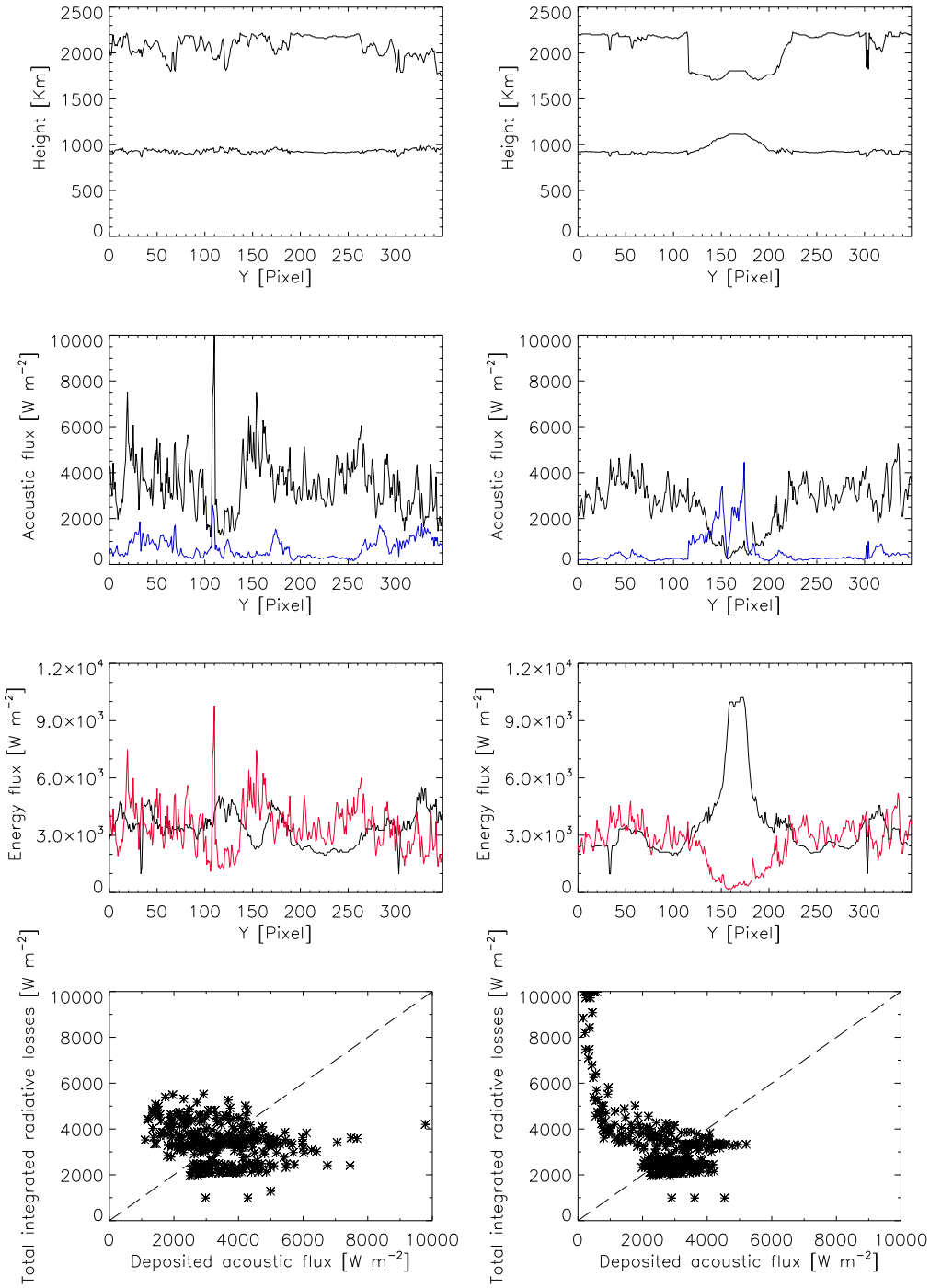

Figure 7.15: Lower and upper effective formation heights (*first row*), acoustic fluxes (*second row*), and energy fluxes (*third row*) along the slit in the typical quiet-Sun data set – QS11 (*left*) and active-region data set – AR10 (*right*). In the acoustic-flux plots, black lines correspond to incoming acoustic fluxes and blue ones to outgoing acoustic fluxes multiplied by 10. In the energy-flux plots, red lines correspond to deposited acoustic fluxes and black ones to total integrated radiative losses. Scatter plots of these quantities are in the *fourth row*. Straight dashed lines represent the full balance of radiative losses by acoustic-flux deposit.

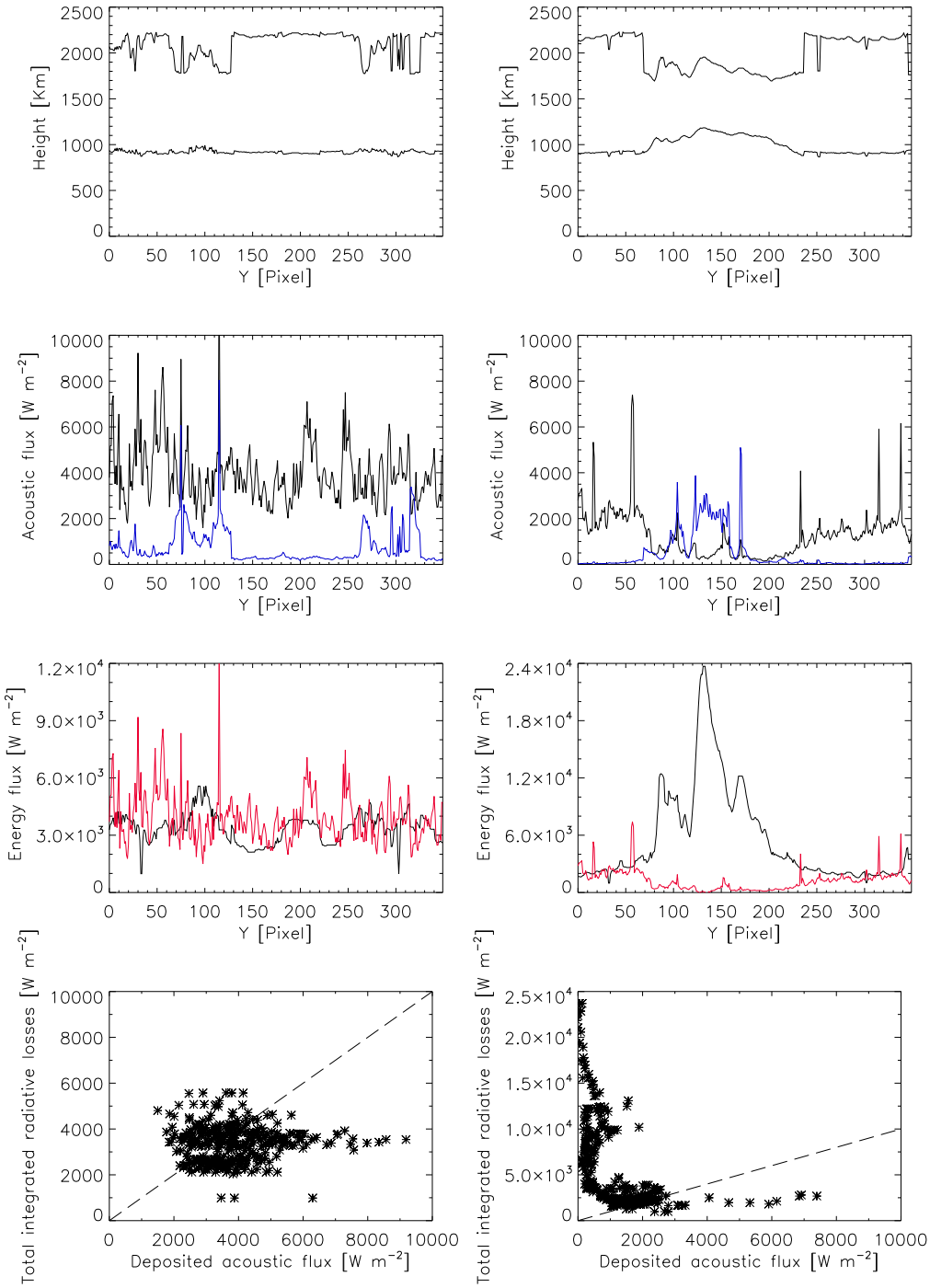

Figure 7.16: Same as in figure 7.15 for quiet-Sun data set – QS3 (*left*) and active-region data set – AR2 (*right*).

flux is absorbed in the considered layers and only about 70 W m^{-2} on average passes higher, to the transition region and corona.

In the active-region data set, the plots (Figure 7.15, third and fourth rows on the right) show that $L \gg \Delta F_{\rm ac}$ for pixels $140 < y < 200$, so that the energy deposited by (magneto)acoustic waves between the considered heights is very small and the ratio $\overline{\Delta F_{\rm ac}}/L$ is approximately 0.1–0.3. In this area, the integration is made over a 650 km thick layer in the central

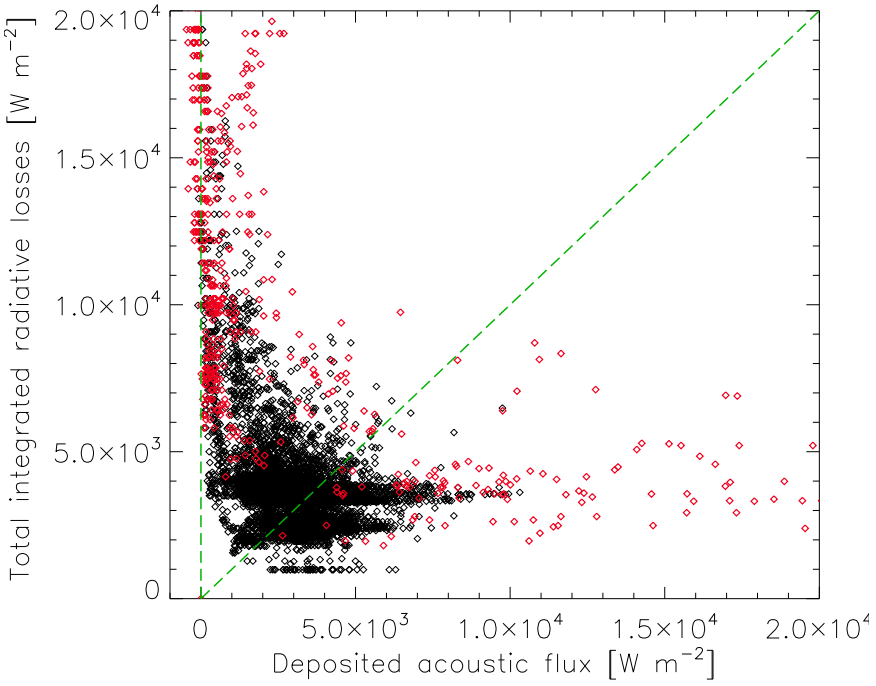

Figure 7.17: Scatter plot of total integrated radiative losses versus deposited acoustic flux at all positions of all data sets. Black and red diamonds correspond to non-magnetic and magnetic positions, respectively. Straight dashed lines represent the full balance of radiative losses by acoustic-flux deposit and zero deposited acoustic flux.

part of the plage, where $L > 4000$ W m^{-2}. The incoming acoustic flux is reduced here by a factor of 3.5, compared to the surrounding quiet area, and about 20 % of this flux passes the layer without being absorbed. The remaining pixels at $y < 140$ and $y > 200$, correspond to the quiet Sun and L is balanced by $\Delta F_{\rm ac}$ at these positions.

- **Comparison of deposited acoustic flux with radiative losses in all data sets**

  In total, 23 different data sets including 12 quiet-Sun and 11 active regions are utilized to compare $\Delta F_{\rm ac}$ and L in the middle and upper chromosphere. The quiet-Sun atmospheres were represented by scaled initial VAL C and D models, providing the best match of synthetic to local-time averaged observed profiles. In the case of active-region atmospheres, best-matching models from the grids of scaled initial VAL E and F models were selected. Figure 7.17 illustrates the scatter-plot comparison of $\Delta F_{\rm ac}$ and L for all positions along the slits in all data sets. Points located in non-magnetic regions (6337 in total) are distinguished from those (524) of magnetic regions with $|B| > 125$ G.
  Figure 7.17 shows that all the observed quiet and active regions behave similarly to the typical cases presented above. In quiet-Sun regions ($L <$ 5000 W m^{-2}), $\Delta F_{\rm ac}$ is statistically comparable with L, so that the energy

released by radiation can be balanced by the deposited acoustic-flux energy. Most of the incoming acoustic flux is absorbed in the studied layer and, on average, only 2 % of it pass to the transition region and corona.
In active regions ($L > 5000$ W m^{-2}), $\Delta F_{\rm ac}$ decreases with increasing L, supplying only 10–30 % of the radiated energy and even less, 5 %, for $L >$ 10000 W m^{-2}. This decrease is caused mainly by the observed reduction of incoming acoustic flux in active regions, probably due to the magnetic-canopy effect. Another reason is that 10–20 % of the incoming acoustic flux is not deposited in the layer and escapes higher into the atmosphere (cf. Section 6.2).
The uncertainty of obtained $\Delta F_{\rm ac}$ depends on several factors: the accuracy of the Doppler velocity measurement, correct assignment of the model atmosphere, and the accuracy of formation heights from which the density and gas pressure at the lower and upper boundaries are obtained. Therefore, we attempt to estimate this uncertainty directly from spatial fluctuation of $\Delta F_{\rm ac}$ values, assuming that they do not vary abruptly with position along the spectrograph slit at distances corresponding to the typical size of chromospheric features seen in the slit-jaw images, which is approximately 1.5″. We define the lower limit of the uncertainty as the standard deviation of differences between the original values of $\Delta F_{\rm ac}$ and those smoothed by a window of 1.5″ in width. The upper limit is estimated as the standard deviation of differences between $\Delta F_{\rm ac}$ at neighboring positions. From six quiet-Sun data sets with low magnetic signal (QS4, QS7, and QS9–12) we find that the lower and upper limits are 520 W m^{-2} and 640 W m^{-2} respectively, meaning that the uncertainty is approximately $\pm$600 W m^{-2}. The points with negative $\Delta F_{\rm ac}$ observed for $L >$ 12000 W m^{-2} (Figure 7.17) are inside this range of uncertainty. The points with $\Delta F_{\rm ac} >$ 8000 W m^{-2} seen in Fig. 7.17 originate in most cases from magnetic regions. Their outlying values stem from errors of measurements of the k&h emission-core Doppler velocity together with an enhancement of $\Delta F_{\rm ac}$ in strongly inclined magnetic fields.

Chapter 8

Summary and conclusions

We examined the heating of the solar chromosphere by dissipation of (magneto)acoustic waves through different layers of the solar chromosphere using the DST/IBIS, VTT/echelle spectrograph, GST/FISS, and IRIS spectroscopic multi-line observations in Hα, Hβ, Ca II 854.2 nm and Mg II k&h lines. The deposited acoustic energy fluxes were quantitatively compared with the total radiative losses in quiet-Sun and weak active regions in the central zone of the solar disc.

The deposited acoustic flux was derived from time series of Dopplergrams measured in the centers and wings of strong chromospheric lines (Chapter 4). We made use of 1D non-LTE hydrostatic semi-empirical models to calculate the radiative losses L, which were assigned to each pixel of each data set together with the deposited acoustic fluxes $\Delta F_{\rm ac}$. The models were selected from a grid obtained by scaling the temperature and column-mass stratifications of the initial VAL models (Section 2.5.1) to provide the best match of the synthetic to the observed time-averaged profiles (Section 3.4). We compared L and $\Delta F_{\rm ac}$ in the chromospheric layer delimited by the upper and lower boundaries (Chapter 7).

In the IRIS data sets, the Doppler velocities were measured in the central reversals and at the half-maximum intensity of the emission cores of the Mg II k&h lines. On average, the central reversals were formed at the heights of 2200 km in quiet regions and 1800 km in active regions, setting the upper boundary of the studied chromospheric layer. The lower boundary was defined by the average formation height of the emission cores, 900 km in quiet regions and 1100 km in active regions. The lower and upper boundaries delimited a broad layer that included the middle together with the upper chromosphere. Individual heights of these boundaries varied with the model atmosphere. The maximum detectable frequencies of velocity oscillations were in the range of 14–24 mHz. The average ratio $\Delta F_{\rm ac}/L$ was 0.9–1.5 in quiet and 0.1–0.3 in active regions.

The IBIS data set provided information about the middle chromosphere between fixed reference heights 900 and 1500 km. The Doppler velocities were measured in the inner wings and center of the line Ca II 854.2 nm and the maximum detectable frequency of oscillations was 9.6 mHz. The average ratio $\Delta F_{\rm ac}/L$ was 0.3–0.5 in quiet and 0.5–0.7 in active regions. The upper chromosphere between the reference heights of 1600 and 1900 km was studied using the VTT observations in the Hβ line wings and Hα center, with the maximum detectable frequency of 20 mHz. The average ratio $\Delta F_{\rm ac}/L$ was practically zero in quiet as well as active regions.

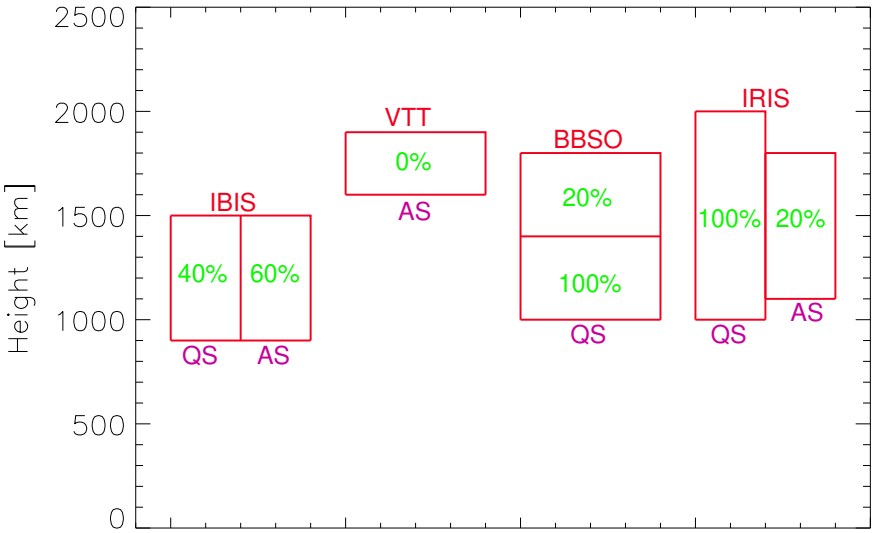

Figure 8.1: Average contributions of the deposited acoustic fluxes to radiative losses in quiet-Sun (QS) and active-Sun (AS) regions in different data sets used in this study.

The BBSO quiet-Sun data set included the lines Ca II 854.2 nm and Hα, so that it was possible to measure Doppler velocities at three reference heights, distinguishing between the middle and upper chromosphere. The reference heights were at 1000, 1400, and 1800 km, corresponding to Ca II wings, Ca II center, and Hα center, respectively. The maximum detectable frequency was 20 mHz. The average ratio $\Delta F_{\rm ac}/L$ was 0.9–1.3 in the middle and 0.2 in the upper chromosphere. Figure 8.1 shows the results of comparison of the deposited acoustic fluxes with radiative losses in different layers of the chromosphere in quiet-Sun (QS) and active-Sun (AS) regions of all data sets together with their average contributions $\Delta F_{\rm ac}/L$.

We also studied properties of observed waves using wavelet analysis of the IRIS Dopplergrams at the lower and upper boundaries. The wavelet coherence spectra provided phase shifts between the two boundaries. The average phase shifts for the non-magnetic and magnetic regions are positive (Fig. 6.3), so that the direction of propagation of the (magneto)acoustic waves is upward through the solar chromosphere. The phase speeds of the signals with frequencies larger than 2 mHz are supersonic. The increase of phase speed with frequency in non-magnetic regions is consistent with the presence of supersonic shocks. In magnetic regions, the phase speed is roughly constant in the frequency range 3–5 mHz, which is an indication of supersonic magnetoacoustic fast modes.

We have shown that the deposited acoustic flux can fully balance the radiative losses in the layers between 900 and 2200 km in *quiet-Sun regions* of the IRIS observations. A dissipation of supersonic shocks can be a major contributor to the radiative losses (Abbasvand et al., 2021). This result is in agreement with the results obtained from the BBSO and VTT data sets showing that the acoustic

flux deposited in the middle chromosphere (1000–1400 km) of a quiet region balanced completely the radiative losses and that its contribution in the upper chromosphere above 1400 km was very small (Abbasvand et al., 2020b).

We have to remark that these quiet-Sun regions were far from plages and their canopies formed by extended magnetic-field lines. Otherwise, the acoustic energy flux can be reduced by a factor of 2–3 in quiet regions that are close to plages or pores (IBIS data set, Abbasvand et al., 2020a) due to the presence of magnetic shadows (Vecchio et al., 2007; Kontogiannis et al., 2010). Thus, the effect of magnetic shadows, related to the elevated magnetic field of the canopy, reduced the oscillatory power and the deposited acoustic flux. The quiet-Sun region studied in the BBSO data set was far from any plage or pore, so that the propagation of waves in the chromosphere was less affected by canopy fields.

Active regions with a strong magnetic field show a small contribution of acoustic waves, where the acoustic-flux deposit balances only 10–30% of the radiative losses in the chromosphere between the heights of 1100 and 1800 km (IRIS data sets). The deposited acoustic-energy flux is small and decreases with increasing radiative losses. We may speculate about a reduction of the incoming acoustic flux by the presence of magnetic shadows and a different character of waves in magnetic regions, which do not dissipate so efficiently like the supersonic shocks. Definitely, the active-region chromosphere is heated by mechanisms different from the magnetoacoustic waves. This finding is consistent with the negligible contribution of magnetoacoustic waves to the heating of the upper chromosphere (1600–1900 km) in active regions (VTT data sets).

We have also shown that in the upper chromosphere, the incoming and deposited acoustic fluxes are very small compared to the radiative losses. In quiet-Sun region, the acoustic-flux deposit contributes only by about 20 % to the radiative losses between the heights 1400 km and 1800 km (BBSO data set) while in weak active regions (VTT data sets), its contribution is practically equal to zero in the height range 1600–1900 km.

This finding may be explained by the fact that the acoustic energy flux at a given height is proportional to the density of gas ρ, power density of Doppler velocities P_v, and the group velocity $v_{\rm gr}$ (Equation 6.6). Of these three quantities, the change of ρ with height is the most important one. Densities in the middle chromosphere are by an order of magnitude higher than those in the upper chromosphere, while $P_v \sim \sigma_v^2$ is approximately of the same order (see Table 7.1) and $v_{\rm gr}$ may change by a factor of 3 at maximum. Thus, it is mainly the density that determines the amounts of the incoming and deposited acoustic fluxes, which are considerable in the middle chromosphere but negligible in the upper layers.

The comparison of our results with the extensive literature on chromospheric heating by waves is not straightforward. Different methods with different assumptions were used to find the wave energy flux, giving different results. For example, Carlsson et al. (2007) applied numerical simulations to match observed broadband intensity fluctuations and concluded that the waves do not have enough energy to heat the quiet chromosphere. Bello González et al. (2009) and also our work utilized power spectra of Doppler velocity oscillations and found that the energy deposited by the waves is sufficient. In most of previous cases, the acoustic energy flux was determined in layers below the chromosphere. Our observations allow to calculate the acoustic energy deposited in the middle and upper chromosphere

between $z \simeq 900$ and 2000 km and compare it to radiative losses from this range of heights. We cannot include lower layers, but an important part of energy released by radiation comes also from the lower chromosphere, as seen in Figures 7.2 and 7.9. The most reliable comparison should cover all heights in the chromosphere, using 3D radiative transfer and time-dependent model atmospheres.

We would like to emphasize that our results are not inconsistent with the previous studies, where many (e.g., Fossum and Carlsson 2005; Beck et al. 2009, or see a thorough discussion in Section 4.1 of Jess et al. 2015) showed that the (magneto)acoustic waves are not sufficient to explain the heating of the chromosphere. In the present work we only studied two separate layers of the chromosphere available to us in our observations. We have no information about the relations between the deposited acoustic flux and radiative losses in the lower chromosphere. Thus, we do not attempt to draw any conclusions regarding the energy budget of the chromosphere as a whole. We point out that for some layers the heating by (magneto)acoustic waves may be sufficient, whereas in other layers it is insufficient. This fact itself draws a need for an additional source of energy. It is interesting to note that a similar conclusion was drawn by Fawzy et al. (2002) in the case of chromospheres of six late-type main-sequence stars, for which high-quality spectroscopic observations were available.

Although our stationary approach based on time-averaged acoustic fluxes and 1D hydrostatic semi-empirical models might not be fully realistic, it nevertheless opens up a possibility of a general estimate of the role of (magneto)acoustic waves in chromospheric heating by statistical comparison of the deposited acoustic fluxes to the radiative losses. Its results, namely (i) the ability of the quiet-region middle chromosphere to absorb sufficient acoustic-energy flux to maintain the temperature derived from semi-empirical models and (ii) the substantial reduction of incoming and deposited acoustic fluxes in magnetized active regions, may provide some hints to more realistic studies that use dynamic time-dependent models.

Bibliography

V. Abbasvand, M. Sobotka, P. Heinzel, M. Švanda, J. Jurčák, D. del Moro, and F. Berrilli. Chromospheric heating by acoustic waves compared to radiative cooling. II. revised grid of models. *ApJ*, 890(1):22, Feb 2020a. doi: 10.3847/1538-4357/ab665f.

V. Abbasvand, M. Sobotka, M. Švanda, P. Heinzel, M. García-Rivas, C. Denker, H. Balthasar, M. Verma, I. Kontogiannis, J. Koza, D. Korda, and C. Kuckein. Observational study of chromospheric heating by acoustic waves. *A&A*, 642: A52, Oct 2020b. doi: 10.1051/0004-6361/202038559.

V. Abbasvand, M. Sobotka, M. Švanda, P. Heinzel, W. Liu, and L. Mravcová. IRIS observations of chromospheric heating by acoustic waves in solar quiet and active regions. *A&A*, 648:A28, Apr 2021. doi: 10.1051/0004-6361/202140344.

M. J. Aschwanden. An evaluation of coronal heating models for active regions based on Yohkoh, SOHO, and TRACE observations. *ApJ*, 560(1):23, May 2001. doi: 10.1086/323064.

M. Asplund, N. Grevesse, A. J. Sauval, and P. Scott. The chemical composition of the Sun. *ARA&A*, 47(1):481–522, Sep 2009. doi: 10.1146/annurev.astro.46.060407.145222.

E. H. Avrett. The calculation of theoretical chromospheric models and the interpretation of solar spectra from rockets and spacecraft. Smithsonian Astrophysical Observatory Report, Jan 1985.

E. H. Avrett and R. Loeser. Models of the solar chromosphere and transition region from SUMER and HRTS observations: formation of the extreme-ultraviolet spectrum of hydrogen, carbon, and oxygen. *ApJS*, 175(1):229–276, Mar 2008. doi: 10.1086/523671.

C. Beck, E. Khomenko, R. Rezaei, and M. Collados. The energy of waves in the photosphere and lower chromosphere. I. Velocity statistics. *A&A*, 507(1): 453–467, Nov 2009. doi: 10.1051/0004-6361/200911851.

J. M. Beckers. Solar spicules. *ARA&A*, 10(1):73–100, 1972.

N. Bello González, M. Flores Soriano, F. Kneer, and O. Okunev. Acoustic waves in the solar atmosphere at high spatial resolution. *A&A*, 508:941, Dec 2009. doi: 10.1051/0004-6361/200912275.

N. Bello González, M. Franz, V. Martínez Pillet, J. A. Bonet, S. K. Solanki, J. C. del Toro Iniesta, W. Schmidt, A. Gandorfer, V. Domingo, P. Barthol, T. Berkefeld, and M. Knölker. Detection of large acoustic energy flux in the solar atmosphere. *ApJ*, 723(2):L134–L138, Nov 2010a. doi: 10.1088/2041-8205/723/2/L134.

N. Bello González, M. Franz, V. Martínez Pillet, J. A. Bonet, S. K. Solanki, J. C. del Toro Iniesta, W. Schmidt, A. Gandorfer, V. Domingo, P. Barthol, T. Berkefeld, and M. Knölker. Detection of large acoustic energy flux in the solar atmosphere. *ApJ*, 723(2):L134–L138, Nov 2010b. doi: 10.1088/2041-8205/723/2/L134.

T. E. Berger, B. De Pontieu, C. J. Schrijver, and A. M. Title. High-resolution imaging of the solar chromosphere/corona transition region. *ApJ*, 519(1):L97–L100, Jul 1999. doi: 10.1086/312088.

A. Berlicki, P. Heinzel, B. Schmieder, P. Mein, and N. Mein. Non-LTE diagnostics of velocity fields during the gradual phase of a solar flare. *A&A*, 430:679–689, Feb 2005. doi: 10.1051/0004-6361:20041293.

L. Biermann. Über die Ursache der chromosphärischen Turbulenz und des UV-Exzesses der Sonnenstrahlung. *ZAp*, 25:161, Jan 1948.

J. M. Borrero, S. Tomczyk, M. Kubo, H. Socas-Navarro, J. Schou, S. Couvidat, and R. Bogart. VFISV: Very Fast Inversion of the Stokes Vector for the Helioseismic and Magnetic Imager. *Sol. Phys.*, 273(1):267–293, Oct 2011. doi: 10.1007/s11207-010-9515-6.

E. Bratsolis, D. Dialetis, and C.E. Alissandrakis. A new determination of the mean lifetime of bright and dark chromospheric mottles. *A&A*, 274:940, 1993.

P. S. Cally. Dispersion relations, rays and ray splitting in magnetohelioseismology. *Phil. Trans. Roy. Soc. London Ser. A*, 364(1839):333–349, Feb 2006. doi: 10.1098/rsta.2005.1702.

W. Cao, N. Gorceix, R. Coulter, K. Ahn, T. R. Rimmele, and P. R. Goode. Scientific instrumentation for the 1.6 m New Solar Telescope in Big Bear. *Astron. Nachr.*, 331(6):636, Jun 2010. doi: 10.1002/asna.201011390.

M. Carlsson and J. Leenaarts. Approximations for radiative cooling and heating in the solar chromosphere. *A&A*, 539:A39, Mar 2012a. doi: 10.1051/0004-6361/201118366.

M. Carlsson and J. Leenaarts. Approximations for radiative cooling and heating in the solar chromosphere. *A&A*, 539:A39, Mar 2012b. doi: 10.1051/0004-6361/201118366.

M. Carlsson and R. F. Stein. Non-LTE radiating acoustic shocks and Ca II K2V bright points. *ApJ*, 397:L59, Sep 1992. doi: 10.1086/186544.

M. Carlsson and R. F. Stein. Does a nonmagnetic solar chromosphere exist? *ApJ*, 440:L29, Feb 1995. doi: 10.1086/187753.

M. Carlsson and R. F. Stein. Formation of solar calcium H and K bright grains. *ApJ*, 481(1):500–514, May 1997. doi: 10.1086/304043.

M. Carlsson and R. F. Stein. The dynamic solar chromosphere and the ionization of hydrogen. In S. R. Habbal, R. Esser, J. V. Hollweg, and P. A. Isenberg, editors, *American Institute of Physics Conference Series*, volume 471, pages 23–28, Jun 1999. doi: 10.1063/1.58753.

M. Carlsson, P. G. Judge, and K. Wilhelm. SUMER observations confirm the dynamic nature of the quiet solar outer atmosphere: The internetwork chromosphere. *ApJ*, 486(1):L63–L66, Sep 1997. doi: 10.1086/310836.

M. Carlsson, V. H. Hansteen, B. de Pontieu, S. McIntosh, T. D. Tarbell, D. Shine, S. Tsuneta, Y. Katsukawa, K. Ichimoto, Y. Suematsu, T. Shimizu, and S. Nagata. Can high frequency acoustic waves heat the quiet Sun chromosphere? *PASJ*, 59:S663, Nov 2007. doi: 10.1093/pasj/59.sp3.S663.

G. Cauzzi, K. P. Reardon, H. Uitenbroek, F. Cavallini, A. Falchi, R. Falciani, K. Janssen, T. Rimmele, A. Vecchio, and F. Wöger. The solar chromosphere at high resolution with IBIS. I. New insights from the Ca II 854.2 nm line. *A&A*, 480(2):515–526, Mar 2008. doi: 10.1051/0004-6361:20078642.

F. Cavallini. IBIS: A new post-focus instrument for solar imaging spectroscopy. *Sol. Phys.*, 236(2):415–439, Jul 2006. doi: 10.1007/s11207-006-0103-8.

R. Centeno, J. Schou, K. Hayashi, A. Norton, J. T. Hoeksema, Y. Liu, K. D. Leka, and G. Barnes. The Helioseismic and Magnetic Imager (HMI) vector magnetic field pipeline: optimization of the spectral line inversion Code. *Sol. Phys.*, 289 (9):3531–3547, Sep 2014. doi: 10.1007/s11207-014-0497-7.

J. Chae, H. Park, K. Ahn, H. Yang, Y. Park, J. Nah, B. Jang, K. Cho, W. Cao, and P. R. Goode. Fast Imaging Solar Spectrograph of the 1.6 Meter New Solar Telescope at Big Bear Solar Observatory. *Sol. Phys.*, 288(1):1–22, Nov 2013. doi: 10.1007/s11207-012-0147-x.

E. S. Chang, E. H. Avrett, P. J. Mauas, R. W. Noyes, and R. Loeser. Formation of the infrared emission lines of Mg I in the solar atmosphere. *ApJ*, 379:L79, Oct 1991. doi: 10.1086/186158.

M. Collados. High resolution spectropolarimetry and magnetography. In B. Schmieder, A. Hofmann, and J. Staude, editors, *Third Advances in Solar Physics Euroconference: Magnetic Fields and Oscillations*, volume 184 of *Astronomical Society of the Pacific Conference Series*, pages 3–22, 1999.

M. Collados, A. Lagg, J. J. Díaz Garcí A, E. Hernández Suárez, R. López López, E. Páez Mañá, and S. K. Solanki. Tenerife Infrared Polarimeter II. In P. Heinzel, I. Dorotovič, and R. J. Rutten, editors, *The Physics of Chromospheric Plasmas*, volume 368 of *Astronomical Society of the Pacific Conference Series*, page 611, May 2007.

M. Collados, R. López, E. Páez, E. Hernández, M. Reyes, A. Calcines, E. Ballesteros, J. J. Díaz, C. Denker, A. Lagg, R. Schlichenmaier, W. Schmidt, S. K. Solanki, K. G. Strassmeier, O. von der Lühe, and R. Volkmer. GRIS: The GREGOR Infrared Spectrograph. *Astronomische Nachrichten*, 333:872, Nov 2012. doi: 10.1002/asna.201211738.

R. D. Cowan. *The theory of atomic structure and spectra.* Berkeley: University of California Press, 1981.

L. E. Cram, S. L. Keil, and P. Ulmschneider. Some effects of acoustic waves on spectral-line profiles. *ApJ*, 234:768–774, Dec 1979. doi: 10.1086/157555.

M. Cuntz, W. Rammacher, and Z. E. Musielak. Acoustic heating of the solar chromosphere: present indeed and locally dominant. *ApJ*, 657:635, 2007. doi: 10.1086/512973.

B. De Pontieu, R. Erdelyi, A. de Wijn, and M. Loefdahl. Intensity oscillations in the upper transition region above active region plage. In *AGU Fall Meeting Abstracts*, volume 2003, pages SH42B–0540, Dec 2003.

B. De Pontieu, R. Erdélyi, and I. De Moortel. How to channel photospheric oscillations into the corona. *ApJ*, 624(1):L61–L64, May 2005. doi: 10.1086/430345.

B. de Pontieu, S. McIntosh, V. H. Hansteen, M. Carlsson, C. J. Schrijver, T. D. Tarbell, A. M. Title, R. A. Shine, Y. Suematsu, S. Tsuneta, Y. Katsukawa, K. Ichimoto, T. Shimizu, and S. Nagata. A tale of two spicules: the impact of spicules on the magnetic chromosphere. *PASJ*, 59:S655, Nov 2007. doi: 10.1093/pasj/59.sp3.S655.

B. De Pontieu, A. M. Title, J. R. Lemen, G. D. Kushner, D. J. Akin, B. Allard, T. Berger, P. Boerner, M. Cheung, C. Chou, J. F. Drake, D. W. Duncan, S. Freeland, G. F. Heyman, C. Hoffman, N. E. Hurlburt, R. W. Lindgren, D. Mathur, R. Rehse, D. Sabolish, R. Seguin, C. J. Schrijver, T. D. Tarbell, J. P. Wülser, C. J. Wolfson, C. Yanari, J. Mudge, N. Nguyen-Phuc, R. Timmons, R. van Bezooijen, I. Weingrod, R. Brookner, G. Butcher, B. Dougherty, J. Eder, V. Knagenhjelm, S. Larsen, D. Mansir, L. Phan, P. Boyle, P. N. Cheimets, E. E. DeLuca, L. Golub, R. Gates, E. Hertz, S. McKillop, S. Park, T. Perry, W. A. Podgorski, K. Reeves, S. Saar, P. Testa, H. Tian, M. Weber, C. Dunn, S. Eccles, S. A. Jaeggli, C. C. Kankelborg, K. Mashburn, N. Pust, L. Springer, R. Carvalho, L. Kleint, J. Marmie, E. Mazmanian, T. M. D. Pereira, S. Sawyer, J. Strong, S. P. Worden, M. Carlsson, V. H. Hansteen, J. Leenaarts, M. Wiesmann, J. Aloise, K. C. Chu, R. I. Bush, P. H. Scherrer, P. Brekke, J. Martinez-Sykora, B. W. Lites, S. W. McIntosh, H. Uitenbroek, T. J. Okamoto, M. A. Gummin, G. Auker, P. Jerram, P. Pool, and N. Waltham. The Interface Region Imaging Spectrograph (IRIS). *Sol. Phys.*, 289(7):2733–2779, Jul 2014. doi: 10.1007/s11207-014-0485-y.

E. Dineva, M. Verma, S. J. González Manrique, P. Schwartz, and C. Denker. Cloud model inversions of strong chromospheric absorption lines using principal component analysis. *Astronomische Nachrichten*, 341(1):64–78, Jan 2020. doi: 10.1002/asna.202013652.

D. Fawzy, P. Ulmschneider, K. Stępień, Z. E. Musielak, and W. Rammacher. Acoustic and magnetic wave heating in stars . II. On the range of chromospheric activity. *A&A*, 386:983–993, May 2002. doi: 10.1051/0004-6361:20020265.

D. E. Fawzy and Z. E. Musielak. Atmospheric oscillations in late-type stars - I. Non-linear response to excitation by acoustic wave energy spectra. *MNRAS*, 421(1):159–168, Mar 2012. doi: 10.1111/j.1365-2966.2011.20285.x.

J. Fontenla, O. R. White, P. A. Fox, E. H. Avrett, and R. L. Kurucz. Calculation of solar irradiances. I. Synthesis of the solar spectrum. *ApJ*, 518(1):480–499, Jun 1999. doi: 10.1086/307258.

J. M. Fontenla, E. H. Avrett, and R. Loeser. Energy balance in the solar transition region. III. Helium emission in hydrostatic, constant-abundance models with diffusion. *ApJ*, 406:319, Mar 1993. doi: 10.1086/172443.

J. M. Fontenla, E. H. Avrett, and R. Loeser. Energy balance in the solar transition region. IV. Hydrogen and helium mass flows with diffusion. *ApJ*, 572(1):636–662, Jun 2002. doi: 10.1086/340227.

J. M. Fontenla, E. Avrett, G. Thuillier, and J. Harder. Semi-empirical models of the solar atmosphere. I. The quiet- and active Sun photosphere at moderate resolution. *ApJ*, 639(1):441–458, Mar 2006. doi: 10.1086/499345.

A. Fossum and M. Carlsson. High-frequency acoustic waves are not sufficient to heat the solar chromosphere. *Nature*, 435(7044):919–921, Jun 2005. doi: 10.1038/nature03695.

S. L. Freeland and B. N. Handy. Data analysis with the SolarSoft system. *Sol. Phys.*, 182:497–500, 1998. doi: 10.1023/A:1005038224881.

A. H. Gabriel. A magnetic model of the solar transition region. *Philosophical Transactions of the Royal Society of London Series A*, 281(1304):339–352, May 1976. doi: 10.1098/rsta.1976.0031.

A. Garcia, M. Klvaňa, and M. Sobotka. Measurements of chromospheric velocity fields by means of the Coimbra University spectroheliograph. *Central European Astrophysical Bulletin*, 34:47–56, Jan 2010.

M. K. Georgoulis. A new technique for a routine azimuth disambiguation of solar vector magnetograms. *ApJ*, 629(1):L69–L72, Aug 2005. doi: 10.1086/444376.

A. Ghosh, J. A. Klimchuk, and D. Tripathi. On Doppler shift and its center-to-limb variation in active regions in the transition region. *ApJ*, 886(1):46, Nov 2019. doi: 10.3847/1538-4357/ab43c4.

O. Gingerich and C. de Jager. The Bilderberg model of the photosphere and low chromosphere. *Sol. Phys.*, 3(1):5–25, Jan 1968. doi: 10.1007/BF00154238.

R. G. Giovanelli and H. P. Jones. The three-dimensional structure of atmospheric magnetic fields in two active regions. *Sol. Phys.*, 79(2):267–278, Aug 1982. doi: 10.1007/BF00146244.

P. R. Goode, C. J. Denker, L. I. Didkovsky, J. R. Kuhn, and H. Wang. 1.6 M Solar Telescope in Big Bear – The NST. *Journal of Korean Astronomical Society*, 36:S125–S133, June 2003. doi: 10.5303/JKAS.2003.36.spc1.125.

P. Gouttebroze. Solar atmospheric dynamics. III. The effect of acoustic waves on the Mg II K line profile. *ApJ*, 337:536, Feb 1989. doi: 10.1086/167122.

B. V. Gudiksen, M. Carlsson, V. H. Hansteen, W. Hayek, J. Leenaarts, and J. Martínez-Sykora. The stellar atmosphere simulation code Bifrost. Code description and validation. *A&A*, 531:A154, Jul 2011. doi: 10.1051/0004-6361/201116520.

E. Gurtovenko, V. Ratnikova, and C. De Jager. On the average optical depth of formation of weak Fraunhofer lines. *Sol. Phys.*, 37:43, 1974. doi: 10.1007/BF00157842.

J. W. Harvey, F. Hill, R. P. Hubbard, J. R. Kennedy, J. W. Leibacher, J. A. Pintar, P. A. Gilman, R. W. Noyes, A. M. Title, J. Toomre, R. K. Ulrich, A. Bhatnagar, J. A. Kennewell, W. Marquette, J. Patron, O. Saa, and E. Yasukawa. The Global Oscillation Network Group (GONG) Project. *Science*, 272 (5266):1284–1286, May 1996. doi: 10.1126/science.272.5266.1284.

L. Heggland, V. H. Hansteen, B. De Pontieu, and M. Carlsson. Wave propagation and jet formation in the chromosphere. *ApJ*, 743(2):142, Dec 2011. doi: 10.1088/0004-637X/743/2/142.

P. Heinzel. Multilevel NLTE radiative transfer in isolated atmospheric structures: implementation of the MALI-technique. *A&A*, 299:563, July 1995.

P. Heinzel. in *The Sun as a Guide to Stellar Physics, Chapter 5.2 - Models of Solar and Stellar Atmospheres*, pages 157–183. Amsterdam: Elsevier, 2019. doi: 10.1016/B978-0-12-814334-6.00006-6.

P. Heinzel and B. Schmieder. Chromospheric fine structure: black & white mottles. *A&A*, 282:939–954, 1994.

J. T. Hoeksema, Y. Liu, K. Hayashi, X. Sun, J. Schou, S. Couvidat, A. Norton, M. Bobra, R. Centeno, K. D. Leka, G. Barnes, and M. Turmon. The Helioseismic and Magnetic Imager (HMI) vector magnetic field pipeline: overview and performance. *Sol. Phys.*, 289(9):3483–3530, Sep 2014. doi: 10.1007/s11207-014-0516-8.

A. Hofmann, K. Arlt, H. Balthasar, S. M. Bauer, W. Bittner, J. Paschke, E. Popow, J. Rendtel, D. Soltau, and T. Waldmann. The GREGOR polarimetric calibration unit. *Astronomische Nachrichten*, 333(9):854, Nov 2012. doi: 10.1002/asna.201211733.

H. Holweger. The solar abundance of calcium and collision broadening of Ca i- and Ca ii-Fraunhofer lines by hydrogen. *Sol. Phys.*, 25(1):14–29, July 1972. doi: 10.1007/BF00155741.

S. M. Jefferies, S. W. McIntosh, J. D. Armstrong, T. J. Bogdan, A. Cacciani, and B. Fleck. Low-frequency magneto-acoustic waves in the solar chromosphere. In *Proceedings of SOHO 18/GONG 2006/HELAS I, Beyond the spherical Sun*, volume 624 of *ESA Special Publication*, page 16, Oct 2006.

D. B. Jess, R. J. Morton, G. Verth, V. Fedun, S. D. T. Grant, and I. Giagkiozis. Multiwavelength studies of MHD waves in the solar chromosphere. An overview of recent results. *Space Sci. Rev.*, 190(1-4):103–161, Jul 2015. doi: 10.1007/s11214-015-0141-3.

H. P. Jones and R. G. Giovanelli. Magnetograph response to canopy-type fields. *Sol. Phys.*, 79(2):247–266, Aug 1982. doi: 10.1007/BF00146243.

U. G. Jorgensen, M. Carlsson, and H. R. Johnson. The calcium infrared triplet lines in stellar spectra. *A&A*, 254:258–265, Feb 1992.

P. G. Judge, L. Kleint, J. Leenaarts, A. V. Sukhorukov, and J. Vial. New light on an old problem of the cores of solar resonance lines. *ApJ*, 901(1):32, Sep 2020. doi: 10.3847/1538-4357/abadf4.

W. Kalkofen. The Solar chromosphere: observations and models. In *AGU Spring Meeting Abstracts*, volume 2001, pages SH21B–01 INVITED, May 2001.

W. Kalkofen, P. Ulmschneider, and E. H. Avrett. Does the Sun have a full-time chromosphere? *ApJ*, 521(2):L141–L144, Aug 1999. doi: 10.1086/312193.

P. Kayshap, K. Murawski, A. K. Srivastava, Z. E. Musielak, and B. N. Dwivedi. Vertical propagation of acoustic waves in the solar internetworkas observed by IRIS. *MNRAS*, 479(4):5512–5521, Oct 2018. doi: 10.1093/mnras/sty1861.

I. Kontogiannis, G. Tsiropoula, and K. Tziotziou. Power halo and magnetic shadow in a solar quiet region observed in the Hα line. *A&A*, 510:A41, Feb 2010. doi: 10.1051/0004-6361/200912841.

I. Kontogiannis, G. Tsiropoula, and K. Tziotziou. Transmission and conversion of magnetoacoustic waves on the magnetic canopy in a quiet Sun region. *A&A*, 567:A62, Jul 2014. doi: 10.1051/0004-6361/201423986.

I. Kontogiannis, G. Tsiropoula, and K. Tziotziou. Wave propagation in a solar quiet region and the influence of the magnetic canopy. *A&A*, 585:A110, Jan 2016. doi: 10.1051/0004-6361/201527053.

R. L. Kurucz. A new theoretical model photosphere. In *Bulletin of the American Astronomical Society*, volume 23, page 1047, Mar 1991.

R. L. Kurucz. LTE models. *Highlights of Astronomy*, 11A:646, Jan 1998.

H. Lamb. *Hydrodynamics*. New York: Dover, 1932.

E. Landi degl'Innocenti. Evidence against turbulent and canopy-like magnetic fields in the solar chromosphere. *Nature*, 392(6673):256–258, Mar 1998. doi: 10.1038/32603.

J. Lee, S. M. White, M. R. Kundu, Z. Mikić , and A. N. McClymont. A test for coronal magnetic field extrapolations. *ApJ*, 510(1):413–421, Jan 1999. doi: 10.1086/306556.

J. Leenaarts. Radiation hydrodynamics in simulations of the solar atmosphere. *Living Reviews in Solar Physics*, 17(1):3, Mar 2020. doi: 10.1007/s41116-020-0024-x.

J. Leenaarts, T. M. D. Pereira, M. Carlsson, H. Uitenbroek, and B. De Pontieu. The formation of IRIS diagnostics. I. A quintessential model atom of Mg II and general formation properties of the Mg II h&k lines. *ApJ*, 772(2):89, Aug 2013. doi: 10.1088/0004-637X/772/2/89.

K. D. Leka, G. Barnes, and A. Crouch. An automated ambiguity-resolution code for Hinode/SP vector magnetic field data. In B. Lites, M. Cheung, T. Magara, J. Mariska, and K. Reeves, editors, *The Second Hinode Science Meeting: Beyond Discovery-Toward Understanding*, volume 415 of *Astronomical Society of the Pacific Conference Series*, page 365, Dec 2009.

J. L. Linsky. On the relative residual intensities of the calcium H and K lines. *Sol. Phys.*, 11(3):355–373, Mar 1970. doi: 10.1007/BF00153071.

J. L. Linsky and E. H. Avrett. The solar H and K lines. *PASP*, 82(485):169, Apr 1970. doi: 10.1086/128904.

B. W. Lites and E. G. Chipman. The vertical propagation of waves in the solar atmosphere. I. Observations of phase delay. *ApJ*, 231:570–588, Jul 1979. doi: 10.1086/157219.

B. W. Lites, E. G. Chipman, and O. R. White. The vertical propagation of waves in the solar atmosphere. II Phase delays in the quiet chromosphere and cell-network distinctions. *ApJ*, 253:367–385, Feb 1982. doi: 10.1086/159641.

B. W. Lites, D. F. Elmore, P. Seagraves, and A. P. Skumanich. Stokes profile analysis and vector magnetic fields. VI. Fine scale structure of a sunspot. *ApJ*, 418:928, Dec 1993. doi: 10.1086/173450.

B. W. Lites, B. C. Low, V. Martínez Pillet, P. Seagraves, A. Skumanich, Z. A. Frank, R. A. Shine, and S. Tsuneta. The possible ascent of a closed magnetic system through the photosphere. *ApJ*, 446:877, Jun 1995. doi: 10.1086/175845.

P. Maltby, E. H. Avrett, M. Carlsson, O. Kjeldseth-Moe, R. L. Kurucz, and R. Loeser. A new sunspot umbral model and its variation with the solar cycle. *ApJ*, 306:284, Jul 1986. doi: 10.1086/164342.

L. Mashonkina, T. Gehren, J. R. Shi, A. J. Korn, and F. Grupp. A non-LTE study of neutral and singly-ionized iron line spectra in 1D models of the Sun and selected late-type stars. *A&A*, 528:A87, Apr 2011. doi: 10.1051/0004-6361/201015336.

N. Mein and P. Mein. Mechanical flux in the solar chromosphere. I - Velocity and temperature weighting functions for CA II lines. *A&A*, 84(1-2):96–98, Apr 1980.

H. Mészárosová and P. Gömöry. Magnetically coupled atmosphere, fast sausage MHD waves, and forced magnetic field reconnection during the SOL2014-09-10T17:45 flare. *A&A*, 643:A140, Nov 2020. doi: 10.1051/0004-6361/202038388.

D. Mihalas. *Stellar atmospheres*. San Francisco: W.H. Freeman, 1978.

J. S. Morrill, K. P. Dere, C. M. Korendyke, and L. E. Floyd. Solar irradiance variability modeled near Mg II using plage and sunspot contrast factors measured by HRTS. In *AGU Fall Meeting Abstracts*, volume 2001, pages SH11C–0733, Dec 2001.

R. J. Morton, G. Verth, A. Hillier, and R. Erdélyi. The generation and damping of propagating MHD kink waves in the solar atmosphere. *ApJ*, 784(1):29, Mar 2014. doi: 10.1088/0004-637X/784/1/29.

J. M. Pasachoff, W. A. Jacobson, and A. C. Sterling. Limb spicules from the ground and from space. *Sol. Phys.*, 260(1):59–82, 2009.

W. D. Pesnell, B. J. Thompson, and P. C. Chamberlin. The Solar Dynamics Observatory (SDO). *Sol. Phys.*, 275(1-2):3–15, Jan 2012. doi: 10.1007/s11207-011-9841-3.

A. Pietarila, J. Hirzberger, V. Zakharov, and S.K. Solanki. Bright fibrils in ca ii k. *A&A*, 502(2):647–660, 2009.

W. H. Press, S. A. Teukolsky, W. T. Vetterling, and B. P. Flannery. *Numerical recipes in FORTRAN. The art of scientific computing*. Cambridge: University Press, 2nd ed., 1992.

D. Rabin and R. Moore. Heating the sun's lower transition region with fine-scale electric currents. *ApJ*, 285:359, Apr 1984. doi: 10.1086/162513.

S. P. Rajaguru, C. R. Sangeetha, and D. Tripathi. Magnetic fields and the supply of low-frequency acoustic wave energy to the solar chromosphere. *ApJ*, 871(2):155, Feb 2019. doi: 10.3847/1538-4357/aaf883.

K. P. Reardon, F. Lepreti, V. Carbone, and A. Vecchio. Evidence of shock-driven turbulence in the solar chromosphere. *ApJ*, 683(2):L207, Aug 2008. doi: 10.1086/591790.

R. Rezaei, J. Bruls, C. Beck, W. Schmidt, W. Kalkofen, and R. Schlichenmaier. Reversal-free Ca II H profiles: a challenge for solar chromosphere modeling in quiet inter-Network. In *12th European Solar Physics Meeting, Freiburg, Germany*, page 2.13, Sep 2008.

T. R. Rimmele, K. Richards, S. Hegwer, S. Fletcher, S. Gregory, G. Moretto, L. V. Didkovsky, C. Denker, A. Dolgushin, P. R. Goode, M. Langlois, J. Marino, and W. Marquette. First results from the NSO/NJIT solar adaptive optics system. In Silvano Fineschi and Mark A. Gummin, editors, *Telescopes and Instrumentation for Solar Astrophysics*, volume 5171 of *Society of Photo-Optical Instrumentation Engineers (SPIE) Conference Series*, pages 179–186, Feb 2004. doi: 10.1117/12.508513.

W. O. Roberts. A preliminary report on chromospheric spicules of extremely short lifetime. *ApJ*, 101:136, Mar 1945. doi: 10.1086/144699.

S. Routh and Z. E. Musielak. Propagation of acoustic waves in the non-isothermal solar atmosphere. *Astronomische Nachrichten*, 335(10):1043, Dec 2014. doi: 10.1002/asna.201412128.

S. Routh, Z. Musielak, and R. Hammer. Cut off free propagation of torsional waves along solar magnetic flux tubes. In *APS Texas Sections Fall Meeting Abstracts*, APS Meeting Abstracts, page AP1.006, Oct 2006.

B. Ruiz Cobo and J. C. del Toro Iniesta. Inversion of Stokes profiles. *ApJ*, 398: 375, Oct 1992. doi: 10.1086/171862.

R. J. Rutten et al. *Radiative transfer in stellar atmospheres*. Sterrekundig Instituut Utrecht, 1995.

G. B. Rybicki. A modified Feautrier method. *J. Quant. Spectr. Rad. Transf.*, 11: 589–595, Jan 1971. doi: 10.1016/0022-4073(71)90040-9.

G. B. Rybicki and D. G. Hummer. An accelerated lambda iteration method for multilevel radiative transfer. *A&A*, 245:171, 1991.

G. B. Rybicki and D. G. Hummer. An accelerated lambda iteration method for multilevel radiative transfer. II. Overlapping transitions with full continuum. *A&A*, 262:209, 1992.

W. Schmidt, O. von der Lühe, R. Volkmer, C. Denker, S. K. Solanki, H. Balthasar, N. Bello Gonzalez, Th. Berkefeld, M. Collados, A. Fischer, C. Halbgewachs, F. Heidecke, A. Hofmann, F. Kneer, A. Lagg, H. Nicklas, E. Popow, K. G. Puschmann, D. Schmidt, M. Sigwarth, M. Sobotka, D. Soltau, J. Staude, K. G. Strassmeier, and T. A. Waldmann . The 1.5 meter solar telescope GREGOR. *Astronomische Nachrichten*, 333(9):796, Nov 2012. doi: 10.1002/asna.201211725.

J. Schou, P. H. Scherrer, R. I. Bush, R. Wachter, S. Couvidat, M. C. Rabello-Soares, R. S. Bogart, J. T. Hoeksema, Y. Liu, T. L. Duvall, D. J. Akin, B. A. Allard, J. W. Miles, R. Rairden, R. A. Shine, T. D. Tarbell, A. M. Title, C. J. Wolfson, D. F. Elmore, A. A. Norton, and S. Tomczyk. Design and Ground Calibration of the Helioseismic and Magnetic Imager (HMI) Instrument on the Solar Dynamics Observatory (SDO). *Sol. Phys.*, 275(1-2):229–259, Jan 2012. doi: 10.1007/s11207-011-9842-2.

C. J. Schrijver and A. M. Title. The magnetic connection between the solar photosphere and the corona. *ApJ*, 597(2):L165–L168, Nov 2003. doi: 10.1086/379870.

E. H. Schröter, D. Soltau, and E. Wiehr. The German solar telescopes at the Observatorio del Teide. *New Astronomy Reviews*, 28:519, Oct 1985. doi: 10.1016/0083-6656(85)90073-X.

M. Schwarzschild. On Noise Arising from the Solar Granulation. *ApJ*, 107:1, Jan 1948. doi: 10.1086/144983.

S. Shumko, N. Gorceix, S. Choi, A. Kellerer, W. Cao, P. R. Goode, V. Abramenko, K. Richards, T. R. Rimmele, and J. Marino. *AO-308: the high-order adaptive optics system at Big Bear Solar Observatory*, volume 9148 of *Proc. SPIE*, page 914835. 2014. doi: 10.1117/12.2056731.

M. Sobotka, M. Švanda, J. Jurčák, P. Heinzel, D. Del Moro, and F. Berrilli. Dynamics of the solar atmosphere above a pore with a light bridge. *A&A*, 560: A84, Dec 2013. doi: 10.1051/0004-6361/201322148.

M. Sobotka, P. Heinzel, M. Švanda, J. Jurčák, D. del Moro, and F. Berrilli. Chromospheric heating by acoustic waves compared to radiative cooling. *ApJ*, 826:49, 2016. doi: 10.3847/0004-637X/826/1/49.

S. K. Solanki. Small scale solar magnetic fields - an overview. *Space Sci. Rev.*, 63(1-2):1–188, Mar 1993. doi: 10.1007/BF00749277.

S. K. Solanki. in *European Meeting on Solar Physics, Dynamics of Flux Tubes in the Solar Atmosphere: Observations,* Eds. G.M. Simnett, C.E. Alissandrakis, and L. Vlahos. Springer-Verlag Berlin Heidelberg New York, 1997. doi: 10.1007/BFb0105670.

S. K. Solanki and O. Steiner. How magnetic is the solar chromosphere? *A&A*, 234(1-2):519–529, Aug 1990.

M. Stangalini, D. Del Moro, F. Berrilli, and S. M Jefferies. MHD wave transmission in the Sun's atmosphere. *A&A*, 534(2):82, Oct 2011. doi: 10.1051/0004-6361/201117356.

O. Steiner. Theoretical Models of Magnetic Flux Tubes: Structure and Dynamics. In D. M. Rabin, John T. Jefferies, and C. Lindsey, editors, *Infrared Solar Physics,* IAU Symp., volume 154, page 407, January 1994.

A. C. Sterling and J. V. Hollweg. A rebound shock mechanism for solar fibrils. *ApJ*, 343:985, Aug 1989. doi: 10.1086/167767.

T. Straus, B. Fleck, S. M. Jefferies, G. Cauzzi, S. W. McIntosh, K. Reardon, G. Severino, and M. Steffen. The energy flux of internal gravity waves in the lower solar atmosphere. *ApJ*, 681(2):L125, Jul 2008. doi: 10.1086/590495.

R. N. Thomas. The source function in a non-equilibrium atmosphere.IV. Evaluation and applications of the net radiative bracket. *ApJ*, 131:429, Mar 1960. doi: 10.1086/146847.

A. P. Thorne, U. Litzen, and S. Johansson. *Spectrophysics.* Principles and Applications XIV, Springer-Verlag Berlin Heidelberg New York, 1999.

C. Torrence and G. P. Compo. A practical guide to wavelet analysis. *Bulletin of the American Meteorological Society*, 79(1):61–78, Jan 1998. doi: 10.1175/1520-0477(1998)079<0061:APGTWA>2.0.CO;2.

G. Tsiropoula, K. Tziotziou, I. Kontogiannis, M.S. Madjarska, J.G. Doyle, and Y. Suematsu. Solar fine-scale structures. i. spicules and other small-scale, jet-like events at the chromospheric level: observations and physical parameters. *Space science reviews*, 169(1-4):181–244, 2012.

H. Uitenbroek and C. Briand. The Mg I lambda 285.21 nm Line: an example of non-LTE line formation. *ApJ*, 447:453, Jul 1995. doi: 10.1086/175889.

P. Ulmschneider and Z. Musielak. Mechanisms of Chromospheric and Coronal Heating (Invited review). In A. A. Pevtsov and H. Uitenbroek, editors, *Current Theoretical Models and Future High Resolution Solar Observations: Preparing for ATST*, volume 286 of *Astronomical Society of the Pacific Conference Series*, page 363, January 2003.

P. Ulmschneider, W. Rammacher, Z. E. Musielak, and W. Kalkofen. On the validity of acoustically heated chromosphere models. *ApJ*, 631(2):L155–L158, Oct 2005. doi: 10.1086/497395.

R. Ulmschneider, F. Schmitz, W. Kalkofen, and H. U. Bohn. Acoustic waves in the solar atmosphere. V. On the chromospheric temperature rise. *A&A*, 70: 487, Nov 1978.

T. A. Underwood, D. Voelz, F. Schmider, J. Jackiewicz, J. Dejonghe, Y. Bresson, R. Hull, I. Goncalves, P. Gualme, F. Morand, and O. Preis. Adaptation of Dunn Solar Telescope for Jovian Doppler spectro imaging. In *Society of Photo-Optical Instrumentation Engineers (SPIE) Conference Series*, volume 10401, page 104010Y, Sep 2017. doi: 10.1117/12.2275909.

M. van Noort, L. Rouppe van der Voort, and M. Löfdahl. Solar image restoration by use of multi-object multi-frame blind deconvolution. In J. Leibacher, R. F. Stein, and H. Uitenbroek, editors, *Solar MHD Theory and Observations: A High Spatial Resolution Perspective*, volume 354 of *Astronomical Society of the Pacific Conference Series*, page 55, Dec 2006.

A. Vecchio, G. Cauzzi, K. P. Reardon, K. Janssen, and T. Rimmele. Solar atmospheric oscillations and the chromospheric magnetic topology. *A&A*, 461:L1, 2007. doi: 10.1051/0004-6361:20066415.

J. E. Vernazza, E. H. Avrett, and R. Loeser. Structure of the solar chromosphere. II. The underlying photosphere and temperature-minimum region. *ApJS*, 30: 1–60, Jan 1976. doi: 10.1086/190356.

J. E. Vernazza, E. H. Avrett, and R Loeser. Structure of the solar chromosphere. III - Models of the EUV brightness components of the quiet-sun. *ApJS*, 45: 635, 1981. doi: 10.1086/190731.

B. Viticchié, D. Del Moro, S. Criscuoli, and F. Berrilli. Imaging spectropolarimetry with IBIS. II. On the fine structure of G-band bright features. *ApJ*, 723 (1):787–796, Nov 2010. doi: 10.1088/0004-637X/723/1/787.

O von der Lühe. High-resolution observations with the German Vacuum TowerTelescope on Tenerife. *New Astronomy Reviews*, 42:493, Oct 1998. doi: 10.1016/S1387-6473(98)00060-8.

T. Watanabe and W. Steenbock. Statistical equilibrium of neutral calcium in the sun and Procyon. *A&A*, 149:21–28, Aug 1985.

S. Wedemeyer-Böhm, O. Steiner, J. Bruls, and W. Rammacher. What is heating the quiet-Sun chromosphere? In P. Heinzel, I. Dorotovič, and R. J. Rutten, editors, *The Physics of Chromospheric Plasmas*, volume 368 of *Astronomical Society of the Pacific Conference Series*, page 93, May 2007.

S. Wedemeyer-Böhm, A. Lagg, and Å. Nordlund. Coupling from the photosphere to the chromosphere and the corona. *Space Sci. Rev.*, 144(1-4):317–350, Apr 2009. doi: 10.1007/s11214-008-9447-8.

A. Wiśniewska, Z. E. Musielak, J. Staiger, and M. Roth. Observational evidence for variations of the acoustic cutoff frequency with height in the solar atmosphere. *ApJ*, 819(2):L23, Mar 2016. doi: 10.3847/2041-8205/819/2/L23.

J. P. Wülser, S. Jaeggli, B. De Pontieu, T. Tarbell, P. Boerner, S. Freeland, W. Liu, R. Timmons, S. Brannon, C. Kankelborg, C. Madsen, S. McKillop, J. Prchlik, S. Saar, N. Schanche, P. Testa, P. Bryans, and M. Wiesmann. Instrument calibration of the Interface Region Imaging Spectrograph (IRIS) mission. *Sol. Phys.*, 293(11):149, Nov 2018. doi: 10.1007/s11207-018-1364-8.

M. Wunnenberg, F. Kneer, and J. Hirzberger. Evidence for short-period acoustic waves in the solar atmosphere. *A&A*, 395:L51–L54, Nov 2002. doi: 10.1051/0004-6361:20021531.

T. V. Zaqarashvili and R. Erdélyi. Oscillations and waves in solar spicules. *Space Sci. Rev.*, 149(1-4):355–388, Dec 2009. doi: 10.1007/s11214-009-9549-y.

List of Figures

List of Tables